APPLICATIONS OF THERMOPHYSICAL CHARACTERIZATION USING THE 3-OMEGA TECHNIQUE

A Dissertation
Presented to
The Academic Faculty

by

Sampath Kommandur

In Partial Fulfillment
of the Requirements for the Degree
of Doctor of Philosophy in the
George W. Woodruff School of Mechanical Engineering

Georgia Institute of Technology
May 2019

APPLICATIONS OF THERMOPHYSICAL CHARACTERIZATION USING THE 3-OMEGA TECHNIQUE

Approved by:

Dr. Shannon K. Yee, Advisor
School of Mechanical Engineering
Georgia Institute of Technology

Dr. Peter Hesketh
School of Mechanical Engineering
Georgia Institute of Technology

Dr. Andrei Fedorov
School of Mechanical Engineering
Georgia Institute of Technology

Dr. Zhuomin Zhang
School of Mechanical Engineering
Georgia Institute of Technology

Dr. Michael Filler
School of Chemical and Biomolecular Engineering
Georgia Institute of Technology

Date Approved: [March 08, 2019]

To my parents, Badri Narayanan and Geetha

ACKNOWLEDGEMENTS

I am grateful to my advisor, Prof. Shannon Yee for accepting me as one of his first graduate students and helping me succeed as a Ph.D. candidate. I am especially thankful for his trust in me by letting me work on multiple projects over the course of 5 years and assist him in writing a project proposal. Recognizing my passion for teaching, he encouraged me to serve as the instructor of record for two full semesters, which has been one of my best experiences at Georgia Tech.

Next, I'd like to thank my committee members who have given me useful feedback, not only on my thesis but also about other aspects of academia. I'd like to express my gratitude to Dr. Andrei Fedorov and Dr. Zhuomin Zhang for accepting me as a teaching intern/teaching assistant and providing me valuable information about various aspects of teaching, and to Dr. Michael Filler and Dr. Peter Hesketh for helping me understand the nuances of research areas outside of my specialization.

I would like to acknowledge my colleagues at Georgia Tech – Dr. Brian Foley, Dr. Alireza Mahdavifar, Dr. Gozde Tutuncuoglu, Patrick Creamer, Abhinav Malhotra, and Aravindh Rajan – who helped me to accomplish different aspects of my thesis projects. I'd also like to mention the efforts of Shikai Jin and Abbas Furniturewalla, two undergraduates who worked with me during the early parts of my Ph.D. I'd also like to express gratitude to all my labmates from Yeelab, who have helped me in different ways over the past five years.

TABLE OF CONTENTS

LIST OF TABLES

LIST OF FIGURES

LIST OF SYMBOLS AND ABBREVIATIONS

b	Half-width of the heater line
d	Thickness of the sample
c	Specific (gravimetric) heat capacity
C	Volumetric heat capacity
D	Diffusivity of vibrational mode
$\overline{D}$	Dimensionless parameter to characterize modulated nanowire geometry
E	Elastic modulus
dR/dT	Temperature rate of change of resistance
f	Frequency
I_0	Amplitude of electrical current
j	Imaginary unit, given by $\sqrt{-1}$
k	Thermal conductivity
k_B	Boltzmann constant
L	Length of the heater line
$\overline{L}$	Dimensionless parameter to characterize modulated nanowire geometry
L_p	Thermal penetration depth
M	Monomer molecular weight
n	Number density
N	Energy density of states
P_0	Amplitude of heating power
R_c	Thermal contact resistance
R_0	Electrical resistance of the heater line

S_m	Cross-sectional area of microbridge
S_β	Sensitivity of a 3-omega measurement to the parameter β
T	Temperature
T_{Deb}	Debye temperature
$T_{m,n}$	Temperature rise of m^{th} microbridge when n^{th} microbridge is heated
ΔT	Temperature rise of the 3-omega heater line
v_{s}	Speed of sound
$V_{3\omega}$	3-omega voltage component
X	In-phase component of the 3-omega voltage
Y	Out-of-phase component of the 3-omega voltage
Z	Thermal transfer function/thermal impedance
zT	Thermoelectric figure-of-merit
α	Thermal diffusivity
δ	Kronecker delta function
η	Metric used to validate 1D anisotropic model
ρ	Density
υ	Poisson ratio
ω	Angular frequency
ϕ	Phase lag of the 3-omega voltage
$\hbar$	Reduced Planck's constant
$\parallel$	In-plane direction
$\perp$	Through-plane direction
BOE	Buffered Oxide Etch
FDTR	Frequency-Domain ThermoReflectance
ICP	Inductively Coupled Plasma

LPCVD	Low-Pressure Chemical Vapor Deposition
MD	Molecular Dynamics
RIE	Reactive Ion Etching
RMS	Root-Mean Square average
SEM	Scanning Electron Microscope
TCD	Thermal Conductivity Detector
TDTR	Time-Domain ThermoReflectance

SUMMARY

The 3-omega technique is a commonly used electrothermal technique to characterize thermal conductivity. While most commonly used to characterize isotropic thin films on substrates, the high accuracy and versatility of the technique can be extended to a broader application space. This dissertation focuses on exploring a few selected applications of thermophysical characterization. 3-omega excels in measuring low thermal conductivities (<1 W/m-K) with high accuracy, making it a prime choice for characterizing gases and amorphous polymers. Using experiments on gas mixtures, a gas sensing technique is developed that can determine gas concentrations in binary mixtures based on their thermophysical properties. This is demonstrated using two sensor geometries with sensitivities comparable to other electrothermal techniques, but with a lower power consumption. Using temperature dependent thermal conductivity of polymers, an empirical model is proposed to aid in predicting temperature-dependent thermal conductivity of amorphous polymers. The model is based on kinetic theory and accounts for the different vibrational modes (e.g., propagon, diffusons, and locons) in polymers, and depends on only the density, monomer molecular weight, and speed of sound. This empirical model's predictions are then validated using the 3-omega technique across a range of temperatures.

The second half of the dissertation focuses on variants of 3-omega technique to characterize anisotropic thermal conductivity in polymer films and nanostructures. A suspended film configuration to measure anisotropic thermal conductivity of polymers is presented. The experimental guidelines for validity of a simplified 1-D heat transfer model for data analysis are explicitly determined. This method is then used to determine the

anisotropic thermal conductivity of common semiconducting polymers and a few recently developed n-type organic thermoelectric materials. Finally, a suspended microbridge configuration to measure temperature-dependent thermal conductivity in nanowires is explored using a modification of 3ω technique. Data analysis using the modified technique is performed using an equivalent thermal impedance circuit and is validated using a steady-state technique reported in literature. The nanowires measured here as axially modulated with repeated doped and undoped segments with the doped segments etched to varying degrees. The effect of the geometry modulation on thermal conductivity is determined using experimental efforts.

CHAPTER 1. THE 3-OMEGA TECHNIQUE

Thin films, polymers, nanostructures, and related materials are of broad technological interest in applications such as thermoelectrics, optoelectronics, photovoltaics, and micro-electromechanical systems. Thermal performance is often a key consideration in many of these applications, making experimental efforts to measure thermal conductivity critical. There are a host of techniques currently available that can be used to measure thermophysical properties, especially thermal conductivity (k) and volumetric heat capacity (C). These techniques generally involve heating the sample and measuring the temperature response, which is subsequently analyzed using heat transfer models to obtain relevant thermophysical properties. Table 1 lists a few commonly used techniques, characterized according to the nature of heating and/or sensing. Some of the techniques such as transient hotwire, transient plane source, guarded hot plate, laser flash, are commercially available and adhere to ASTM standards. The various techniques listed in Table 1 have specific advantages depending on the size and phase of sample, surface characteristics, and the magnitude of thermophysical properties. Transient techniques (time-domain and frequency-domain) generally allow for better control over the measured sample volume and are favorable for measurement of thin films. Transient techniques also allow for faster measurements due to the lower wait times, and they often have higher measurement accuracy.

The dissertation focuses on applications of the 3-omega technique, which is a frequency-domain electrothermal technique. In electrothermal measurements, the sample is Joule heated by sourcing a current through a resistive element and the temperature

response of the sample is measured using resistive thermometry. The same resistive element can be used simultaneously as the heater and thermometer, or different elements can be used for heating and sensing purposes. The resistive element is often a metal layer deposited on the sample or a pre-fabricated heating element that is brought into contact with the sample. In case of electrically conducting samples, the sample itself can be used as the resistive heating and sensing element.

Table 1 – List of commonly used thermal metrology techniques

Steady-state techniques	Transient techniques (time-domain)	Transient techniques (frequency-domain)
1D reference bar (ASTM D5470)[1]	Transient hot-wire(ASTM D7896-14)[6]	3-omega[10]
Radial heat flow method[2,3]	Time-domain thermoreflectance[7]	Frequency-domain thermoreflectance[11]
Guarded hot plate (ASTM D1518)[4]	Laser flash method[8]	Pulsed power technique[12]
DC thermal bridge method[5]	Transient plane source (ASTM D7984-16)[9]	

1.1 Overview of the 3-omega technique

The 3-omega (3ω) technique is a frequency-domain electrothermal measurement technique, which has high accuracy and precision, with uncertainties typically under 10%.[10,13-15] In a standard 3ω measurement, a sinusoidal electrical current of amplitude I_0 at frequency $\omega = 2\pi f$ is sourced through a metal heater line of resistance R_0 deposited atop the sample of interest, resulting in a Joule heating of amplitude $P_0 = I_0^2 R_0/2$ at frequency 2ω, in addition to steady-state Joule heating of the same magnitude (see equation (2)).

$$I = I_0 \sin(\omega t) \tag{1}$$

$$P = I^2 R_0 = \frac{I_0^2 R_0}{2} - \frac{I_0^2 R_0}{2}\cos(2\omega t) \tag{2}$$

The periodic heating creates a thermal wave that penetrates the sample. The thermal wave attenuates over a penetration depth, given by $L_p = \sqrt{\alpha/2\omega}$, where $\alpha = k/C$ is the thermal diffusivity of the sample medium. This gives rise to a temperature oscillation of the heater at a frequency 2ω that lags the heating current by a phase lag ϕ due to the finite time it takes for a temperature response. The periodic temperature response is observed in addition to a DC temperature rise, caused by the steady-state Joule heating.

$$\Delta T = \Delta T_{DC} + \Delta T_{2\omega}\cos(2\omega t + \phi) \tag{3}$$

This temperature oscillation causes the resistance of the heater to oscillate at 2ω, as shown in equation (4). Here, dR/dT is the temperature rate of change of the heater resistance, which is equal to the product of temperature coefficient of resistance and the

resistance, R_0. The combination of the current sourced at 1ω and the resistance oscillation at 2ω results in a voltage component at 3ω. This is shown in equation (5)[16] and illustrated in Figure 1.

$$R = R_0 + \left(\frac{dR}{dT}\right)\Delta T \approx R_0 + \left(\frac{dR}{dT}\right)\Delta T_{2\omega}\cos\left(2\omega t + \phi\right) \tag{4}$$

$$\begin{aligned} V &= I\left(t\right)R\left(t\right) \\ &\approx I_0 R_0 \sin\left(\omega t\right) + I_0\left(\frac{dR}{dT}\right)\Delta T_{2\omega}\cos\left(2\omega t + \phi\right)\sin\left(\omega t\right) \\ &= I_0 R_0 \sin\left(\omega t\right) + I_0\left(\frac{dR}{dT}\right)\frac{\Delta T_{2\omega}}{2}\left[\sin\left(2\omega t + \phi\right) - \sin\left(\omega t - \phi\right)\right] \\ &= \left[I_0 R_0 \sin\left(\omega t\right) - \frac{1}{2}I_0\left(\frac{dR}{dT}\right)\Delta T_{2\omega}\sin\left(\omega t - \phi\right)\right] + \left[\frac{1}{2}I_0\left(\frac{dR}{dT}\right)\Delta T_{2\omega}\sin\left(2\omega t + \phi\right)\right] \\ &= V_{1\omega}\sin\left(\omega t + \chi\right) + V_{3\omega}\sin\left(3\omega t + \phi\right) \end{aligned} \tag{5}$$

The voltage drop across the heater has components at 1ω and 3ω, and both these components contain information about the periodic temperature rise, $\Delta T_{2\omega}$. As the name suggests, the 3-omega technique uses the voltage component at 3ω to measure the temperature oscillation. The amplitude, $V_{3\omega}$ and phase lag, ϕ of the voltage signal can be directly measured and the voltage amplitude can be directly related to the amplitude of the temperature oscillation by equation (6), where the subscript RMS refers to the root-mean-square value. The 3ω voltage can also be expressed as in-phase (or real) component, *X*, and out-of-phase (or imaginary) component, *Y*, using equation (7).

$$\Delta T_{2\omega} = \frac{2}{dR/dT}\cdot\frac{V_{3\omega,\mathrm{RMS}}}{I_{\mathrm{RMS}}} \tag{6}$$

$$X = V_{3\omega}\cos\phi;\quad Y = V_{3\omega}\sin\phi \tag{7}$$

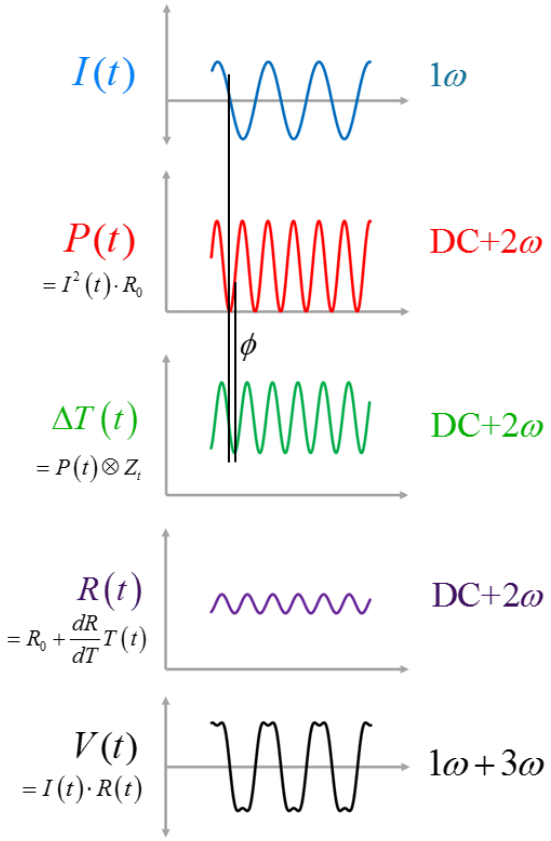

Figure 1 – Schematic relationship between the current and voltage components in a 3ω measurement

In a typical 3ω measurement, the amplitude of temperature oscillation in the heater, ΔT in the frequency domain is related to the amplitude of heating power, P_0 by equation (8). Here, $Z(\omega)$ is called the thermal transfer function, and directly follows from the solution to the heat diffusion equation[17] and is only a function of the geometry and thermophysical properties of the sample material(s). $Z(\omega)$ can be alternatively described as the thermal impedance of the sample. Equations (6) and (8) can be combined to express the 3ω voltage in terms of the thermal transfer function, given by equation (9). Relevant thermophysical properties of the sample are obtained by fitting the experimental 3ω

voltages, measured over a range of frequencies, using equation (9) with the appropriate thermal transfer function.

$$\Delta T_{2\omega} = P_0 Z(\omega) \tag{8}$$

$$V_{3\omega,\mathrm{RMS}} = -\frac{1}{2}\left(\frac{dR}{dT}\right) I_{\mathrm{RMS}}^2 R_0 Z(\omega) \tag{9}$$

1.1.1 General multilayer solution

Traditional 3ω measurements are performed on thin films on substrates. A generalized thermal transfer function for a multilayer-film on substrate with anisotropic thermophysical properties has been derived by solving the heat diffusion equation using the integral Fourier transformation technique and is given by equation (10).[15]

$$\Delta T_{2\omega} = \frac{-P_0}{\pi L k_{\perp,1}} \int_0^\infty \frac{1}{A_1 B_1} \frac{\sin^2(b\zeta)}{(b\zeta)^2} d\zeta,$$
$$\text{with } A_{i-1} = \frac{A_i \dfrac{k_{\perp,i} B_i}{k_{\perp,i-1} B_{i-1}} - \tanh(B_{i-1} d_{i-1})}{1 - A_i \dfrac{k_{\perp,i} B_i}{k_{\perp,i-1} B_{i-1}} \tanh(B_{i-1} d_{i-1})} \text{ and } B_i = \sqrt{\left(\frac{k_{\parallel,i}}{k_{\perp,i}} \zeta^2 + j \frac{2\omega C}{k_{\perp,i}}\right)},\ i = 2,\ldots,n \tag{10}$$

In the above expressions, n is the total number of layers including the substrate, subscript i corresponds to the ith layer starting from the top, k is the thermal conductivity of the layer, d is the layer thickness, b is the heater half-width, and subscripts ∥ and ⊥ correspond to the directions perpendicular and parallel to the film/substrate interface, respectively. For a semi-infinite substrate layer ($i = n$), $A_n = -1$. For substrates with finite thickness, the value of A_n depends on the boundary condition at the bottom surface of the substrate:

$A_n = -\tanh(B_n d_n)$ for an adiabatic boundary or $A_n = -\coth(B_n d_n)$ for an isothermal boundary. This solution is derived by neglecting the thermal mass of the heater and thermal boundary resistances, and by assuming an infinitely long heater. The infinitely long heater assumption is valid (<1% error) if equation (11) is satisfied. The negligible heater thermal mass approximation also holds true for traditional heater materials (gold, platinum, aluminum and other common metals) and dimensions (b ~ 10 μm, thickness ~ 100 nm). The effect of thermal boundary resistance is briefly discussed in Section 1.1.3.

$$\frac{L}{L_p} > 4.7 \text{ for } <1\% \text{ error in infinite line heater assumption} \tag{11}$$

1.1.2 Measurement sensitivity

Theoretically, experimental data can be fit to the multilayer solution to determine any unknown thermophysical property of any layer. However, the confidence in the measurement of a parameter β depends on the sensitivity of the measured signal to that parameter, defined by equation (12).

$$S_\beta = \frac{\partial(\ln \Delta T_{2\omega})}{\partial(\ln \beta)} \tag{12}$$

Based on this definition, a sensitivity of $S_\beta = 0.5$ means that a 10% increase in the parameter β will result in a 5% increase in the signal. The sensitivity ratio S_β / S_γ, on the other hand, describes the error propagation between two parameters β and γ. For example, $S_\beta / S_\gamma = 2$ means that a 10% uncertainty in β and a 20% uncertainty in γ would cause the same magnitude of change in $\Delta T_{2\omega}$. In other words, the measurement is more sensitive to

β than γ. Generally, a higher sensitivity to a parameter implies a lower measurement uncertainty. Since the sensitivity to a parameter is a function of frequency, the experimental frequency range is chosen such that the sensitivity to the parameter to be measured is high relative to others. Prior to a 3ω measurement, it is important to perform a detailed sensitivity analysis to verify whether the desired property can be measured with a high accuracy.

1.1.3 Slope method and differential method

For semi-infinite samples and thin films on semi-infinite substrates, two common approximations are used for data analysis instead of the general multilayer solution. The slope method is a commonly used approximation for a narrow line heater (b/L_p <5) on a bulk substrate of thickness d under the semi-infinite assumption (d/L_p >5). Equation (13) gives the thermal transfer function under these assumptions, and the thermal conductivity of the substrate can be determined directly from the slope of the linear fit between the in-phase (real) component and the logarithmic frequency. The main advantage of the slope method is its independence of the heater width and the heat capacity of the substrate. The thermal conductivity determined using the slope method is within 5% of the exact value provided the conditions listed in equation (13) are satisfied. For anisotropic samples, the thermal conductivity calculated by the slope method yields the geometric mean of the thermal conductivity in the ∥ and ⊥ directions. Figure 2 shows the sample-heater configuration and a sample measurement for the slope method.

$$Z(\omega)=\frac{1}{2\pi k_s L}\left[-\ln\omega+\ln\frac{\alpha}{b^2}+\eta\right]-j\frac{1}{4kL},\ \text{for}\ \frac{b}{L_p}<5\ \text{and}\ \frac{d}{L_p}>5 \qquad (13)$$

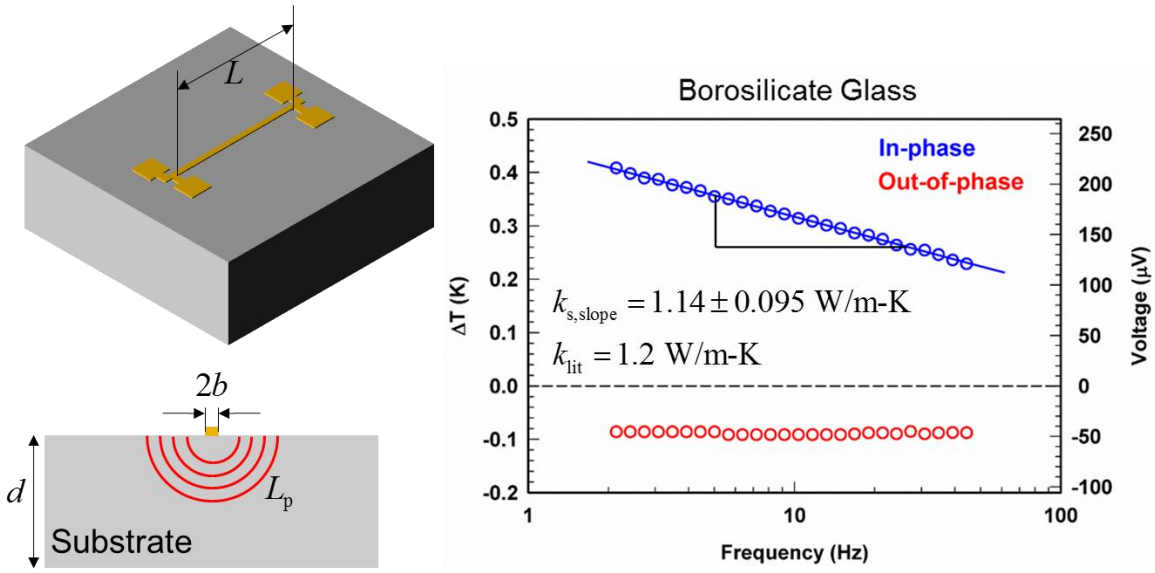

Figure 2 – Schematic illustration of the sample-heater configuration for slope method along with a sample measurement on borosilicate glass. The slope method predicts a thermal conductivity within 10% of the nominal value.

The thermal conductivity, k_f, of a thin film of thickness d on a substrate (thermal conductivity k_s) is determined by measuring the temperature drop across the film. This temperature drop is inferred from the difference in temperature rise of similar heaters deposited on (i) the thin film atop a substrate, and (ii) a substrate without the film. By modelling the heat transfer through the film as one-dimensional conduction, the thermal conductivity can be determined by equation (14). This approach is commonly referred to as the differential method, and the required conditions for its validity are also listed in equation (14). Figure 3 shows a schematic illustration of the sample-heater configuration for a differential measurement.

$$Z_{\text{film}} = Z_{\text{film+sub}} - Z_{\text{film}} = \frac{d_f}{2bLk_f}, \text{ for } \frac{d_f}{L_p} < 5 \text{ and } \frac{k_f}{k_s} < 0.1 \qquad (14)$$

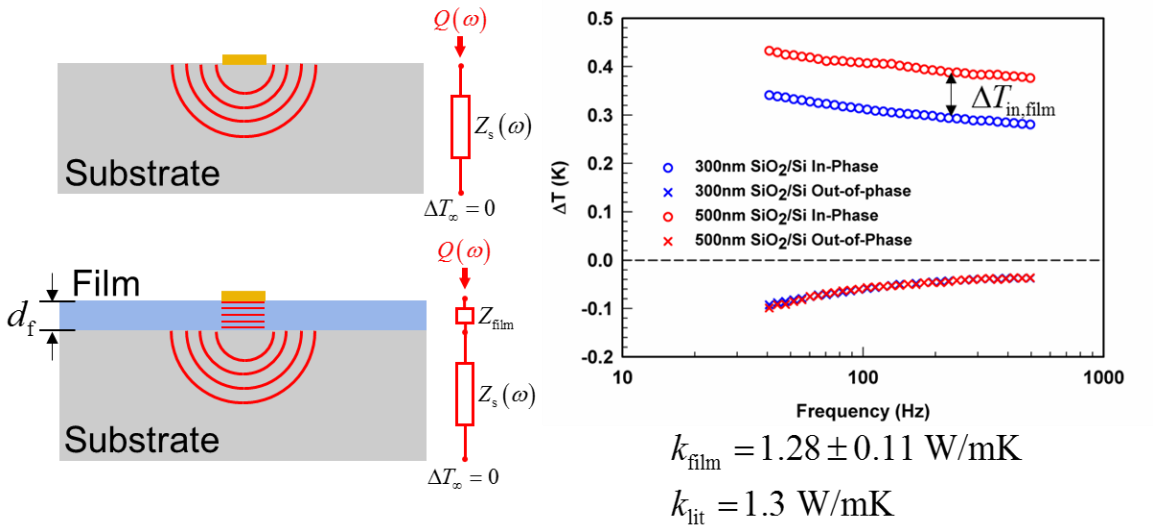

Figure 3 – Schematic illustration of the sample-heater configuration for differential method along with a sample measurement on thermally grown SiO_2 on Si. The differential method predicts a thermal conductivity within 10% of the nominal value.

The differential method does not account for the thermal boundary resistance between the substrate and the film and the measured thermal conductivity is an effective value that includes the thermal resistance of the film and the thermal boundary resistance. While this method is often a good approximation for clean substrates and low thermal conductivity films ($k \leq 0.5$ W/m-K), accounting for the thermal boundary resistance is critical for conductive films. Using the modification illustrated in Figure 4, the differential method can separate the film thermal conductivity from the thermal boundary resistance. 3ω measurements are performed on samples with varying film thicknesses and their respective thermal impedances are measured. The thermal impedances are linearly fit to the film thicknesses to obtain the thermal conductivity. This approach assumes that the film thermal conductivity is independent of its thickness (i.e., thermal transport is not ballistic) and is generally more advantageous than the conventional differential method.

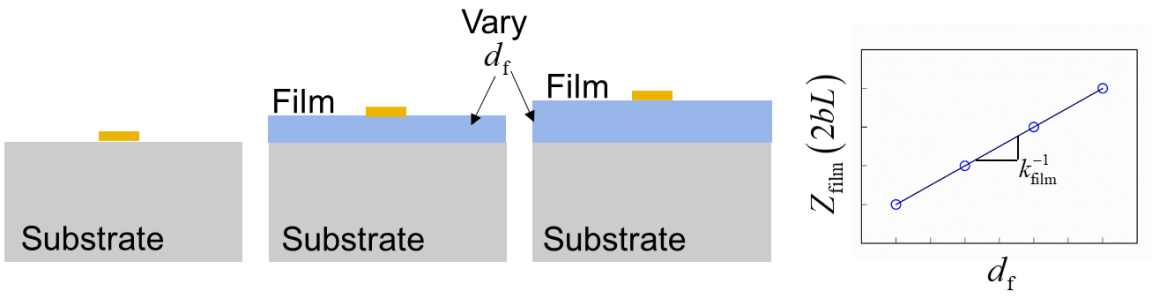

Figure 4 – Modified differential method that can be used to determine thermal conductivity of film independent of the thermal boundary resistance.

1.1.4 Radial multilayer solution

The 3ω technique can also be used to characterize fluids by using a solid metal wire as the heater-thermometer immersed in the fluid. The heat generated in the wire will propagate into the metal core and the fluid proportional to their thermal effusivities. Since metals have higher effusivities (often by 1 or 2 orders of magnitudes), a significant part of the 3ω signal comes from the metal, which decreases the sensitivity of the measurement to the thermophysical properties of the fluid. This issue can be overcome by using a metal-coated fiber, which uses a thin layer of metal (~100 nm) deposited along the circumference of an insulating core. Furthermore, the thinner metal layer reduces the cross-sectional area of the heating layer, which improves the 3-omega voltage per temperature oscillation amplitude, $\Delta V_{3\omega}/\Delta T_{2\omega}$.[18] Therefore, this modification increases the signal-to-noise ratio and improves measurement accuracy for fluids. The radial heat conduction for a *n*-layer concentric cylindrical structure with heat generation in one or more layer has been solved and the general solution is presented below.[18,19] The complex amplitude of 2ω temperature oscillation in the n^{th} layer as a function of the radial position is given by equation. Here, q_n''' is the amplitude of volumetric heat generation in the *n*th layer and I_0 and K_0 are zeroth

order Bessel functions. The first layer has only a coefficient $C_{1,I}$ as $C_{1,K}$ is zero, and the last layer only has the coefficient $C_{\text{last},K}$ as the coefficient $C_{last,I}$ is zero due to the boundary conditions at $r = 0$ and $r \to \infty$, respectively.

$$\Delta T_{2\omega,n}(r) = C_{n,I} I_0(\gamma_n r) + C_{n,K} K_0(\gamma_n r) + \frac{q'''_n}{\gamma_n^2 k_n}, \text{ where } \gamma_n = \sqrt{j\frac{2\omega}{\alpha_n}} \tag{15}$$

The remaining coefficients can be obtained by solving for $\bar{x}$ in the matrix equation (16). $\bar{x}$ is a $2l \times 1$ vector defined by equation (17), where l is the number of interfaces in the multilayer geometry. Likewise, [A] is a $2l \times 2l$ matrix and b is a $2l \times 1$ vector, whose elements are given by equation (18).

$$[A]\bar{x} = b \tag{16}$$

$$\bar{x} = \left[C_{1,I} \;\; C_{2,I} \;\; C_{2,K} \cdots C_{(last-1),I} \;\; C_{(last-1),K} \;\; C_{(last),K} \right]^{\mathrm{T}} \tag{17}$$

For interface $l = 1$:

$$A_{1,1} = -k_1\gamma_1 I_1(\gamma_1 r_1),$$
$$A_{1,2} = k_2\gamma_2 I_1(\gamma_2 r_1),$$
$$A_{1,3} = -k_2\gamma_2 K_1(\gamma_2 r_1),$$
$$A_{2,1} = I_0(\gamma_1 r_1),$$
$$A_{2,2} = -I_0(\gamma_2 r_1),$$
$$A_{2,3} = -K_0(\gamma_2 r_1),$$
$$b_{2,1} = -j\frac{\left(\frac{\alpha_2 q''_2}{k_2} - \frac{\alpha_1 q'''_1}{k_1}\right)}{2\omega}$$

For interfaces $l \geq 2$ and $l \neq last$

$$A_{2l-1,2l-2} = -k_l\gamma_l I_1(\gamma_l r_l),$$
$$A_{2l-1,2l-1} = k_l\gamma_l K_1(\gamma_l r_l),$$
$$A_{2l-1,2l} = -k_{l+1}\gamma_{l+1} I_1(\gamma_{l+1} r_l),$$
$$A_{2l-1,2l+1} = -k_{l+1}\gamma_{l+1} K_1(\gamma_{l+1} r_l),$$
$$A_{2l,2l-2} = I_0(\gamma_l r_l),$$
$$A_{2l,2l-1} = K_0(\gamma_l r_l)$$
$$A_{2l,2l} = -I_0(\gamma_{l+1} r_l)$$
$$A_{2l,2l+1} = -K_0(\gamma_{l+1} r_l)$$
$$b_{2l,1} = -j\frac{\left(\frac{\alpha_{l+1} q'''_{l+1}}{k_{l+1}} - \frac{\alpha_l q'''_l}{k_l}\right)}{2\omega}$$

For interface $l = last$

$$A_{2l-1,l+1} = -k_l\gamma_l I_1(\gamma_l r_l),$$
$$A_{2l-1,l+2} = k_l\gamma_l K_1(\gamma_l r_l),$$
$$A_{2l-1,l+3} = -k_{l+1}\gamma_{l+1} K_1(\gamma_{l+1} r_l),$$
$$A_{2l,l+1} = I_0(\gamma_l r_l),$$
$$A_{2l,l+2} = K_0(\gamma_l r_l),$$
$$A_{2l,l+3} = -K_0(\gamma_{l+1} r_l),$$
$$b_{2l,1} = j\frac{\left(\frac{\alpha_l q'''_l}{k_l}\right)}{2\omega}$$

(18)

The temperature amplitude averaged over the thickness of the metal heater-thermometer layer can be fit to the experimental data to determine thermophysical properties of the outermost liquid/gas layer. Figure 5 shows the sample-heater configuration using a metal-coated fiber and an example measurement using the multilayer radial solution.

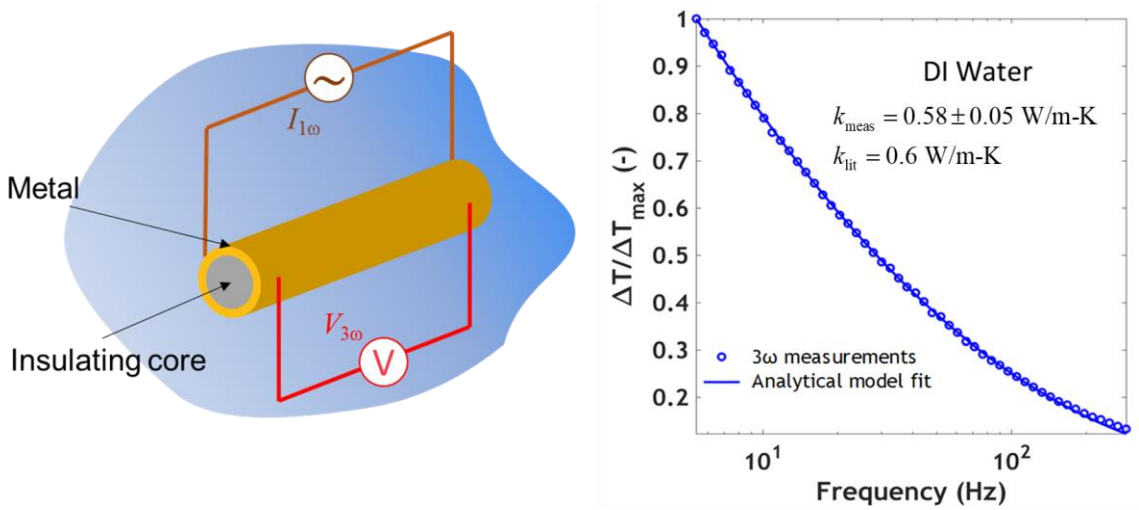

Figure 5 – Schematic illustration of the metal-coated fiber 3ω heater for measurement of liquids and gases. A sample measurement of deionized water is also shown.

1.1.5 Electrically conducting samples

The 3ω technique can be extended to electrically conducting samples, but it is necessary to electrically insulate the sample from the metal heater to prevent Joule heating of the sample. A thin dielectric layer such as SiO_2, Al_2O_3 is deposited on the electrically conducting substrates or films prior to the metal heater fabrication. In metal-coated fiber configuration, the insulating layer is sputtered around the metal layer to insulate it from the conducting fluid on the outside. The 3ω data can be subsequently fit to multi-layer models given by equations (10) and (15) to obtain thermal conductivity of the sample.

For electrically conducting bulk substrates and thin-films on substrates, the slope-method and differential method can still be used, respectively, by fabricating an insulating layer underneath the metal heater. While using these approximations, it is important to ensure that the insulating layer is thermally thin (i.e., thickness << penetration depth) and satisfies the conditions listed in equations (13) and (14).

1.1.6 Uncertainty analysis

Estimating uncertainty is critical in an experimental technique and two approaches are broadly used to determine measurement uncertainties. For the slope method and differential method, a simple error-propagation analysis (EPA) can be used on the simplified analytical solutions. Appendix B describes the EPA in more detail.

For more complex analytical solutions such as the multi-layer geometries, a Monte Carlo computational approach is preferred. The Monte Carlo approach is described as follows: (i) determine uncertainty in experimental data and input parameters, (ii) randomly generate a new set of input parameters and experimental data based on the nominal value and uncertainties, using a normal (or similarly appropriate) distribution, (iii) fit to the parameter of interest using the generated set of data and input parameters, and (iv) repeat steps (ii) and (iii) until the set of fitted values converges to a normal distribution. This method of estimating uncertainty is well-documented in literature[20-22] and is advantageous as it includes uncertainty propagations from all model input parameters and experimental uncertainty. Figure 6 shows an example Monte Carlo histogram for the thermal conductivity of DI water measured in Figure 5. Once the histogram is generated, a 95%

confidence interval is used to quantify the uncertainty of the fitting parameter. The 95% confidence is often conservative, thus resulting in a higher value of uncertainty.

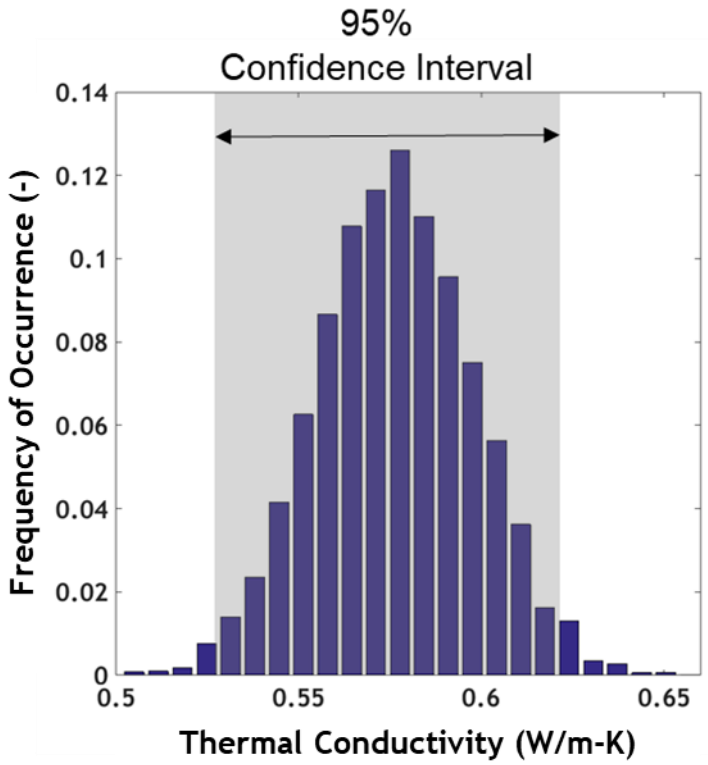

Figure 6 – Uncertainty distribution for thermal conductivity of DI water based on. Monte-Carlo approach. The calculations are based on the data in Figure 5.

1.2 Instrumentation

In a typical experiment, the voltage drop across the heater line contains both 1ω and 3ω components, as mentioned in Section 1.1. While the 3ω component is used for data analysis, the 1ω component is larger by a factor of $\approx 2R_0/\Delta T_{2\omega}\,(dT/dR)$, which is typically around 1000. To improve the measurement accuracy and signal-to-noise ratio, it is common practice to use a simple subtraction circuit to remove most of this 1ω component. The experimental schematic used for 3ω measurements is shown in Figure 7. , the sample heater is connected in series to an adjustable potentiometer, R_b, which has a low temperature coefficient of resistance (typically smaller by 2-3 orders of magnitudes). At the start of the experiment, R_b is set to a value higher than the largest expected value of R_0, and the voltage drop across the ballast is multiplied by a factor $\approx R_0/R_b$ using a digital-to-analog reducer. All resistances are measured in four-probe configuration using a Keithley 2400 Sourcemeter. A sinusoidal current source (Keithley 6221 Current Source) provides the 1ω current to the sample heater. The outputs corresponding to the voltage drop across the sample and the ballast are connected to a precision instrumentation amplifier (AD524 CD) which improves accuracy during data acquisition. These amplifiers also have adjustable gain (1 to 1000) which is useful for measuring voltages down to ~10 μV. Finally, the voltage signals from the sample (A) and ballast (B) are fed to a lock-in amplifier (Standford Research SR 850), which is programmed to read the differential voltage (A-B) and is mostly devoid of the 1ω component. The differential voltage mostly contains information about the relevant 3ω component across the heater, thus making this measurement approach more precise and robust. Since the potentiometer has a low temperature coefficient of resistance, the 3ω component across it is negligible. The voltage

signal from the ballast serves as the frequency reference to the lock-in amplifier. Appendix A details the electronic circuit used in the 3ω measurements.

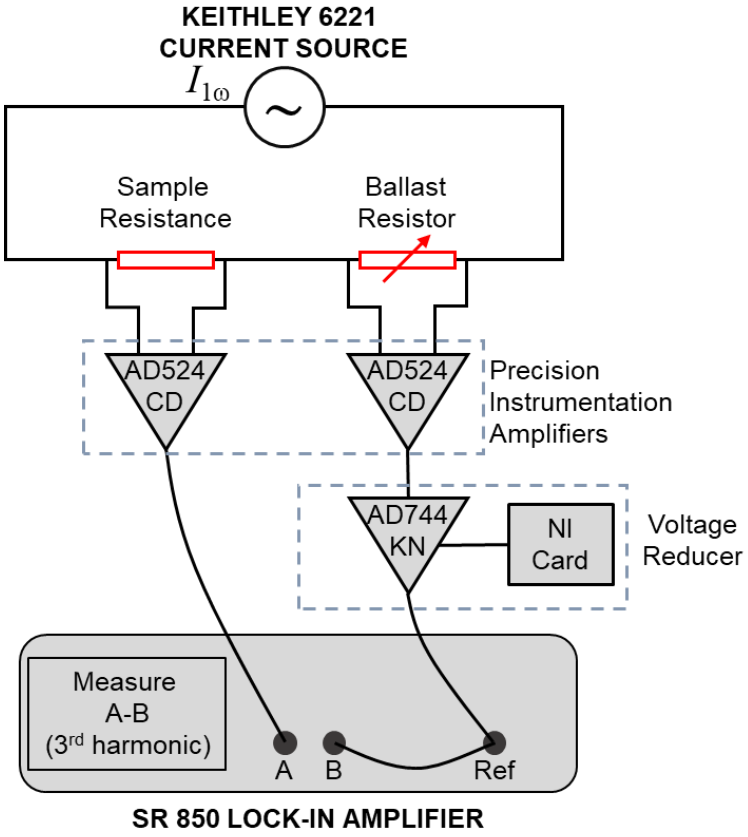

Figure 7 – Schematic of the circuit used to perform 3ω experiments. The precision instrumentation amplifiers improve accuracy during data acquisition and provides adjustable gain. The voltage reducer is used to remove most of the 1ω voltage component.

1.3 Outline and thesis questions

This dissertation consists of five chapters following this introductory chapter and has two key objectives: (i) use existing 3ω methods to explore different application spaces, and (ii) develop variations of the 3ω technique to measure thermophysical properties of suspended films and nanostructures. This **first chapter** provides necessary background on the 3ω technique along with the analytical models that are used for data analysis. The **second chapter** explores the possibility of using two different 3ω heater-thermometers as gas sensors for binary mixtures. The extent to which the measurement sensitivity and power consumption can be optimized is addressed. In the **third chapter**, an empirical model to predict temperature-dependent thermal conductivity of amorphous polymers is developed. The model is validated using experimental 3ω measurements.

The **fourth chapter** discusses a variant of 3ω technique that is useful to measure in-plane thermal conductivity of suspended films. The data analysis can be performed using a simplified 1-D model and the chapter discusses the limits of validity of this model. This technique is then used to characterize a few semiconducting polymers, including recently developed n-type thermoelectric polymers. The **fifth chapter** discusses a modification of 3ω technique that can measure thermal conductivity of nanostructures. Measurements are performed using a platform with four suspended microbridges with the nanowire laid across. Data analysis is performed using a simplified thermal circuit. These aspects will be explored with the goal of answering the following four critical questions:

What are the limits of sensitivity achievable using a gas sensor based on 3ω technique? And to what extent can a balance between sensitivity and power consumption be realized?

Electrothermal gas sensor capable of detecting concentrations based on their thermal properties often use wheat-stone bridge configuration. Since the 3ω technique has high measurement accuracy and precision coupled with a low heating power, a gas sensor based on 3ω technique can achieve a balance between sensitivity and power consumption. Chapter 2 focuses on exploring the limits of sensitivity with a minimal power consumption (~1 mW) of two gas sensor geometries – a suspended microbridge sensor and a metal-coated fiber sensor. The sensitivities, and power consumption of both sensors for four binary gas mixtures is quantified.

How accurately can an empirical model based on experimental 3ω data predict temperature-dependent thermal conductivity of amorphous polymers?

Experimental temperature-dependent thermal conductivity data of amorphous polymers follow a monotonically increasing trend, with two plateaus – the first around 10 K and the second around room temperature. These plateaus can be attributed to the different vibrational modes in polymers, which are different from phonons in crystalline materials. Chapter 3 focuses on developing an empirical model that is based on kinetic theory, and results of molecular dynamics and numerical simulations. The empirical model is fully characterized by fitting to experimental data of multiple amorphous polymers. The predictive accuracy of this model is quantified over temperatures ranging between 1 and

300 K. The model is developed and validated using 3ω measurements of temperature-dependent thermal conductivity.

To what degree of accuracy can the 3ω technique measure anisotropic thermal conductivities in polymers? What degree of anisotropy in thermal conductivity is observed in semiconducting polymers?

Anisotropic thermal conductivity directly affects the performance of polymers in applications such as organic thermoelectrics, motivating efforts to accurately measure in-plane thermal conductivity of polymer films. A modified suspended film 3ω method is proposed in chapter 4 that can accurately determine the in-plane thermal conductivity of polymer thin films without requiring (often detrimental) microfabrication that are commonly reported in literature. The heat transfer in this configuration can be approximated by a 1D model, and the geometric and experimental guidelines for the validity of this approximation are explored. This approach is used to measure in-plane thermal conductivities of semiconducting polymers, including recently developed n-type thermoelectric polymers. By measuring through-plane conductivities using conventional 3ω methods, thermal anisotropy in these polymers is determined.

How accurately can a variant of 3ω technique measure thermal conductivities of nanowires and other nanostructures?

Electrothermal techniques are commonly used to measure thermal conductivities of 1D micro/nanostructures. In chapter 5, a suspended platform technique with four Pt/SiN_x microbridges, each of which can be used as a heater/thermometer is used to measure temperature-dependent thermal conductivity of axially modulated nanowires. While a

steady-state (DC) approach is reported in literature, using a frequency-domain (AC) approach can improve measurement accuracy and confidence. An AC approach is proposed using a variant of 3ω technique, and data analysis is performed using an approximated thermal impedance network. After validating this approach, it is used to measure thermal conductivities of axially modulated nanowires to study the effects of modulation length and diameters on their thermal transport.

By answering these questions, this dissertation aims at exploring a few applications of the 3ω technique, including modifications that can aid in accurately characterizing thermal anisotropy in polymer films and nanostructures. The modifications and applications discussed here can be extended to other research spaces, some of which are briefly outlined in the **sixth chapter**.

CHAPTER 2. GAS SENSING USING THE 3-OMEGA TECHNIQUE

2.1 Background

For the past four decades, gas sensors, detectors, and analyzers have been widely used to measure the composition of gas mixtures or to detect the presence of a particular species in gases.[23] Most of the conventional gas sensors are based on electrochemical or chemo-resistor technology due to their high selectivity. Some of these chemical sensors respond slowly and require calibration. In many cases the transducer response is nonlinear, which makes calibration difficult.[24] An alternative approach to chemical sensors are thermal-physical sensors. In some of these sensors, Joule heating in a microbridge heats the surrounding gas, which in turn changes the thermal-physical properties of the sensor. Sensors of this type which are based on semiconductor technologies offer improved gas sensing due to their small size, simple operation, high sensitivity, and integration with circuits.

Conventional electro-thermal gas detectors have been used as pellistors,[25] which are solid-state devices used to detect combustible gases by measuring the temperature of a hot element covered with a catalyst (e.g., platinum). The additional heat released from the oxidization of the combustible gas changes the temperature of the sensing element. Conventional pellistors require large power consumption (hundreds of milliWatts to Watts) and have response times on the order of tens of seconds. Furthermore, their relatively large footprints compared to integrated circuits limits their use in compact applications. To

reduce the size and power consumption, micro-hot-plates have been developed based on MEMS technology.[26,27] An electro-thermal sensing mechanism whose detection relies on the thermo-physical properties of gases and does not rely on gas adsorption and reaction with catalyst films, have the potential to respond faster and operate in a continuously with low degradation over time. Specifically, miniature TCDs are highly desirable for gas chromatography.[28,29] Current manifestations use a platinum heater resting on a silicon nitride membrane as the sensor element,[30] where the total size of membrane structure may exceed 0.5 mm. In one of the latest advancements, a doped polysilicon microbridge with very low thermal mass was developed that allows for ultra-fast thermal response.[31] Nanoscale bridge type gas sensors using nanotubes,[32] nanowires,[33] and nanobelts[34] have also been fabricated. However, unlike MEMS technology, nanosensors are not commercialized for practical working environments due to fabrication and reliability issues.

2.2 Microbridge Gas Sensor

In this chapter, a variation of the 3ω technique is explored for optimizing power consumption and sensitivity in binary gas mixtures of He, Ar, CO_2 and CH_4 in N_2. The heater is a 100 μm long microbridge made from a 1 μm thick doped polysilicon layer, suspended on a 10 μm silicon dioxide sacrificial layer. The sensor is passivated with a 200 nm silicon nitride layer shown in Figure 8. This microbridge is exposed to the binary gas mixture under test and serves as the heater-thermometer, like in conventional 3ω measurements.

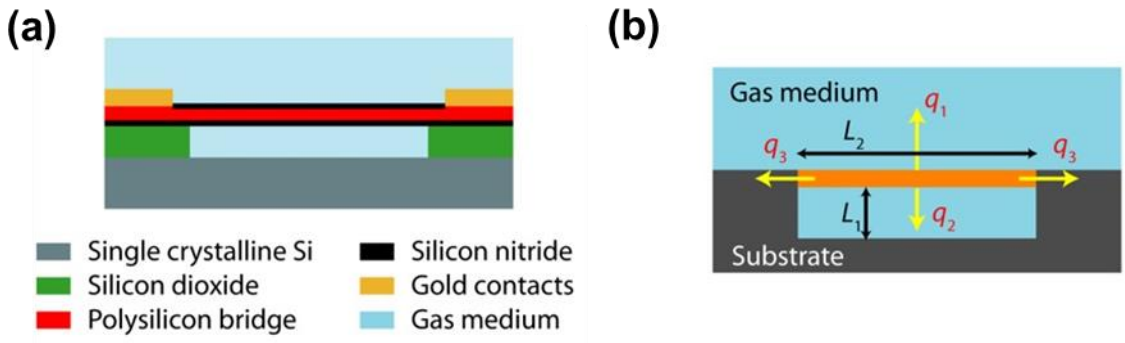

Figure 8 – Microbridge sensor schematic indicating (a) the sensor's material cross section, (b) the possible heat flow direction in the sensor-gas system. The characteristic heat transfer lengths are indicated as L_1 and L_2.

2.2.1 Sensor Fabrication

The microbridge sensor used here is the smallest polysilicon TCD reported in literature.[31] A brief description of the fabrication process is shown in Figure 9. First, a 10 µm SiO_2 sacrificial layer is thermally grown on a Si wafer (step 1). Next, a thin nitride layer (~0.2 µm) is deposited by a Low-Pressure Chemical Vapor Deposition (LPCVD) furnace (step 2) using 100 sccm of dichlorosilane and 17 sccm of ammonia at 835 ˚C. The nitride layer serves as the protection layer during the removal of SiO_2 sacrificial layer. This is followed by the deposition of ~1 µm polysilicon (step 3). Then p-type doping of the polysilicon layer is carried out using boron source at 1050 ˚C for 2 hrs, followed by drive-in process at the same temperature for 1 hr. The polysilicon layer is then patterned using a technique called mix and match or double exposure, in which the pattern is exposed electron-beam lithography and deep UV lithography separately but into the same resist layer. This is followed by an Inductively Coupled Plasma (ICP) etch (step 4). The patterned polysilicon wafer is cleaned in Piranha solution and is followed by the growth of another LPCVD nitride layer (~0.2µm) to sandwich the polysilicon beams (step 5). Then, UV

lithography and reactive ion etching (RIE) are carried out to open electrical contact windows at the top surface of the bridge anchors (step 6). Step 7 involves fabrication of the contact pads. The electrical contact is first defined by patterning the resist for runners. To deposit the runners, 30 nm thick chromium is evaporated at a rate of 0.5 Å/s, followed by deposition of 250 nm thick platinum at 1 Å/s. The chromium layer acts as the adhesion layer. This is followed by patterning the resist for the contact pads. The contact pads are deposited by evaporating 30 nm thick chromium layer at a rate of 0.5 Å/s (adhesion layer), followed by 450 nm thick gold layer at a rate of 2 Å/s.

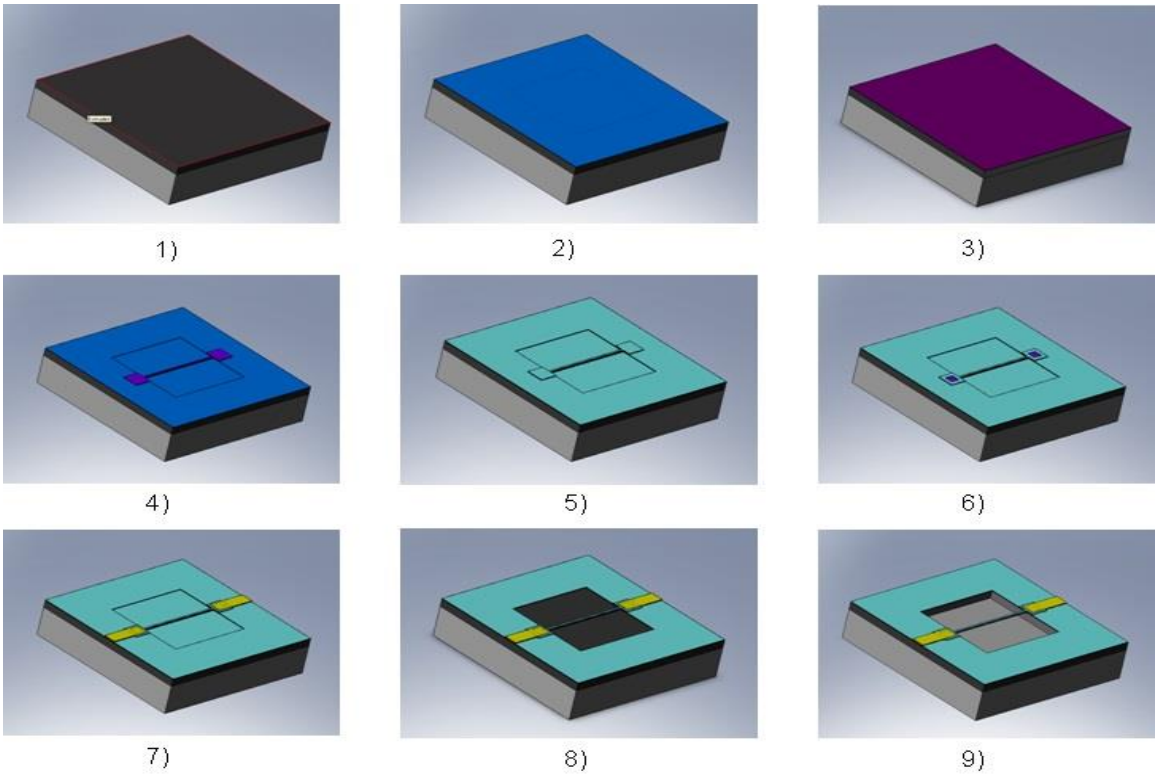

Figure 9 – Microfabrication flowchart for a microbridge heater/thermometer

To release the beams and form the suspended bridge, etch windows are opened in alignment with the polysilicon beams using UV lithography and RIE of the nitride layer

(step 8). The final step on the wafer process is using Buffered Oxide Etch (BOE 6:1) to etch away the exposed SiO_2 material (step 9). Finally, the wafer is diced, and the dies are wire-bonded to an IC package for use as gas sensors. Each sensor consists of an array of 16 bridges. The sensor is designed with two isolated anchors connecting one beam so that each bridge can be individually addressed. Figure 10 shows an optical microscope and SEM image of the polysilicon microbridge.

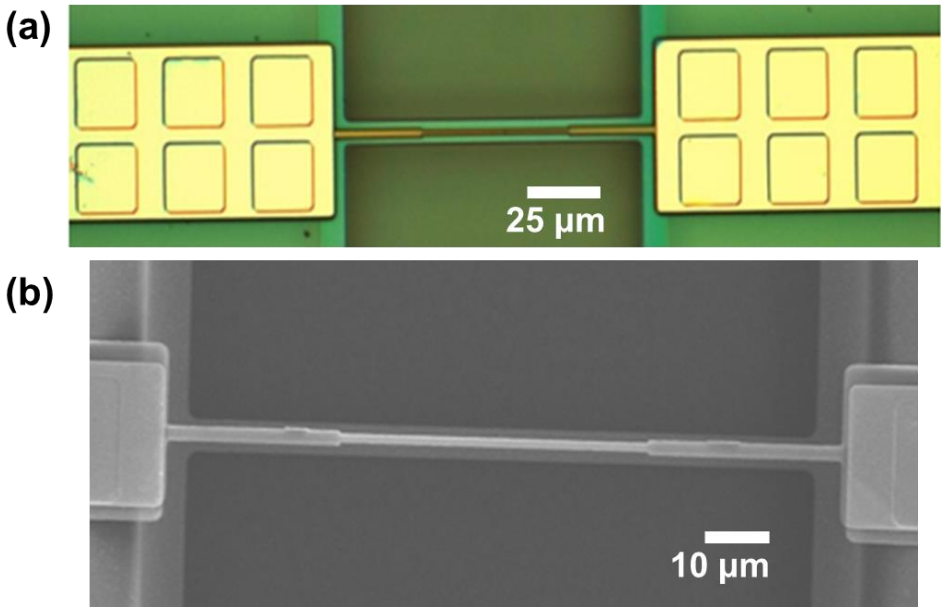

Figure 10 – (a) Optical microscope image and (b) electron microscope image of the suspended polysilicon microbridge

2.2.2 Experimental Set-Up and Measurements

The polysilicon microbridge is placed in a dual in-line package and wired in a four-point probe configuration. The sensor is placed in an (quiescent) isothermal chamber and the temperature is increased from 24 to 69 ^{o}C uniformly to determine *dR/dT* (4.09 ohm/^{o}C).

Figure 11 illustrates the experimental set-up used for the 3-omega measurements. 300 cu. ft. gas cylinders containing ultra-high purity nitrogen and a mixture of 5% trace gas (He, Ar, CO_2, CH_4) in N_2 are used to supply the gas mixture for the experiments. Using accurate mass flow controllers, flow is regulated into the test section with trace gas concentrations varying from 0 to 5%, in increments of 0.5%. The volume of the test section is 200 mL and the flow into that section is considered quiescent. If the gas mixture surrounding the sensor is quiescent, convective heat transfer can be neglected and conduction will dominate the heat transfer between the sensor and the surroundings. The amplitude and phase signals can then be directly related to thermal properties (i.e., thermal conductivity and heat capacity) of the sensor and gas media. Since these thermal properties are functions of the composition of the gas mixture, the voltage and phase lag can be directly related to gas composition.

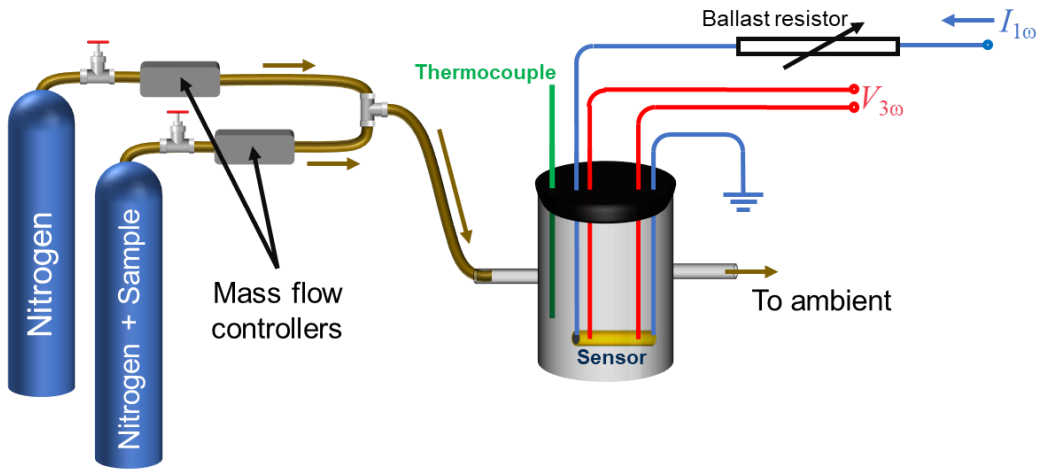

Figure 11 – Schematic of the experimental set-up highlighting the gas flow system and the sensor configuration.

As an illustration, at low modulation frequencies (f < 100 Hz), the sensor-gas system undergoes quasi-steady heating leading to larger temperature amplitudes and near

zero phase lag. Due to the large penetration depths at these frequencies, the thermal transport is dominated by the thermal properties of the gas mixture, in particular, the thermal conductivity. Therefore, the effect of concentration on amplitude is more pronounced at lower frequencies. At high frequencies (f > 10 kHz), the penetration depth is so small that most of the temperature oscillation is constrained to within a small volume inside the sensor. Thus, there is little sensitivity to the gas mixture. At intermediate frequencies, the amplitude is dictated by the thermal effusivity of the gas mixture. The phase lag at these frequencies is a measure of the thermal response of the sensor-gas system and is a strong function of the thermal effusivity of the gas mixture. The phase lag is most sensitive at an intermediate characteristic frequency, which depends on the physical environment and geometry of the sensor-gas system. The characteristic frequency of the system based on the geometry and gas properties is defined by equation (19), where α_{sys} is the effective thermal diffusivity of the sensor-gas system and is bounded between the thermal diffusivity of the sensor, α_{sensor}, and the gas mixture, $\alpha_{gas.}$ To determine a nominal range for the characteristic frequency, α_{sensor} is approximated as the thermal diffusivity of polysilicon and α_{gas} is approximated to be the thermal diffusivity of $N_{2,}$ since the gas mixtures tested are >95% N_2. The length L_c is a characteristic heat transfer length of the sensor-gas system, which is related to the geometric dimensions of the sensor. Figure 8(b) illustrates the possible directions for conduction. Since the gas medium is of interest, the length L_2 is chosen as the characteristic length, since it corresponds to the length that heats the gas and the length over which the temperature oscillation is averaged. Using equation (19), the characteristic frequency of the sensor-gas system is estimated to be between 1.40 kHz and 1.65 kHz based on the bounds of thermal diffusivity. As will be demonstrated in

the next section, this estimate is in good agreement with a natural characteristic frequency at 1.525 kHz that results from the measurement where the bridge is most sensitive to gas composition.

$$f_c = \frac{\alpha_{\text{sys}}}{2\pi L_c^{\,2}} \tag{19}$$

Experiments are performed at three different current amplitudes, I_0, of 0.2, 0.3 and 0.4 mA, which is useful in understanding the dependence of measurement sensitivity on sensor power consumption. A frequency range of 100-12k Hz is chosen for 3ω experiments. Figure 12 shows the raw 3-omega measurements for He-N_2 mixture for a current amplitude of 0.4 mA. Similar data for all current amplitudes and all gas mixture concentrations are observed.[35] At lower frequencies (~100 Hz), the observed trend in amplitude can be explained by means of the thermophysical properties of the gases listed in Table 2.[36] Since Helium has a higher thermal conductivity than N_2, the gas mixture conducts heat from the sensor better as the concentration of He in N_2 increases. Thus, the ΔT of the sensor decreases as the concentration of He in N_2 increases. At higher frequencies (~ 1.5 kHz), the magnitude of phase lag decreases as concentration of He in N_2 increases. Since helium has a higher thermal effusivity than N_2, the sensor responds quicker (i.e., smaller magnitude of phase lag) as the concentration of He in N_2 increases.

Table 2 – Relevant thermophysical properties of the gases and polysilicon microbridge

Material	Thermal conductivity (W/m-K)	Density (kg/m^3)	Specific heat (J/kg-K)	Thermal diffusivity (m^2/s)
Nitrogen	0.0258	1.123	1041.8	2.21×10^{-5}
Methane	0.0346	0.644	2235.8	2.40×10^{-5}
Helium	0.1560	0.160	5193.0	1.87×10^{-4}
Argon	0.0177	1.603	521.5	2.12×10^{-5}
Carbon dioxide	0.0168	1.773	852.5	1.11×10^{-5}
Polysilicon	40.0	2320	678.0	2.55×10^{-5}

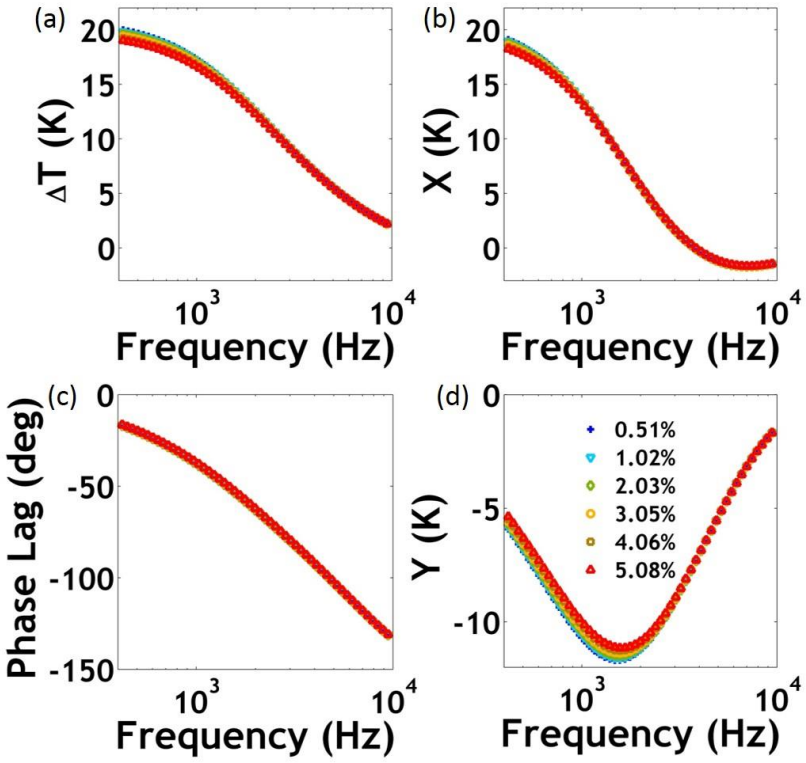

Figure 12 - The raw 3ω signals for the He-N_2 mixture, for six different compositions, and a current amplitude of 0.4 mA. Figure (a) and (c) indicate the amplitude and phase lag, while (b) and (d) indicate the in-phase (real) and out-of-phase (imaginary) components of the amplitude, respectively

2.2.3 Composition Curves

The raw 3ω signals can be expressed as differential signals between the gas mixture and pure N_2 (e.g., $\Delta T_{mix} - \Delta T_{pure\ nitrogen}$), which will allow to develop direct relationships between experimental measurements and gas composition. Figure 13 shows the differential signals (ΔT, ϕ, X, and Y) for He in N_2. Similar plots can be developed for other mixtures as well.[35] To study the effect of mixture composition on this differential 3ω signal, the average of the differential ΔT and X between the frequencies 300 and 700 Hz is considered. The average (which is over 14 points) is used instead of a single point value to smooth over (noise) fluctuations that may be present in a single differential point. These average values are then plotted against the mixture concentration (Figure 14a-b) of trace gas for different mixtures and for different amplitudes of input current. A linear fit between the differential signal and concentration is performed and are the gas composition curves for the sensor. Similar curves can be developed for the other gas mixtures. Using these composition curves for ΔT and X, it is possible to determine the composition of a binary gas mixture. By measuring the 3ω signal for a binary mixture, the linear composition curve for the corresponding signal will result in a unique value of concentration of the trace gas. It is also interesting to note that there is an isosbestic point in X; this isosbestic point occurs at the sensors' characteristic frequency 1.525 kHz.

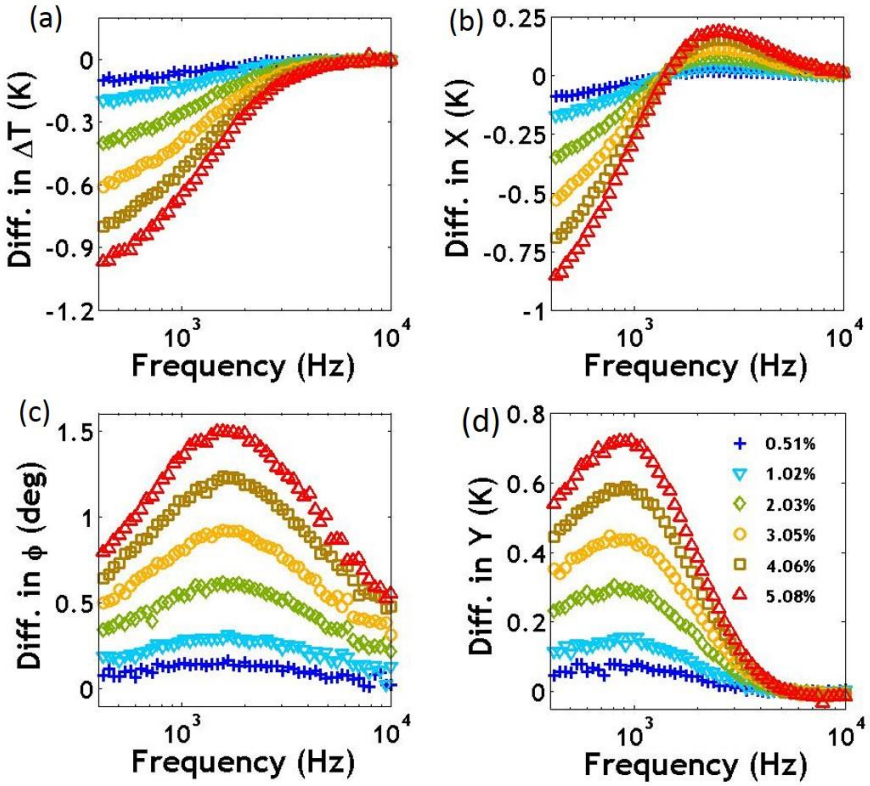

Figure 13 – Differential signals of amplitude, phase, *X*, and *Y* for different compositions of He-N_2 mixtures with a current amplitude of 0.4 mA. An isosbestic point exists in the differential *X* signal at the characteristic frequency (1525.5 Hz) of the sensor-N_2 system

Similar to the differential amplitude and *X*, the differential phase lag signal is plotted against frequency for different gas mixtures, and at different amplitudes of current (Figure 14c). The resulting composition curve based on raw phase lag signal has the advantage of being independent of the current amplitude and not requiring individual sensor calibration. Since the phase is sensitive to the gas composition near the characteristic frequency of the system, we average over frequencies centered on the characteristic frequency of 1.52 kHz in the range $f_L < f_c < f_U$, where f_L (1.4 kHz) and f_U (1.65 kHz) correspond to the frequency bounds of the characteristic frequency. This corresponds to

averaging over 4 points. The data for differential phase, averaged over the frequency range defined by f_L and f_U is plotted against the concentration of He in N_2 for three different current amplitudes. Since the phase is independent of the amplitude of current, a single linear fit is used for the composition curve. Lastly, a composition curve based on the differential *Y* (Figure 14d) can also be developed by averaging over the frequency range between 500 and 1600 Hz. The range is chosen to include the maxima in the differential *Y* signal.

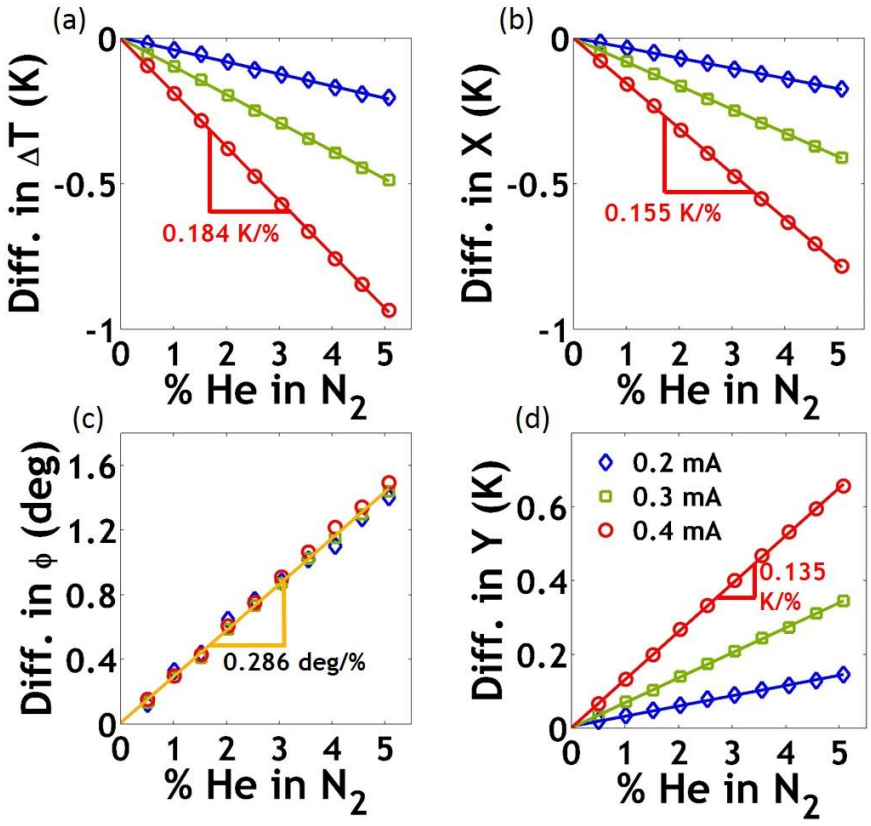

Figure 14 - Composition curves for the gas mixtures of He in N_2. A linear trend between the differential signal and the concentration is observed. The phase signal is independent of the current amplitude. The slopes of the linear fits for the differential amplitude, *X*, *Y* and phase (at a current of 0.4 mA) are shown

An additional composition curve can be developed based on the out-of-phase 3ω component (*Y*). It can be observed in Figure 12 that *Y* shows a minimum within the bounds of the estimated characteristic frequency. For each gas mixture, the *Y* data is fit to a polynomial function of the *f* to determine the frequency at which the minimum occurs. This frequency is only a function of mixture composition, and therefore by determining the frequency of the minimum in *Y*, the composition of an unknown binary mixture can be determined. Figure 15 shows the plot of the experimentally determined minimum frequency vs. the concentration and the subsequent linear fit. It can be noticed that the four gas mixtures converge in pure nitrogen (0%), which corresponds to the experimentally determined characteristic frequency of the sensor-gas system in pure N_2.

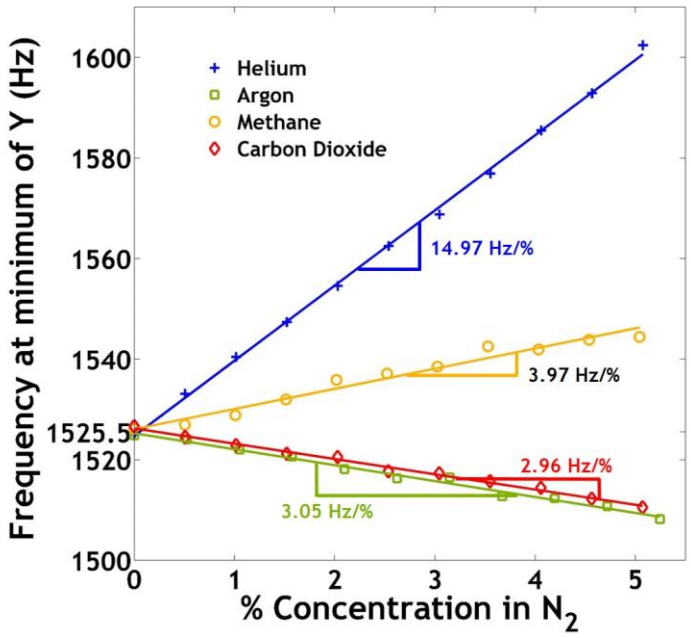

Figure 15 – The frequency at which *Y* has a minimum versus concentration for different binary mixtures with a current amplitude of 0.4 mA. A linear fit and the resulting slopes are indicated. The four curves converge to the same frequency at a concentration of 0 %, which is the characteristic frequency of the sensor-N_2 system

2.2.4 Measurement Sensitivity

To determine the measurement sensitivity, an uncertainty analysis is performed on the differential 3ω signals. The composition curves based on ΔT, ϕ, X, and Y for a current amplitude of 0.4 mA are considered for the uncertainty analysis. At lower currents, the 3ω signal is so small that it is close in magnitude to the ambient noise, which results in fluctuation in the signals at 0.2 mA. Hence, a higher magnitude of current results in a stronger signal but comes at the cost of consuming more power. Since the differential 3ω signal is a linear function of the concentration, the uncertainty in the measured concentration of a sample can be calculated as

$$\delta(\%) = \left| \frac{\delta(\Delta signal)}{m} \right| = \left| \frac{\sqrt{2} \cdot \delta(signal)}{m} \right| \tag{20}$$

where $\delta(\Delta signal)$ and $\delta(signal)$ are the uncertainty in differential signal and the raw signal as measured by the 3ω instrument and m is the slope of the composition curve corresponding to that signal. The uncertainty given by equation (20) depends on the gases present in the mixture, the 3ω signal on which the composition curve is based on, and the amplitude of current (except in the case of phase composition curve). The uncertainties associated with the raw measured amplitude, phase lag, X and Y signals are 0.0061 K, 0.076˚, 0.0073 K and 0.0097 K respectively. A similar uncertainty analysis can be performed on the composition curve involving the minimum Y frequency. Table 3 lists the measurement sensitivity (uncertainty) for different gas mixtures based on the five composition curves. The measurement sensitivity of the sensor is ~1000 ppm and is achieved with a sensor power consumption of 0.25 mW. While the sensitivity of this

microbridge TCD isn't the best in its class, the power consumption is at least an order of magnitude lower than the rest, making it useful for low power applications.

Table 3 – Measurement sensitivity (uncertainty) of different gas mixtures for different composition curves. All values are in %.

Gas mixture	Composition curve based at 0.4 mA				
	ΔT	ϕ	X	Y	Freq. for Y_{min}
He in N_2	0.047	0.376	0.067	0.102	0.071
Ar in N_2	0.192	1.739	0.272	0.443	0.351
CO_2 in N_2	0.216	1.659	0.313	0.473	0.362
CH_4 in N_2	0.190	1.558	0.277	0.416	0.270

2.3 Metal-Coated Fiber Sensor

Gas sensing with 3ω can be extended to sensor geometries beyond the suspended microbridge. While the microbridge has a measurement sensitivity of ~1000 ppm, a significant portion of the heat is dissipated within the conducting microbridge and to the solid substrate, which limited the sensitivity to the gas medium. An alternative design involving an insulating glass fiber circumferentially coated with a thin layer of metal is explored.[19]

2.3.1 Sensor Fabrication

The metal layer is deposited using a conventional sputtering system (Unifilm Multisource Sputtering System, IEN, Georgia Tech). To achieve uniform cylindrical coating, the fibers are strung tautly onto a spool, which is uniformly rotated with the motor in the sputtering system as shown in Figure 16. The deposition lathe ensured uniform circumferential coating. Since the deposition crystal monitor is calibrated for deposition in a rectangular plane, the thickness deposited on the sensors is smaller by a factor of π, which

results from the ratio of the fiber's actual surface area ($\pi \times$ diameter $\times$ length) to its projected area (diameter $\times$ length).[18] The sputterer is programmed to deposit a 10 nm titanium adhesion layer, followed by a ≈150 nm of gold. The fiber is characterized using a SEM to determine the exact thickness and to verify the uniformity of the gold layer along the circumference of the fiber. This is done by measuring the metal layer's thickness at over 10 points along the fiber's circumference.[19] The resulting thickness of the metal layer is 135±11 nm. Figure 17 shows an SEM image of the fiber's cross section.

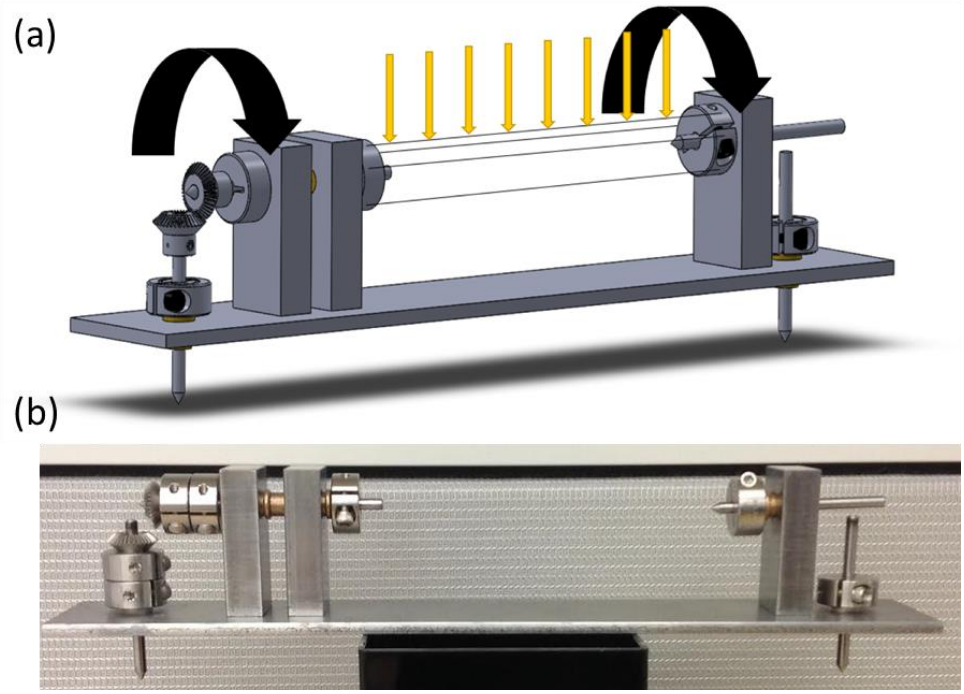

Figure 16 – (a) Schematic showing the deposition lathe with fibers strung onto the rotating spool. The black arrows indicate the direction of rotation of the spool and the golden arrows indicate the direction of gold sputtering. A bevel gear is used to convert the plane of rotation from the default horizontal plane to the vertical one with the spool. (b) A picture of the deposition lathe used.

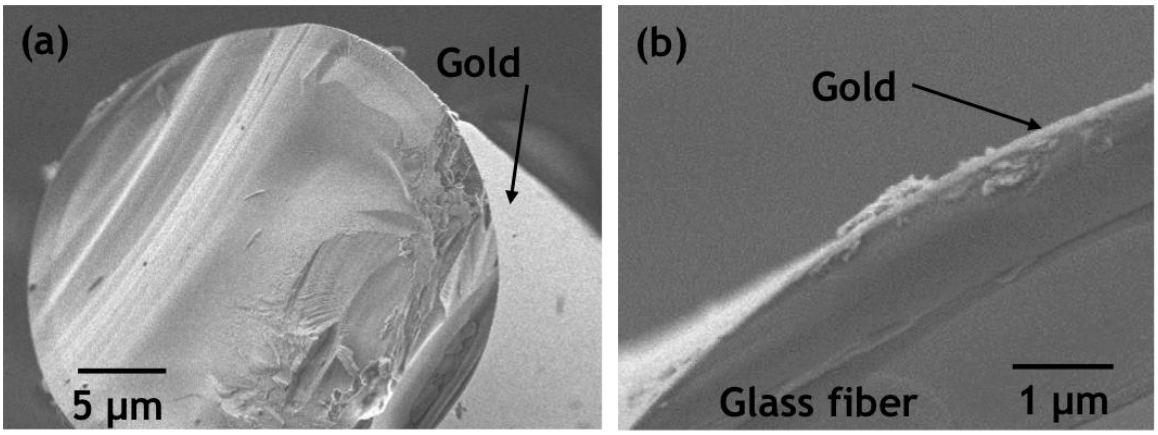

Figure 17 – (a) The cross-sectional image of the metal-coated fiber highlighting the gold layer. (b) A magnified image of the gold layer on the fiber. The uniformity of the coating is verified by measuring the thickness of the gold at several points along the circumference. An Energy Dispersive X-Ray Spectroscopy (EDS) study is also carried out on the fiber to verify the gold thickness.

2.3.2 Experimental Set-up and Composition Curves

The gold-coated fiber is placed in a dual in-line package and wired in four-point configuration. Electrical contacts to the fiber are made using DuPont© CB028 silver conductive paste. The sensor is placed in an isothermal chamber whose temperature is uniformly increased from 20 ˚C to 50 ˚C in 5 ˚C increments and *dR/dT* is measured to be 0.1155 ± 0.008 ohm/˚C. An experimental set-up similar to the one described in Section 2.2.2 is used to characterize this sensor. 3ω experiments are performed with a sourcing current amplitude of 12 mA, between frequencies of 0.5 and 2000 Hz.

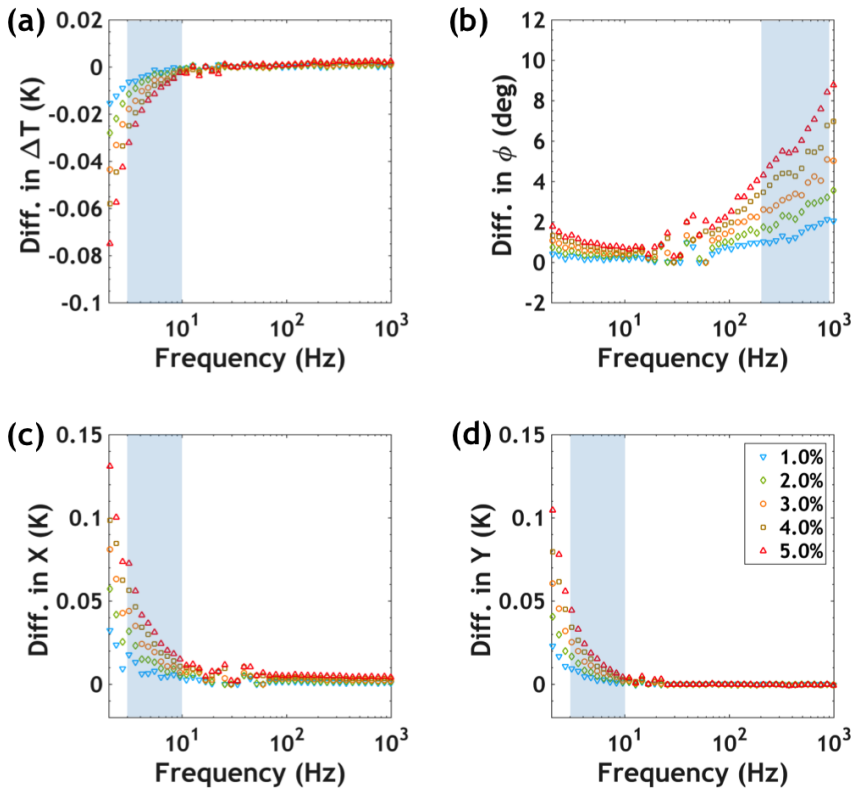

Figure 18 – Differential signals of amplitude, phase, *X* and *Y* vs frequency for different concentrations of He in N_2. The sensitivity of the different signals at different frequencies can be readily noticed. The frequency range of high sensitivity considered for the composition curves is highlighted in each of the four figures.

Data analysis procedure, similar to the one used for the microbridge TCD is adopted here. Figure 18 shows the differential 3ω signals for He in N_2 for different concentration of the trace gas (He). The regions of maximum sensitivity of each differential signal are also highlighted in the figure. The average of the differential signals in the corresponding frequency ranges are then plotted against concentration to obtain composition curves. The composition curves based on different 3ω signals for different gas mixtures are shown in Figure 19.

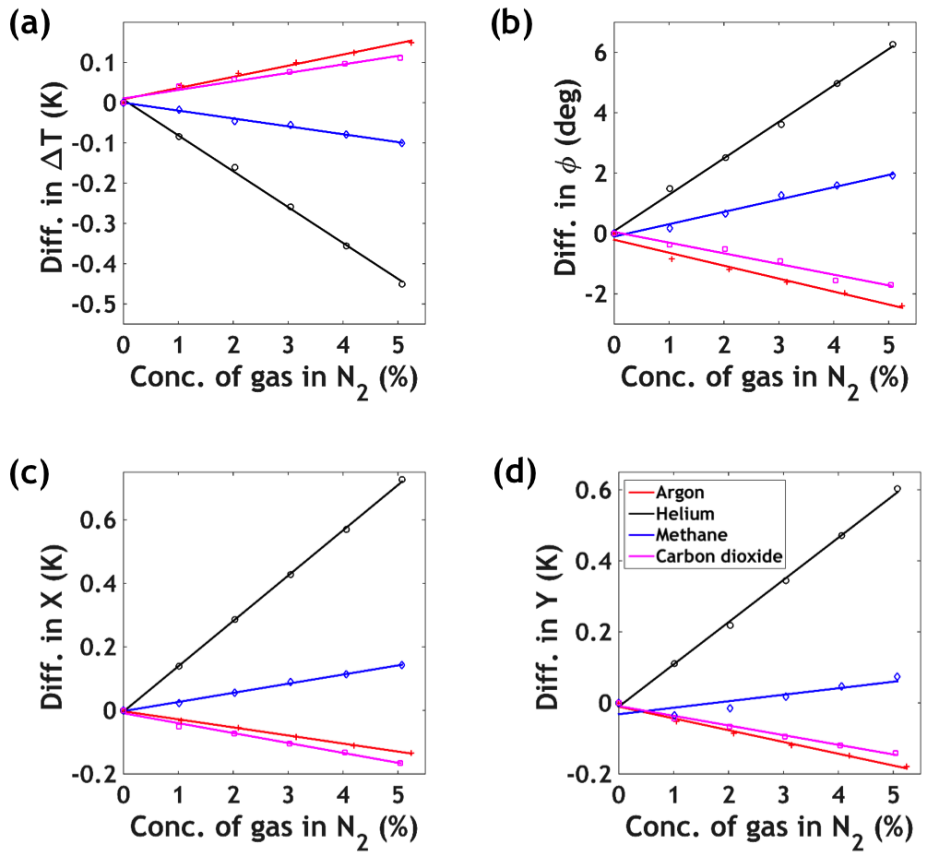

Figure 19 – Composition curves for all four gas mixtures based on differential 3-Omega signals. A linear trend between the averaged differential signal and concentration is observed for all cases, as indicated by a linear fit for the data. The composition curve based on phase lag is independent of the magnitude of sourcing current.

2.3.3 Measurement Sensitivity

Equation (20) is used to determine the measurement uncertainty based on the composition curves for the metal coated sensor. These values are summarized in Table 4. These values are achieved with a sensor power consumption of ~5 mW. The improved measurement sensitivity of the metal-coated fiber compared to the microbridge can be readily observed. This is partly attributed to the sensor design which minimizes axial heat dissipation, and partly attributed to the higher sensor power consumption.

Table 4 - Measurement sensitivity (uncertainty) of different gas mixtures for different composition curves. All values are in ppm.

Gas mixture	Composition curve based at 12 mA			
	ΔT	ϕ	X	Y
He in N_2	8.1	801.0	6.8	8.5
Ar in N_2	18.7	916.4	43.3	22.9
CO_2 in N_2	35.6	2400	32.7	37.9
CH_4 in N_2	29.9	756.1	39.0	47.0

2.4 Summary

In this chapter, the 3ω technique is extended for the purposes of gas sensing in binary mixtures. Two different sensor geometries, a polysilicon microbridge and a gold-coated fiber, are explored. The microbridge sensor can resolve gas concentrations of < 0.5 % and as low as 0.07 % if the thermal properties of the two gases are widely different. This design, however, has minimal sensor power consumption compared to other TCDs thus providing a good compromise between sensitivity and power consumption. Composition curves have been developed for four differential signals, all of which showed a linear response to the concentration, based on this geometry that demonstrates the sensor's ultimate sensitivity. An isosbestic point at this frequency exists in the differential X signal for the four binary mixtures, indicating that the system's response at this frequency is independent of the presence of trace gas. This is a key observation in this experimental study. The gold-coated fiber sensor modifies a few aspects of the microbridge design and can be used to resolve gas concentrations of ~100 ppm. However, this is achieved with a higher sensor power consumption, illustrating the fine balance between the sensitivity and power consumption.

For both sensor designs, the composition curve based on the phase lag is independent of the current amplitude and has the advantage of not requiring a current-dependent calibration for individual sensors. This could be useful as it demonstrates that these sensors system can be fabricated, integrated, and pre-programed to distinguish multi-gases without post calibration. Furthermore, since the amplitude and phase are independent signals and are sensitive to different thermophysical properties (k and C), it is possible to extend this approach to tertiary mixtures.

Finally, the temporal response of the sensor is limited by the integration time constant of the lock-in amplifier. The time constant of the lock-in is set to 300 ms for our experiments. To guarantee independent measurements, a wait time of 10 time-constants between measurements is chosen. With the use of a specialized lock-in circuit rather than a general laboratory lock-in amplifier, the response time could be reduced to approximately 15 ms.

CHAPTER 3. MODELING THERMAL CONDUCTIVITY IN POLYMERS

The thermal conductivity in amorphous and polymeric materials has been theoretically and experimentally[37-43] studied in good detail (especially for inorganic materials), but more accurate and predictive models (both empirical and first-principle models) are lacking. Such predictive models could provide useful information about the nature of vibrations and their contributions to thermal conductivity. In this chapter, an empirical model to predict temperature-dependent thermal conductivity of polymers is developed and is compared against experimental 3ω measurements.

3.1 Overview of Thermal Transport in Polymers

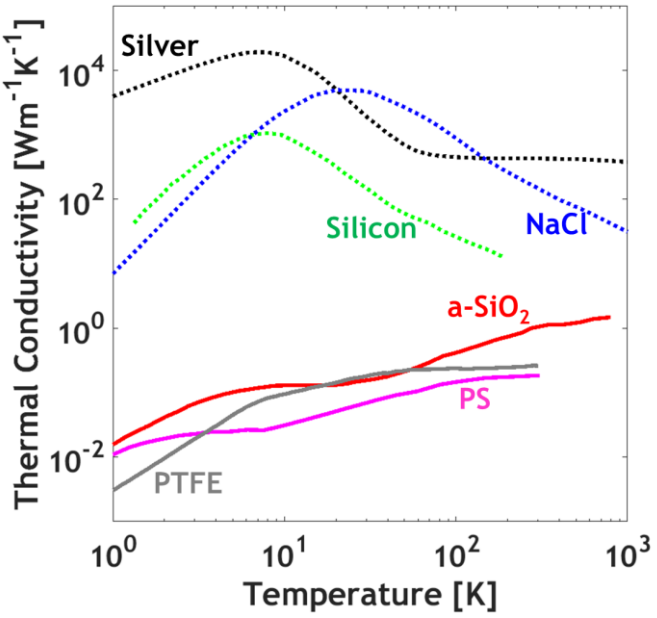

Figure 20 – Thermal conductivity overview of different types of solids – metals (silver), crystalline materials (silicon, NaCl), amorphous materials (a-SiO$_2$) and

polymers (PS, PTFE). Polymers and amorphous materials (—) show monotonically increasing TC with temperature, and undergo a plateau-like transition at intermediate temperatures (around ~10 K), which is different from the well-understood trends in metals and crystalline materials (…).

Figure 20 shows the measured thermal conductivity of different solids, including a crystalline metal (Ag), a crystalline ionic salt (NaCl), a crystalline semi-conductor (Si), an amorphous glass (a-SiO_2), and two common amorphous polymers (polystyrene, PS, and polytetrafluoroethylene, PTFE).[39,44,45] Crystalline and amorphous materials qualitatively exhibit different temperature dependent trends. Theories relying on the principles of phonon transport describe crystalline temperature dependent trends well.[39,46] The thermal conductivity of amorphous glasses and polymers monotonically increase with temperature, and undergo plateau-like transitions, that are not well described by phonon transport. The plateau-like transitions can be attributed to vibrational modes that behave differently from phonons.[47-49] Generally, these atomic vibrations are classified into propagating and non-propagating modes (discussed in further detail in Section 3.1.1); the propagating modes are the major carriers of heat at low temperatures (below the first plateau), whereas the non-propagating modes contribute at higher temperatures (above the first plateau).[47,48,50] Experimental data for temperature dependent thermal conductivity is available for several amorphous materials and disordered solids,[37,38,40,42,44] some of which are polymers. These measurements span temperatures ranging from ~1 K up to ~300 K. The experimental data for temperature dependent thermal conductivity for twelve polymers are shown in Figure 21.[40,41,44,45,51-53] A couple of models exist[37,38] that give an estimate of the thermal conductivity near room temperature, but they are less accurate over a wide range of temperatures, suggesting that these models may not capture the underlying physics describing the vibrational modes well. Atomistic and numerical simulations have yielded

more insight into thermal transport in amorphous materials,[54-58] but most of these studies considered a-Si and a-SiO_2 as model systems with very few simulations on polymers.[43,59,60]

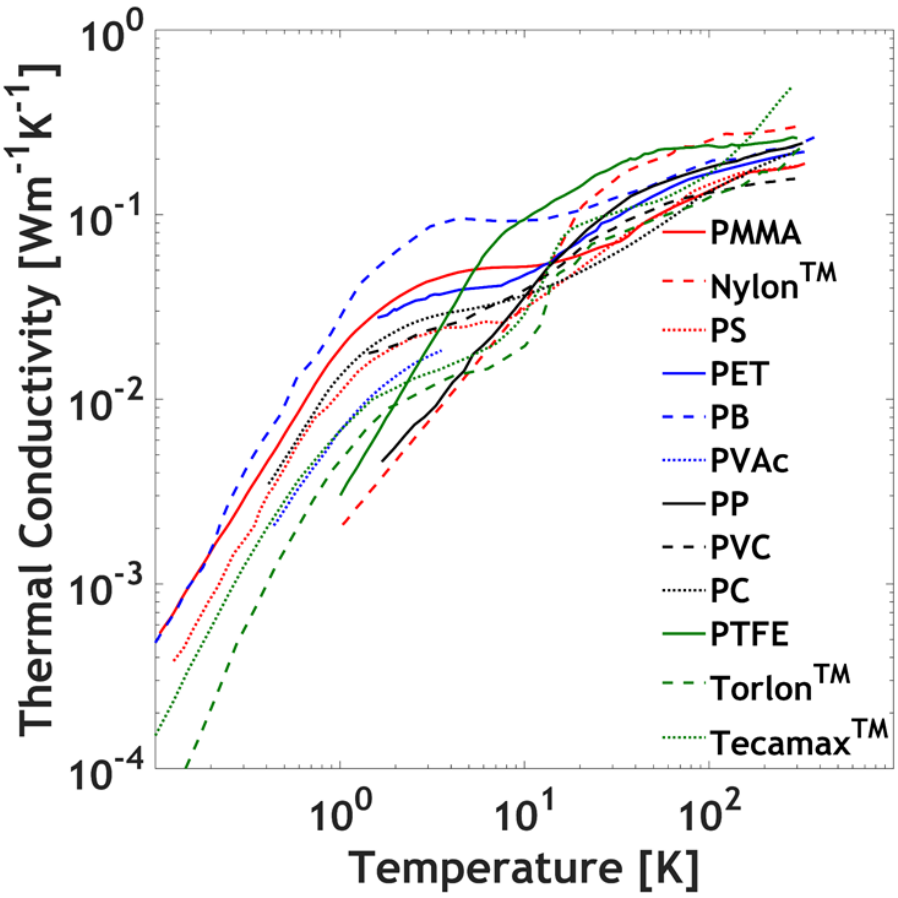

Figure 21 – Measured thermal conductivity of 12 different polymers as a function of temperature. It should be noted that most polymers approach a plateau at higher temperatures (~300 K), and go through a plateau-like transition at lower temperatures, owing to the different types of vibrational modes in amorphous systems

3.1.1 Vibrational modes in polymers

Atomic vibrations are responsible for thermal conduction in solids and are a primary contributing mechanism to thermal conductivity. In metals and other crystalline materials, the electrons and the lattice vibrations (*i.e.*, phonons) contribute to the thermal

transport. The electronic contribution to thermal conductivity is well described by the Wiedemann-Franz law[61] and the lattice contribution is well described by Boltzmann transport utilizing the phonon gas approximation for crystalline solids.[62] In polymers and some other amorphous materials, the free electron contribution is negligible, and a lattice is ill-defined with the lack of regular atomic order (*i.e.*, many polymers are not atomic crystals). Regular atomic order facilitates the definition of a vibration wave-vector and vibration frequency, which constitute a phonon. Without regular atomic order, the definition of a phonon becomes unclear in amorphous materials. Vibrational modes in amorphous materials can be classified into propagating and non-propagating modes.[50,55,56] The propagating modes are similar to phonons as they appear as collective vibrations with long wavelengths and some[50] consider them ballistic vibrations. These modes are termed propagons (P), whereas the non-propagating modes are further classified into diffusons (D) and locons (L). Locons are localized vibrations and diffusons refer to a diffusive like nature, where the vibrations are neither localized nor propagating. The P-D boundary is termed the Ioffe-Regel crossover and the D-L boundary is termed the mobility edge. Amorphous Si has been extensively (theoretically and experimentally) studied; Figure 22 shows the density of vibrational states[56,57] in a-Si with the appropriate P, D, and L domains adopted from Allen *et al*.[50]

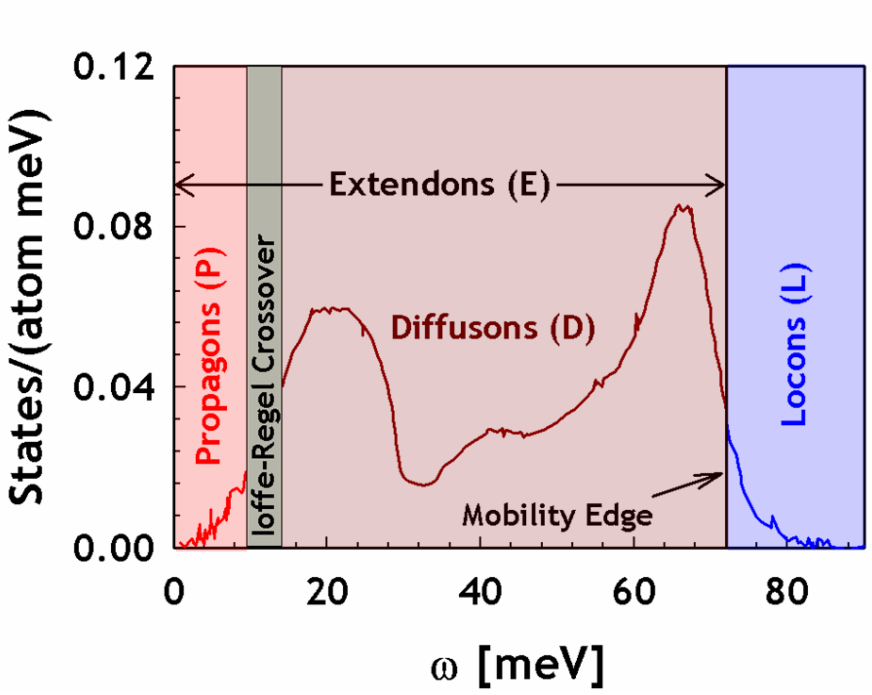

Figure 22 – Theoretically calculated vibrational density of states for a-Si. This is in close agreement to the experimental data

3.1.2 Previous thermal conductivity studies.

An early approach to modelling thermal conductivity that has been applied to amorphous materials is the Einstein model.[37,38] One approach to modeling thermal conductivity that has been applied to amorphous materials is the Einstein model. However, the Einstein model has not been widely adopted because of the ambiguity in choosing a single vibrational frequency and the poor agreement of this model with measured experimental values. An improvement to the Einstein model was suggested by Cahill and Pohl[38] based on the Debye model of vibrations and assuming the lifetime of each oscillator to be half its period of vibration. This is termed the minimum thermal conductivity or k-min model and is more widely adopted because of its relatively good agreement (within an order of magnitude) with room temperature experimental data. As an example, Figure 23

presents the Einstein and k-min predictions for polystyrene along with its measured experimental data.[44] The k-min model gives a good estimate for thermal conductivity at higher temperatures (typically > 50 K) but loses accuracy at lower temperatures. This example of the k-min and Einstein models under predicting the low temperature experimental thermal conductivity data applies to all polymers considered here.

Atomistic simulations are often required to fully understand the different vibrational modes and their contributions to thermal conductivity. Numerical calculations and molecular dynamics (MD) are used to calculate thermal conductivity in amorphous materials. From the standpoint of numerical simulations, determining the locations of the mobility edge and Ioffe-Regel crossover is useful in understanding the contribution of the different sets of modes. Distinguishing locons from propagons and diffusons is straightforward, based on inverse participation ratio calculations.[55,63] Differentiating propagons and diffusons is more challenging. Structure factor-based methods are well-established ways to distinguish propagons from diffusons. Recently, a more general method based on equilibrium atomic positions and vibrational eigenvectors has been developed.[64]

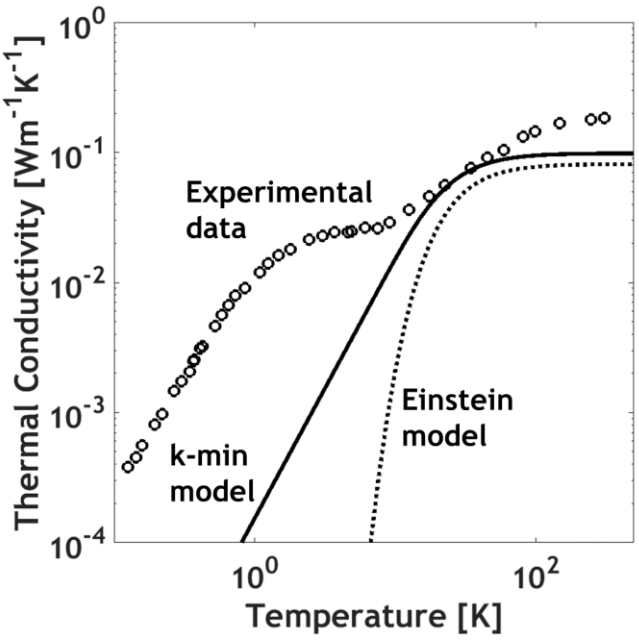

Figure 23 – Thermal conductivity data for polystyrene, along with the corresponding predictions from the Einstein and the k-min models. The k-min model predicts the thermal conductivity to a good degree of accuracy for T > 10 K.

Numerical simulations of thermal conductivity in amorphous materials involve calculations of modal properties such as specific heat, diffusivity, and density of states for propagons, diffusons, and locons. Classical expressions for density of states in solids are often used whereas both classical and quantum expressions for specific heat have been used. [55,58,65,66] Initial calculations of diffusivity were carried out by Allen and Feldman,[54] and are still used in numerical simulations.[43,58] For propagons, Allen and Feldman accounted for contributions to diffusivity from intrinsic resonant absorption and spectral relaxations,[55,67] which are significant at lower frequencies, in addition to expression used for diffusons. A different approach to modeling diffusivity of propagons is in terms of mode lifetime,[58] which is typically determined using normal mode analysis.[55,68,69]

More recently, a new formalism combining the Green-Kubo formulation with lattice dynamics has been developed to directly calculate the modal contributions to thermal conductivity.[70,71] MD simulations rely on knowing the interatomic potentials in materials for thermal conductivity calculations, which are not always readily available for a wide range of materials, especially polymers. Amorphous Si and SiO_2 have been extensively studied using numerical calculations but there has been less focus on amorphous polymers. More recently, thermal conductivity in polymers has been studied numerically.[43,59,60,70]

3.2 Empirical Thermal Conductivity Model

Kinetic theory[61,72] is used as the starting point to develop the empirical model and the thermal conductivity is defined as a function of the volumetric heat capacity, C [J/m^3-K], and the vibration diffusivity, D [m^2/s]. In terms of the phonon gas model, the vibrational diffusivity is defined as the product of the phonon mean-free-path and the phonon group velocity.

$$k = \frac{1}{3} CD \tag{21}$$

The specific heat and diffusivity are functions of the vibrational frequency and account for all the vibrational modes; Equation (21) is better expressed as an integral over the continuum of vibrational frequencies.

$$k = \frac{1}{3} \int C(\omega) D(\omega) N(\omega) d\omega \tag{22}$$

where $N(\omega)$ (in [#-s]) is the density of states, which is the number of vibrational modes in the frequency range between ω and $\omega+d\omega$. To account for the different types of vibrations in polymers introduced earlier, the integral in Equation (22) is split into three parts: one part each for propagons (P), diffusons (D), and locons (L). The integral for each type of vibration is carried out between its corresponding frequency limits between: (i) ω=0 rad·s^{-1} and the Ioffe-Regel cross-over (ω_P) are for propagons, (ii) the Ioffe-Regel crossover and mobility edge (ω_D) are for diffusons, and (iii) the mobility edge and infinity are for locons. Hence the Ioffe-Regel crossover and the mobility edge give cutoff frequencies for the propagons and diffusons, respectively. While the Ioffe-Regel crossover is usually spread over a range of frequencies,[50] a sharp cutoff between propagons and diffusons is utilized for convenience in this model. Furthermore, the cutoff frequency can also be expressed as an equivalent cutoff temperature, according to the relation $\hbar\omega_i = k_B T$ (i=P,D,L), naturally lending itself to the existence of plateaus in the temperature dependent thermal conductivity; therefore, the concept of a cutoff frequency and cutoff temperature are used interchangeably in this chapter. A dimensionless cutoff $x_i = \hbar\omega_i / k_B T = T_i / T$ is used as a convenient change of variables.

$$k = k_P + k_D + k_L = \frac{1}{3} \sum_{i=P,D,L} \int_{\omega_{i-1}}^{\omega_i} C_i(\omega) D_i(\omega) N_i(\omega) d\omega \tag{23}$$

3.2.1 Properties of vibrational modes

The volumetric specific heat is obtained by treating each vibrational mode as an independent 1D oscillator and summing over all three spatial directions, and the final expression is given by Equation (24).[61] This expression models the specific heat suitably

well for propagons as they are closest to phonon-like vibrations. The same expression is used for non-propagating modes as well since thermal conductivity simulations based on this assumption are in reasonable agreement with experimental values.[58]

$$C = 3nk_B \frac{x^2 e^x}{\left(e^x - 1\right)^2}, x = \frac{\hbar\omega}{k_B T} \tag{24}$$

The vibrational diffusivity is proportional to the vibration propagating speed (v_s, in m/s), which is taken to be the speed of sound averaged over transverse (v_T) and longitudinal (v_L) modes, and the frequency of the vibrational mode.[58] The expression given by Equation (25) is used to model diffusivity. While this expression is mainly used for propagating modes, this expression for vibrational diffusivity is favored over the more complicated Allen and Feldman diffusivity[54] and find it describes diffusons and locons reasonably well. The subscript *i* in Equation (25) refers to the type of vibrational mode (P, D, or L). MD and numerical simulations are often required to determine the exact value of exponent β_i and it is presently left as a fitting parameter in the empirical model.

$$D_i(\omega) \propto v_s^2 \omega^{-\beta_i} \tag{25}$$

The 3-dimensional density of states expression under the Debye approximation,[61] given by Equation (26), is used in the empirical model.

$$N(\omega) = \frac{3\forall\omega^2}{2\pi^2 v_s^3} \tag{26}$$

Here, $\forall$ [in m^3] is the volume of a unit cell. Unlike crystalline materials, defining a unit cell in a polymer is non-trivial. However, it can be said that the volume of a unit cell is

inversely proportional to the number density (n, in [#-m^{-3}]). Therefore, the density of states can be proportionally written as

$$N(\omega) \propto \frac{3\omega^2}{2n\pi^2 v_s^{\,3}} \tag{27}$$

Table 5 lists the fundamental material properties used in defining the above modal properties of the twelve polymers shown in Figure 21, which are used in developing the empirical model. The number density is defined as the number of monomer units per unit volume (i.e., $n = \rho N_A/M$, where N_A is the Avogadro constant, ρ is the gravimetric density, and M is the monomer molecular weight). Substituting Equations (24), (25), and (26) into Equation (23) yields a temperature dependent expression for the thermal conductivity given in Equation (28). The proportionality can be expressed as an equality by introducing a proportionality constant, f_i, that is dependent on the type of vibrational mode. Equation (28) has eight unknowns: (i) three proportionality constants, f_i, (ii) two dimensional cutoffs (Ioffe-Regel crossover and mobility edge), and (iii) three exponents β_i for each of the three types of vibrational modes.

$$k(T) = \frac{k_B}{v_s} \sum_{i=P,D,L} f_i \left(\frac{k_B T}{\hbar}\right)^{3-\beta_i} \int_{x_{i-1}}^{x_i} \frac{x^{4-\beta_i} e^x}{\left(e^x - 1\right)^2} dx \tag{28}$$

Table 5 – Fundamental properties of polymers used in this study. The numbers next to the polymer indicate the references used for thermal conductivity data.

Sl. No	Polymer	v_s [m/s]	ρ [kg/m^3]	M [g/mol]	n [m^{-3}], $\times 10^{27}$
1	Polymethylmethacrylate (PMMA)[40]	1730	1170	100	6.93
2	Polyhexamethylene-adipamide (Nylon^{TM})[51]	1845	1140	113	6.08
3	Polystyrene (PS)[44]	1775	1050	104	6.08
4	Polyethyleneterephthalate (PET)[40]	1275	1337	192	4.19
5	Polybutylene (PB)[44]	1690	930	54	10.4
6	Polypropylene (PP)[41]	1975	946	42	1.36
7	Polyvinylchloride (PVC)[41]	1782	1330	62.5	12.8
8	Polycarbonate (PC)[40]	1564	1210	254	2.87
9	Polytetrafluoroethylene (PTFE)	1070	2100	100	1.26
10	Polyvinylacetate (PVAc)[40]	1500	1190	64	11.2
11	Polyamide-imide (Torlon 4203^{TM})[52]	2200[73,74]	1411	64	3.73
12	Polyparaphenylene (Tecamax^{TM})[53]	1432[75]	1210	228	9.59

3.2.2 Results of initial model fitting

The empirical model, described by Equation (28) is fit to the temperature dependent thermal conductivity for twelve polymers (polymers 1-12 in Table 1) found in literature and the values of the eight unknowns are determined for each polymer. For these fits, a coefficient of determination, $R^2 > 0.95$ is obtained, which is not unexpected given the

number of fitting parameters. Based on the findings of the initial fitting routine, a few modifications have been made to the empirical model.

As illustrated in Figure 21, the *k*-*T* curves of most polymers go through a first plateau or a region of reduced slope, around 10 K suggesting transition between propagons and diffusons in polymers. However, a similar transition between diffusons and locons is difficult to observe as most polymers undergo glass transition (or degradation) modestly beyond room temperature. Thus, the f_L values for locons is negligibly small. This has recently been confirmed with MD simulations of a-Si and a-SiO_2, which revealed that propagons and diffusons are the major carriers of heat in amorphous materials and the contribution of locons is usually small.[70,71] Therefore, the model can be simplified by only considering two modes – propagons and diffusons – reducing the number of unknown fitting parameters to six.

The values of the exponents β_P and β_D are shown in quartile representation in Figure 24. For all the polymers considered, β_D is found to be very close to 1. All polymers have β_D between 0.95 and 1.05. For all polymers, a constant value of $\beta_D = 1$ results in a good prediction of the temperature depend thermal conductivity (with $R^2>0.95$), with other parameters left unchanged. Therefore, a constant value of $\beta_D = 1$ is used in the model. β_P has more variation than β_D with ~70% of the polymers considered here falling within than range $1.1 \leq \beta_P \leq 1.3$. To simplify the model further, a constant value of 1.2 for β_P is considered. This value of β_P results in a good prediction of thermal conductivity (with $R^2>0.90$), with all other parameters left unchanged. A value of $\beta_P = 1.2$ results in a $T^{1.8}$ dependence for *k* at low temperatures (<1 K). This temperature dependence is verified for the twelve polymers considered in this study.

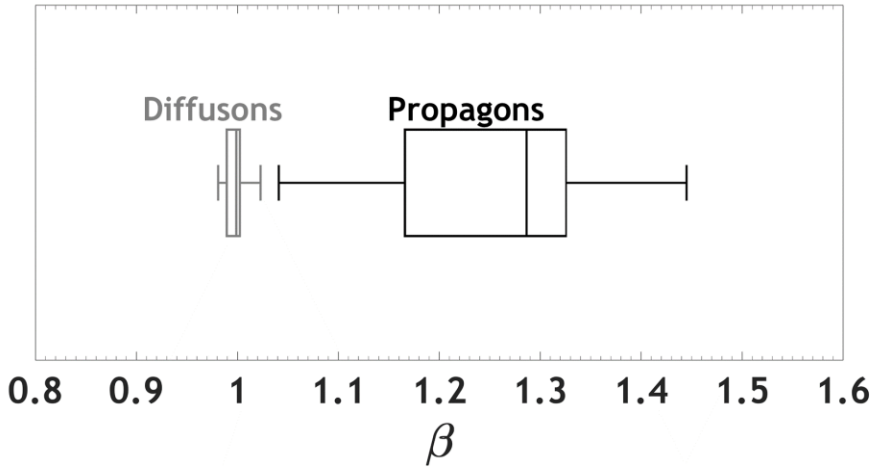

Figure 24 – Quartile graphs indicating the variation in the exponents β_P and β_D determined by curve fitting the measured data to the initial model.

3.3 Temperature-Dependent Thermal Conductivity Model

Based on the observations of the previous fitting routine, Equation (28) can be simplified to Equation (29) to only considers contributions from propagons and diffusons.[76] The first term on the right-hand side of Equation (29) is the contribution from propagons and the second term is the contribution from diffusons. This model has only four fitting parameters – the coefficients f_P and f_D, and the dimensionless cutoffs x_P and x_D for propagons and diffusons, respectively. As before, a fitting routine is performed for the twelve polymers.

$$k(T) = f_P \frac{k_B}{v_s}\left(\frac{k_B T}{\hbar}\right)^{1.8} \int_0^{x_P} \frac{x^{2.8} e^x}{\left(e^x - 1\right)^2} dx + f_D \frac{k_B}{v_s}\left(\frac{k_B T}{\hbar}\right)^{2} \int_{x_P}^{x_D} \frac{x^3 e^x}{\left(e^x - 1\right)^2} dx \qquad (29)$$

3.3.1 Relation between model parameters

The results of the fitting routine to the modified model suggest an inverse power-law relationship between f_P and T_P, and f_D and T_D. A similar relationship is also observed between the coefficients f_P and f_D. Figure 25 shows the relationship between the fitting parameters, the best-fit equations, and the coefficient of determination (R^2) for the inverse-power law fits; Equations (30) summarize these best-fit equations.

$$T_P = 53.94\, f_P^{-0.278};\ T_D = 72.27\, f_D^{-0.283};\ f_D = 25.09\, f_P^{-0.768} \tag{30}$$

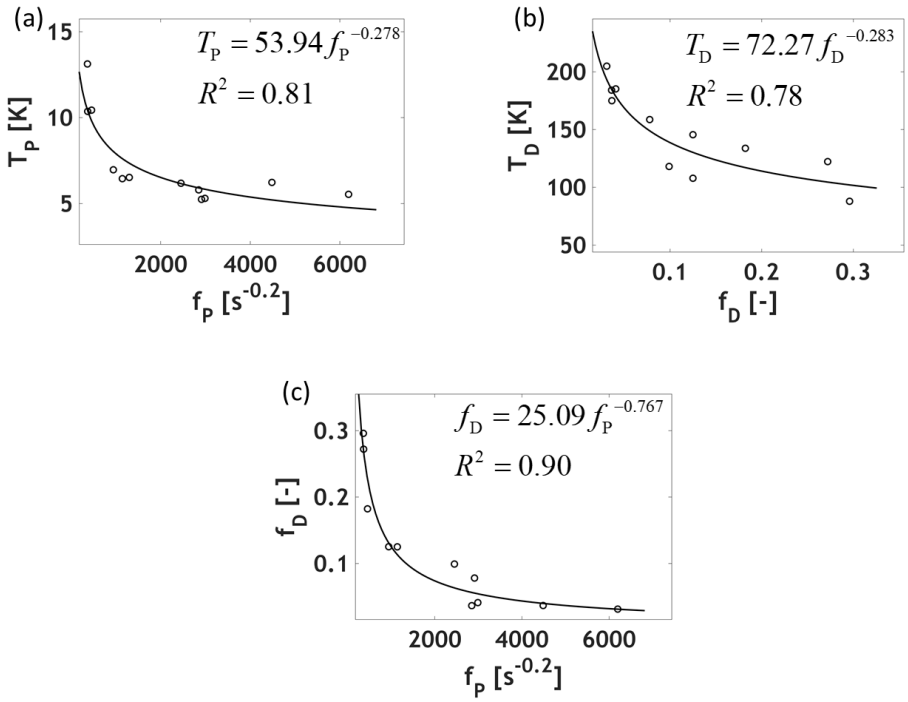

Figure 25 – The four fitting parameters plotted against one another and fitted to an inverse power law curve with their coefficient of determination (R^2).

For the empirical model to be complete, it is necessary to relate one of the four model parameters to fundamental properties like ρ, M, and v_s. For crystalline materials, a Debye temperature can be defined using Equation (31),[61] which is the highest temperature

achieved from a single normal vibration. This definition is extended to polymers, where the monomer molecular weight for M and the average speed of sound for v_s are used. With this modified definition of a Debye temperature, the diffuson cutoff temperature, T_D, can be related to T_{Deb} (in [K]) and ρ (in [kg·m^{-3}]) using an inverse power law-fit given in Equation (32).

$$T_{\mathrm{Deb}} = v_s \frac{\hbar}{k_B}\left(6\pi^2 n\right)^{1/3} \tag{31}$$

$$T_D = 1.465\times10^7 \left(\rho\sqrt{T_{\mathrm{Deb}}}\right)^{-1.23} \tag{32}$$

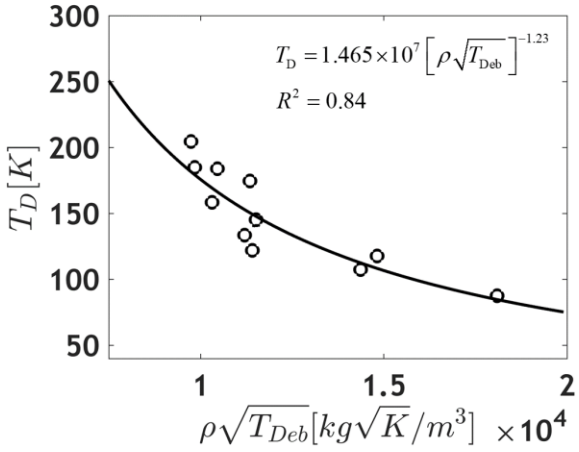

Figure 26 – The diffuson cut-off temperature (T_d) plotted as a function of density (in kg/m^3) and Debye temperature (in [K]), and the inverse power law fit.

3.3.2 Interpreting model parameters

The propagon cut-off frequency, ω_P, represents the Ioffe-Regel crossover, which is the cutoff between propagons and diffusons. The empirical model estimates this frequency to be between 0.6 and 1.7 THz. Previous studies[50,58,72] have shown that this crossover occurs at a frequency when the mean-free-path (Λ) is approximately 10x the interatomic

distances (a). It is possible to determine the order of magnitude of the ratio Λ/a for the polymers considered in this study based on the propagon cutoff frequency, speed of sound, and number density (Equation (33)). The empirical model estimates this ratio to be ~10.

$$\frac{\Lambda}{a} \approx \frac{2\pi v_s n^{1/3}}{\omega_P} \tag{33}$$

The propagon and diffuson contributions to thermal conductivity in equation (29) can be rewritten as equation (34) using the *f*-*T* relations in equation (30). The terms in the brackets converge to a maximum value of 0.56 and 0.5 for propagons and diffusons, respectively. This implies that k_P and k_D appear to have empirical upper limits, which are functions of the model parameters f_P and f_D, and this upper limit is given by equation (35). Thermal conductivity of most polymers change by <5% beyond 300 K, and the upper limit can be used to predict room temperature thermal conductivity of polymers. This limit is compared with the experimental thermal conductivity at 300 K for a range of polymers and is shown in Figure 27. The upper limit of the k-min model, given by equation (36),[39] which is also commonly used for predicting room temperature thermal conductivity is also shown in the figure.

$$k_P(T) = 1.85 \frac{f_P^{0.5}}{v_s}\left[\frac{1}{x_P^{1.8}}\int_0^{x_P}\frac{x^{2.8}e^x}{\left(e^x-1\right)^2}dx\right];\ k_D(T) = 1226\frac{f_D^{0.43}}{v_s}\left[\frac{1}{x_D^{2}}\int_{x_P}^{x_D}\frac{x^{3}e^x}{\left(e^x-1\right)^2}dx\right] \tag{34}$$

$$k_{max} = \frac{1}{v_s}\left(f_P^{0.5} + 613 f_D^{0.43}\right) \tag{35}$$

$$k_{min,high\ T} \approx 0.4 k_B n^{2/3}\left(v_L + 2v_T\right) \tag{36}$$

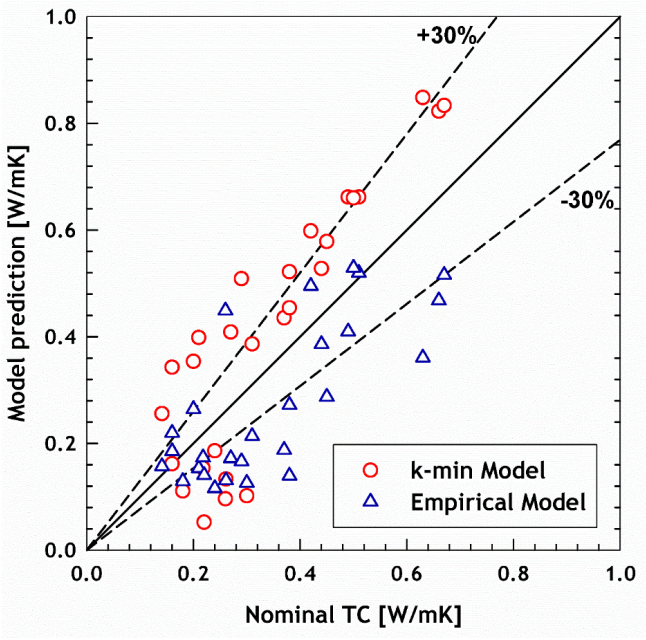

Figure 27 – Comparison of experimental thermal conductivity of polymers and polymer blends at room temperature with k-min and empirical models

This could be a useful observation as it suggests a limit on the total thermal conductivity of bulk amorphous polymer materials. While there are studies suggesting divergent thermal conductivity of single polymer chains[77,78] or high thermal conductivity in drawn/aligned/crystalline polymer fibers,[79-81] the empirical model suggests there is an upper thermal conductivity limit for bulk amorphous polymers. The empirical model could also help in providing insights into tuning material properties to get desired temperature-dependent thermal conductivity.

3.3.3 Comparison with 3-omega measurements

The temperature-dependent thermal conductivity predicted by the empirical model is compared against experimental 3-omega measurements on five amorphous polymers – PMMA, PS, PTFE, PVC, and polyvinyl alcohol (PVA) between 10 K and 300 K.

Measurements on PTFE are performed on a 1 mm thick substrate using the slope method, whereas measurements on the other polymers are performed on ~1 μm thick spun-coat/drop-cast films on a Si substrate with ≈90 nm thick thermal oxide layer. The sample is placed in a closed loop Helium cryostat, which allowed for precise temperature control. Figure 28 shows the 3-omega measurements and literature data for T < 10 K, along with the predictions of the empirical model. The model is found to have a coefficient of determination (R^2) consistently greater than 0.75.[76]

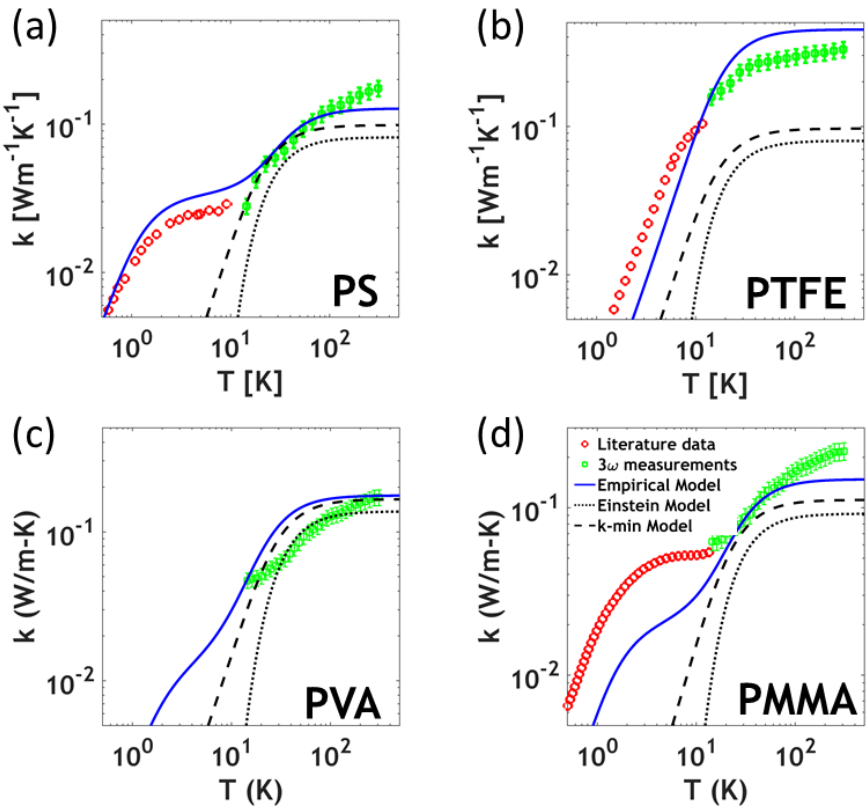

Figure 28 – Literature values of experimental thermal conductivity (red hollow circles), our 3ω measurements (green squares with error bars) and the empirical model predictions (solid blue line) for four polymers.

3.4 Summary

An empirical model to aid in the prediction of temperature-dependent thermal conductivity of polymers is developed in this chapter. The model is based on the kinetic theory and is appropriately modified to account for the different vibrational modes in polymers, namely propagons, diffusons, and locons. The model is fully qualified by relating the empirical parameters to fundamental material properties – density, monomer molecular weight, and speed of sound. The final model is only dependent on three material properties, all of which are relatively straightforward to measure or determine. The empirical model provides useful insights into the location of the Ioffe-Regel crossover and an upper limit, which can be useful to predict room temperature thermal conductivity.

CHAPTER 4. ANISOTROPIC THERMAL CONDUCTIVITY MEASUREMENTS IN POLYMERS

Anisotropic thermal conductivity can complicate the performance of semiconducting polymer thin-films in applications such as thermoelectrics and photovoltaics.[82,83] Previous measurements have indicated the presence of thermal anisotropies in thermoelectric polymers, with thermal conductivity ratios (in-plane to through-plane) as high as 2.[84-86] Anisotropic measurements of low thermal conductivity polymers are challenging and there are a limited number of appropriate measurement techniques. Suspended film 3ω is an appropriate technique but has often required unfavorable microfabrication. This chapter discusses on the utility of the suspended 3-omega technique that uses shadow masking, and no other microfabrication techniques, in performing anisotropic (in-plane, ∥ and through-plane, ⊥) thermal conductivity measurements of polymer films. In this chapter, the anisotropy is defined as the ratio of in-plane and through plane thermal conductivities ($k_{\parallel}/k_{\perp}$).

4.1 Overview of anisotropy measurements

Traditional thermal metrology techniques such as 3ω, TDTR, and FDTR are well-established for accurately measuring thermal conductivity but have primary utility in measuring isotropic films in the through-plane direction. Both the thermoreflectance techniques have been appropriately modified to characterize anisotropy (directional thermal conductivity),[87-89] but these modifications dominantly involve either using more complex thermal models for standard measurement data resulting in large uncertainties or

offsetting the heating and sensing processes along the direction of interest. Unfortunately, these modifications cannot often be extended to polymer films due to their low intrinsic thermal conductivity. The 3ω technique has good sensitivity to low thermal conductivity materials and is well-suited for anisotropy characterization.

There have been a few modifications to traditional 3ω technique to characterize anisotropy. These modifications involve sample-heater configurations, such as a (i) film on a substrate with heater widths comparable to film thickness,[13,15,90] (ii) heat spreader method,[91,92] (iii) suspended film with heater lines,[90,93] and (iv) electrically conductive suspended films in a self-heating configuration.[94,95] Configuration (i) requires complex microfabrication techniques to fabricate heater lines with widths comparable to film thicknesses (~ 1 μm). Photoresist and solvents commonly used in microfabrication processes can often have detrimental effects on polymer films. Furthermore, this technique involves fitting experimental data to the multilayer model and can often result in large measurement uncertainties.

4.2 Suspended film 3ω technique

Figure 29 shows the configuration of the suspended film and the metal heater line that are considered in the suspended film 3ω technique.[96] The multilayer solution, given in equation (10) can be simplified for a single layer of thickness *d* with adiabatic boundary condition at the bottom to give equation (37). This is the general solution for a suspended film and the in-plane thermal conductivity can be obtained by fitting the data to this equation.

$$\Delta T_{\text{susp film}} = \frac{p_0}{\pi L k_\perp} \int_0^\infty \frac{1}{B \tanh(Bd)} \left(\frac{\sin(b\zeta)}{(b\zeta)} \right)^2 d\zeta, \text{ where } B = \sqrt{\frac{k_\parallel}{k_\perp} \zeta^2 + j \frac{2\omega C}{k_\perp}} \quad (37)$$

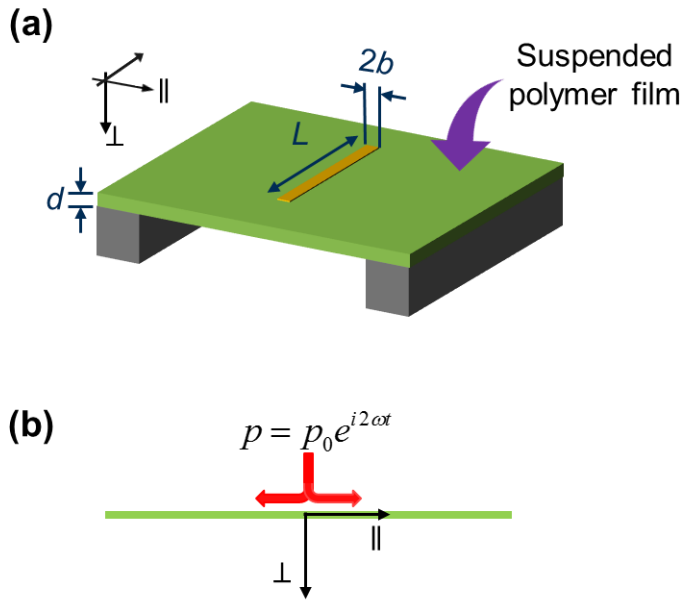

Figure 29 – Configuration of the suspended film and metal heater-line for in-plane measurements and (b) the heat flow configuration used in the 1D analysis. The in-plane and through-plane directions are shown.

However, under the assumptions of negligible film thickness (*i.e.*, $d << L_{p,\perp}$), and negligible heater width (*i.e.*, $b << L_{p,\parallel}$), the heat conduction can be modeled as one-dimensional and the solution is given by equation (38).[93]

$$\Delta T_{1D} = \frac{P_0}{2dL\sqrt{2\omega C k_\parallel}} e^{-j\pi/4} \quad (38)$$

4.2.1 Limits of the 1D model

The 1D approximation given by equation (38) requires an (effectively) infinitely long and narrow heater line, and negligible heat flow in the ⊥-direction (i.e., a thin film).

The numerical criteria for the validity of infinite heater length is given by equation (11). This criterion sets the limit on the minimum frequency in a suspended film technique. The thin-film and narrow heater approximations require the film thickness and heater line half-width to be significantly smaller than the penetration depths of the thermal wave in the ⊥- and ∥-direction, respectively, (*i.e.*, $b/L_{p,\parallel} \ll 1$ and $d/L_{p,\perp} \ll 1$). The 1D model is applicable if its error relative to the general solution (equation (37)) and the experimental uncertainty are low. To determine the precise limits of the aforementioned inequality criterion, the 1D model is compared to the general solution for different values of $b/L_{p,\parallel}$ and $d/L_{p,\perp}$ using two dimensionless parameters – (i) mean absolute error (e), which is a measure of the error between the 1D model and the general solution, and (ii) sensitivity to in-plane thermal conductivity ($S_\parallel$), which is an indirect measure of the of measurement uncertainty. Equation (39) defines e, which is the error between the 1D model and general solution, averaged over all frequencies used during a 3ω measurement. For the 1D approximation to yield an accurate estimate of thermal conductivity, a low value of e and a high value of $S_\parallel$ is desired. To account for both parameters, a factor η is defined using equation (40), which can be used as a metric to determine the validity of the 1D model. η ranges between 0 and 1 since e ranges between 0 and 1 and $S_\parallel$ ranges between 0 and 0.5. Higher values of η correspond to a better validity of the 1D approximation and a lower uncertainty in the measured valued. The value of η can be calculated for different values of $d/L_{p,\perp}$ and $b/L_{p,\parallel}$ and the experimental frequency range chosen in this study is $0.1 < f < 1$ Hz, although the results hold true for any logarithmic decade of frequencies.

$$e = \frac{1}{N}\sum_{i=1}^{N}\left(1-\frac{\Delta T_{1\mathrm{D},i}}{\Delta T_{\text{susp film},i}}\right)^2, i = \omega_1, \omega_2, \ldots, \omega_N \tag{39}$$

$$\eta = 2(1-e)S_{\parallel} \tag{40}$$

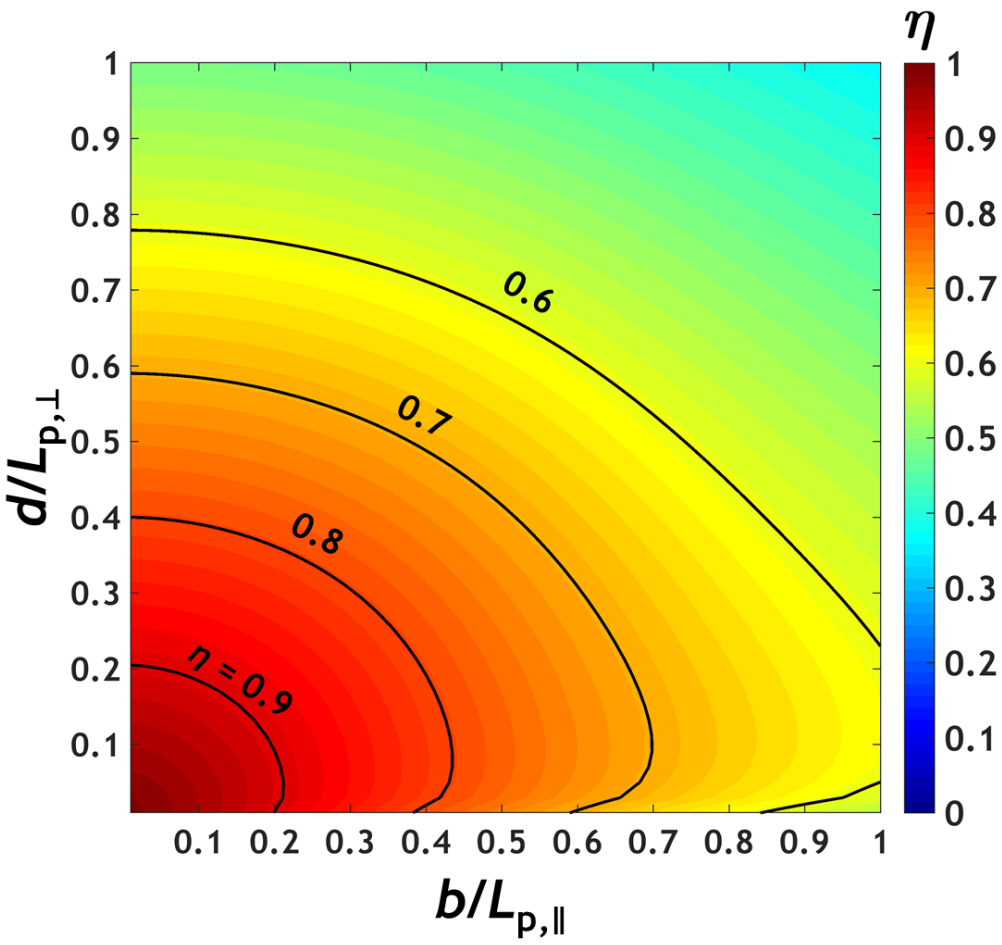

Figure 30 – Contour plot of η as a function of the dimensionless variables, $d/L_{p,\perp}$ and $b/L_{p,\parallel}$. Iso-η lines provide guidelines for the validity of the 1D approximation.

Figure 30 provides a contour plot of η for different values of $d/L_{p,\perp}$ and $b/L_{p,\parallel}$. Here, $L_{p,\perp}$ and $L_{p,\parallel}$ are calculated at the maximum frequency (f =1 Hz) since it represents the limiting case as lower frequencies for a given values of d and b result in higher values of η. For η > 0.9, the measured thermal conductivity extracted from the 1D model fitting is within 5% of the actual value, and for η > 0.8, the predicted value is within 10% of the actual value. This is verified for using robust Monte Carlo uncertainty approaches.

Measurement uncertainty increases as η further decreases, and prediction errors larger than 25% can be common for $\eta < 0.7$. The criteria mentioned in equation (11), coupled with the $\eta > 0.9$ criterion provides the measurement conditions for the applicability of the suspended 3ω technique with errors consistently under 5%.

4.2.2 Validation experiments

The contour plot shown in Figure 30 provides criteria for using the suspended 3ω technique for measuring anisotropic polymer films. These criteria are verified on three materials: (i) PVDF, an isotropic polymer, (ii) muscovite mica, a naturally occurring mineral with a high degree of anisotropy, and (iii) PEDOT:PSS, a thermoelectric polymer with a reported anisotropy of ~2. PVDF pellets (MW ~ 180,000) are obtained from Sigma-Aldrich, PEDOT:PSS (Clevios PH1000) is obtained from Heraeus, and muscovite mica discs are obtained from Axim Enterprises Inc. The specific heat capacities of PVDF, and mica are measured to be 1.32, and 0.645 J/g-K, respectively, using a differential scanning calorimeter (TA Instruments, Q100 DSC). Density of PVDF is taken from the MSDS provided by the manufacturer at a value of 1.78 g/cc. The density of mica is measured to be 2.96 ± 0.15 g/cc using water-displacement method. The volumetric heat capacity of PEDOT:PSS is obtained from literature.[85] Thin films of PVDF (d = 2.8 μm) and PEDOT:PSS (d = 9.4 μm) are obtained by peeling-off a drop-cast film from a Si substrate and thin-films of mica (d = 41.3 μm) are obtained by manual exfoliating. These films are suspended between Si substrates that acted as heat sinks, and a gold heater lines of width $2b$ = 20 μm and length L = 4.5 mm are deposited using electron-beam evaporation through a shadow mask. 3ω experiments are performed in a frequency range such that the conditions from the previous section are satisfied. The experiments are performed under

vacuum (pressure < 10^{-5} torr) to prevent conduction through air. By fitting the 3ω data to the 1D model, in-plane thermal conductivities of PVDF, PEDOT:PSS, and mica are determined to be 0.21 ± 0.02, 0.52 ± 0.08, and 4.26 ± 0.41, respectively, and all measurements are within 10% of the values previously reported in literature.[85,97,98] The uncertainty in our measurement is calculated using standard error propagation analysis on equation (38). Figure 31(a) shows the experimental 2ω temperature amplitude (normalized by input power) vs. frequency for PVDF, mica, and PEDOT:PSS, along with the 1D fits. The independence on the heater width is also verified on mica using three different linewidths, and this is shown in Figure 31(b).

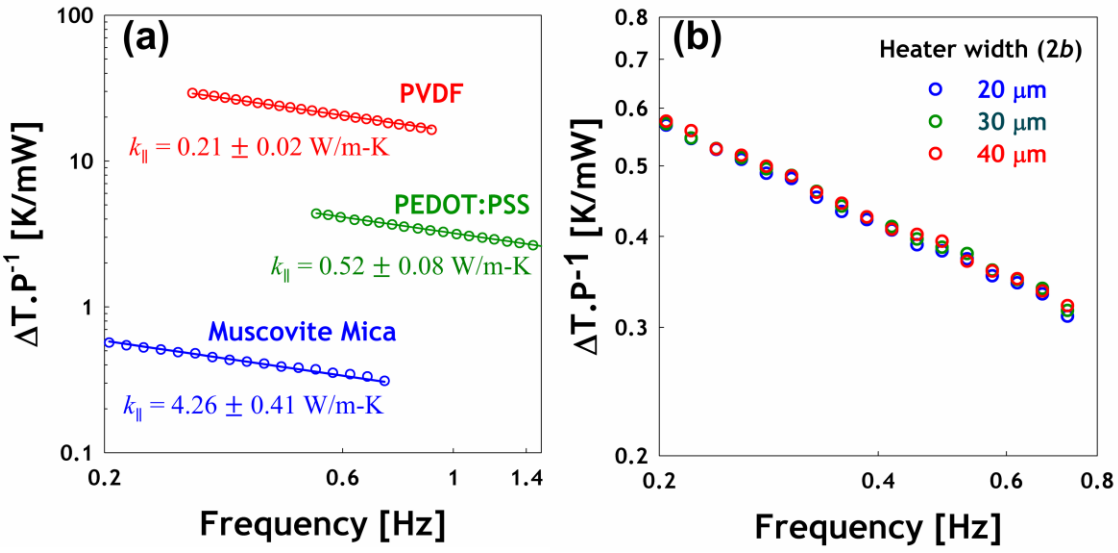

Figure 31 – (a) Experimental temperature amplitudes normalized by the input electrical power (circles) of suspended mica and PVDF, along with the 1D model fit (solid lines). Frequency ranges for fits are chosen to satisfy the criteria for 1D model. (b) Experimental normalized temperature amplitudes of suspended mica for three different heater widths, 2*b*; independence of the measurement on *b* supports validity of the 1D model.

4.3 Anisotropic measurement on polymers

4.3.1 Semiconducting polymers – N2200 and P3HT

Using the suspended 3ω technique described in the previous section, two common semiconducting polymers – N2200 (or P(NDI2OD-T2)), a commercially available n-type semiconducting polymer, and P3HT (MW ~ 10532 Da), a common p-type semiconducting polymer synthesized by Grignard Metathesis method – are thermally characterized. To measure $k_{\parallel}$ with the suspended film technique, information on volumetric heat capacity (i.e., density and specific heat) are required. The density of P3HT is determined using water displacement method, while the density of N2200 is indirectly calculated from speed of sound (using picosecond acoustics) and elastic modulus (using nanoindentation) measurements. This approach is adopted due to the limited quantity of material available (< 100 mg). Specific heat capacities of P3HT and N2200 are measured using differential scanning calorimetry. Measurements are performed in the temperature range of 25-50 ^{o}C (ramp rate: 5 ^{o}C/min) using 2.4 mg and 8.2 mg of N2200 and P3HT, respectively. Specific heat at 30 ^{o}C is used for the purposes of data analysis. The specific heat of N2200 and P3HT is measured to be 1.35 and 1.53 J/g-K, respectively. The results of DSC measurements are shown in Figure 32.

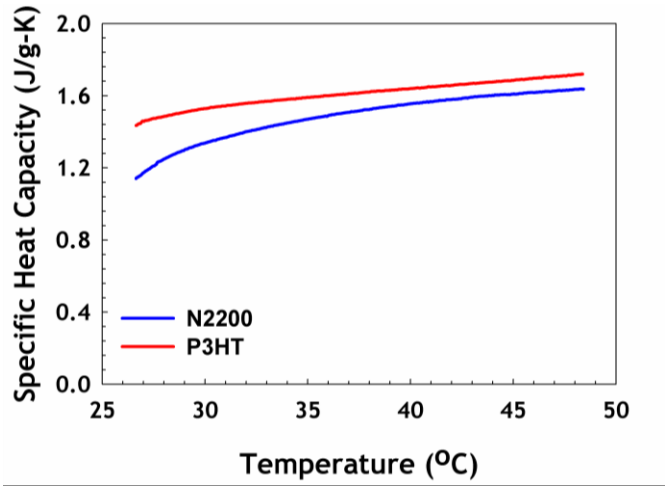

Figure 32 – Specific heat capacity measurements on N200 and P3HT performed using DSC. Values at 30 °C are used for data analysis.

To obtain suspended films for in-plane measurement, P3HT and N2200 are drop-cast on a silicon substrate to obtain films of thicknesses 35 ± 1.5 and 32 ± 2 μm, respectively. The films are peeled off using water flotation technique, which involves immersing the film-on-substrate in DI water until the film peeled off the substrate (typically within 60 seconds). The films are heated in a vacuum oven at 100 °C to remove residual water from the films. Gold heater lines of L = 4.5 mm and $2b$ = 20 μm are deposited on the film, and frequencies are chosen to satisfy $\eta > 0.8$. The film is suspended between two Si substrates, and experiments are performed at high vacuum levels (< 10^{-5} torr). The results of the 3ω measurements on the suspended film are fit to the 1D model, and the in-plane plane thermal conductivity of P3HT and N2200 are determined to be 0.35 ± 0.03 and 0.27 ± 0.02, respectively. Figure 33 shows the experimental data and the 1D model fits for the suspended films.

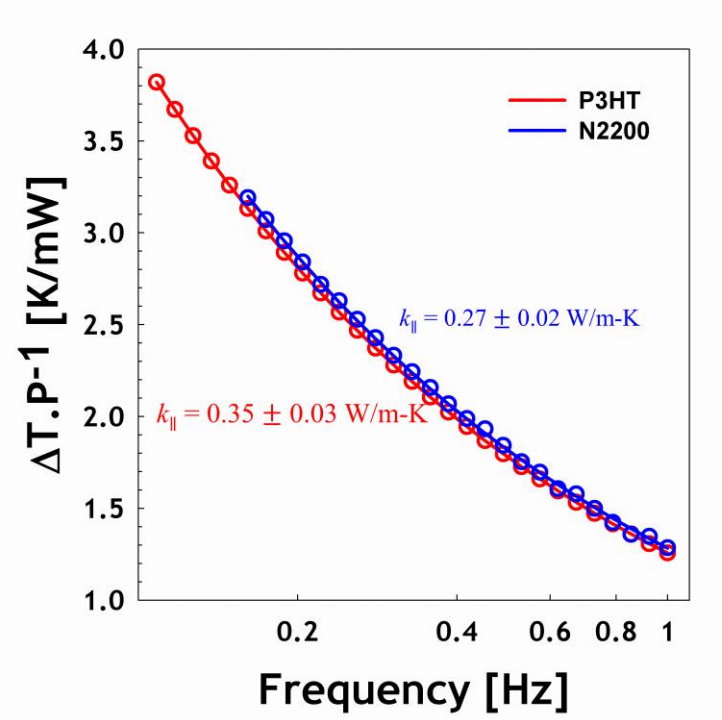

Figure 33 – Experimental normalized 2ω temperature amplitude for suspended P3HT and N2200 (open circles), along with the corresponding 1D model fits (solid lines).

In addition to in-plane thermal conductivities, the through-plane values are also measured using the differential 3ω method. Thin-films of P3HT (≈300 nm) and N2200 (≈345 nm) are spun-coat from 30 mg/mL solutions in chlorobenzene at 1000 rpm for 60 s on a silicon substrate with a 100 nm oxide layer. Prior to spin-coating, the substrates are sonicated for 3 minutes in DI water, acetone, and isopropanol, in that order, and exposed to oxygen plasma for 5 minutes. The through-plane thermal conductivities of P3HT and N2200 are measured to be 0.27 ± 0.02 and 0.16 ± 0.01 W/m-K, respectively. These values are smaller than the in-plane conductivities, resulting in anisotropies of 1.3 and 1.7, for P3HT and N2200, respectively.

The measured thermal conductivities of P3HT and N2200 are compared with the predictions of two models – the Cahill-Pohl k-min model and the empirical model described in Chapter 3. The upper limits of the two models, given by equations (35) and (36), are used for comparison; the inputs to both models are number density, gravimetric density, and speed of sound. The number density is obtained from the measured volumetric heat capacity using the Dulong-Petit limit, $C=3nk_B$, where k_B is the Boltzmann constant. Longitudinal speed of sound in N2200 is calculated from picosecond time-resolved acoustic measurements using a traditional TDTR set-up. A thin-film of N2200 (thickness, $d \approx 50$ nm) is spun-coat on a sapphire substrate. An aluminum transducer layer of thickness $d_{Al} \approx 320$ nm is deposited on the polymer layer. Figure 34 shows the results of thermoreflectance measurements on N2200. The acoustic echoes from the Al/polymer interface (delay time, t_1) and polymer/substrate interface (delay time, t_2) can be observed, and the longitudinal speed of sound ($v_{s,L}$) is estimated to be 1860 m/s using equation (41). The transverse speed of sound ($v_{s,T}$) is assumed to be half the longitudinal value (equivalent to a Poisson ratio of 0.33). This assumption is reasonable with <15% error in most polymers.

$$v_{s,L} = \frac{2d}{t_2 - t_1} \tag{41}$$

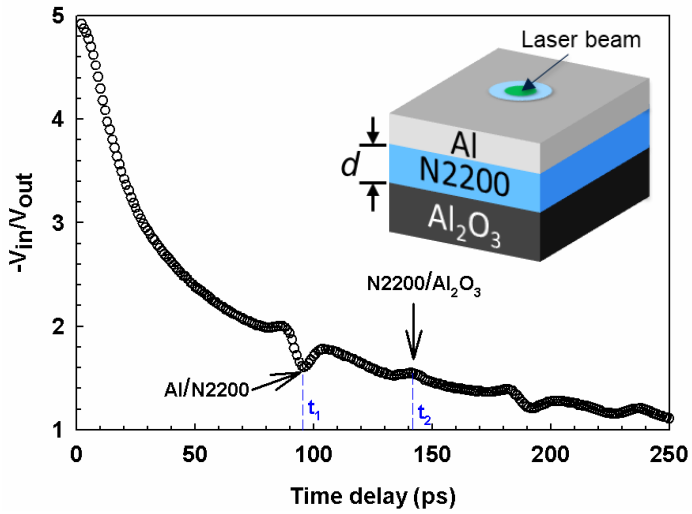

Figure 34 – Results of picosecond acoustics measurements on N2200/sapphire sample. The y-axis represents the ratio of magnitudes in-phase and out-of-phase voltage of the probe beam, and the x-axis is the time delay between the pump and probe. The acoustic echoes from the Al/N2200 and N2200/Sapphire interfaces are clearly observable

Speed of sound in P3HT is calculated indirectly from elastic modulus (*E*) measured by nanoindentation experiments using Hysitron Triboindenter. This approach is adopted due to the difficulty in performing picosecond acoustics on P3HT due to the diffuse reflection of the pump laser from the Aluminum transducer, which resulted in measurements with low signal-to-noise ratio. Nanoindentation experiments are performed at four different maximum loads at a total of 9 points in a 50×50 μm area. Results of the nanoindentation measurements are shown in Figure 35. The elastic modulus and the hardness are determined to be 4.8 GPa and 0.56 GPa, respectively. The longitudinal and transverse speeds of sound are calculated to be 2800 and 1400 m/s, respectively using equation (42), with Poisson ratio (υ) taken to be 0.33.

$$v_{s,L} = \sqrt{\frac{E}{\rho} \cdot \frac{(1-\upsilon)}{(1+\upsilon)(1-2\upsilon)}} \text{ and } v_{s,T} = \sqrt{\frac{E}{\rho} \cdot \frac{1}{2(1+\upsilon)}} \quad (42)$$

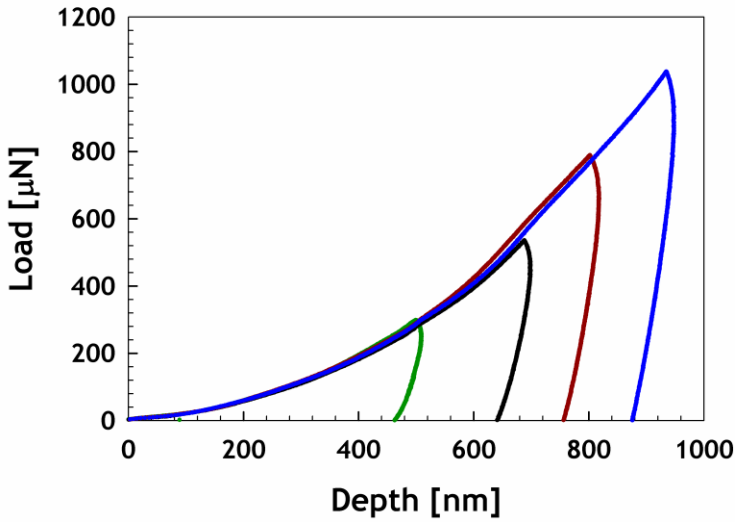

Figure 35 – Results of nanoindentation measurement on ~10 μm thick P3HT film on Si substrate. Four different maximum loads are chosen for measurement. The elastic modulus calculated from the unloading curves for all four scenarios are within 5% of each other indicating measurement precision.

Table 6 lists the measured through-plane and in-plane thermal conductivities of P3HT and N2200 along with the predictions of the k-min and empirical model. The speed of sound, specific heat, and density are also included. It can be readily observed that the prediction of k-min model is closer to the measured in-plane conductivity, while the empirical model is closer to the through-plane conductivity. While this is interesting, no significance can be attributed to this trend since both models assume isotropic material properties.

Table 6 – Summary of thermophysical properties of P3HT and N2200.

Polym-er	3ω measurements	Speed of sound	Density and heat capacity	Model predictions

	$k_\perp$ (W/m-K)	$k_\parallel$ (W/m-K)	$\frac{k_\parallel}{k_\perp}$	$v_{s,T}$ (m/s)	$v_{s,L}$ (m/s)	ρ (g/cc)	c (J/g-K)	n $\times 10^{22}$ (cm^{-3})	k_{min} (W/m-K)	k_{emp} (W/m-K)
P3HT	0.27± 0.02	0.35± 0.03	1.3	1400	2800	0.95± 0.05	1.53± 0.08	3.51	0.38	0.25
N2200	0.16± 0.01	0.27± 0.02	1.7	930	1860	1.32± 0.07	1.35± 0.07	4.30	0.29	0.17

4.3.2 N-type thermoelectric polymers

The suspended 3ω technique is also used to determine the in-plane thermal conductivity of two sets of n-type thermoelectric polymers – poly(nickel ethylenetetrathiolate), NiETT and poly(tetrathiooxolate), NiTTO.[99,100] In addition to in-plane conductivity, through-plane conductivity and volumetric heat capacity are also determined using the 3ω technique.

$k_\perp$ is determined by performing conventional 3ω measurements on a polymer film on a borosilicate glass substrate and fitting the data to the multilayer model. Polymer films (thickness ~5-10 μm) are obtained by drop casting NiETT and NiTTO dispersed in a PVDF matrix onto a borosilicate glass substrate. The films are then annealed at 160 °C for one hour in air on a hot plate. The measured 3ω signals are fit to equation (10) to simultaneously determine the $k_\perp$ and C, with measurement uncertainty determined using the Monte-Carlo approach. The films are then peeled off the substrate to obtain free-standing samples and suspended-film 3ω measurements are performed to determine $k_\parallel$. Measurement frequencies are chosen to satisfy the 1D approximation. Since the films used in this study have low electrical conductivities, an electrically insulating layer is not necessary to carry out 3ω measurements. Table 7 summarizes the measured thermophysical properties of NiETT and

NiTTO composite films with different alkali metal counterions.[101] It is evident that all polymer films exhibit anisotropy, with $k_{\parallel}/k_{\perp}$ between 1.5 and 2

Table 7 – Summary of thermophysical properties of NiETT and NiTTO

Polymer	$k_{\perp}$ (W/m-K)	$k_{\parallel}$ (W/m-K)	C (MJ/m^3-K)	$k_{\parallel}/k_{\perp}$
Li[NiETT]	0.20 ± 0.02	0.33 ± 0.03	1.85 ± 0.2	1.65
Na[NiETT]	0.18 ± 0.01	0.27 ± 0.02	1.67 ± 0.2	1.89
K[NiETT]	0.19 ± 0.02	0.37 ± 0.04	1.64 ± 0.2	1.95
Li[NiTTO]	0.24 ± 0.02	0.36 ± 0.04	1.71 ± 0.2	1.50
Na[NiTTO]	0.27 ± 0.02	0.40 ± 0.04	1.69 ± 0.2	1.48
K[NiTTO]	0.25 ± 0.03	0.42 ± 0.05	1.69 ± 0.2	1.68

This measurement approach can be extended to other thermoelectric polymers. However, for polymers with electrical conductivity higher than those used measured here (c.a., >1000 S/cm), a dielectric layer should be used to electrically insulate the metal heater from the polymer film to prevent Joule heating of the film. A similar 1D model can be used for data analysis to obtain an effective thermal conductance of the polymer and dielectric sample. Alternatively, a self-heating 3ω technique can be used for such polymers.

4.4 Summary

In this chapter, the suspended film 3ω technique to measure in-plane thermal conductivity of polymers is discussed with an approximate analytical 1D model used for data analysis. The necessary conditions to use this 1D model for suspended films are presented. These conditions provide geometrical and experimental constraints for applying the 1D model. PVDF, muscovite mica, and PEDOT:PSS are used to validate this approach, and the in-plane thermal conductivities are measured to be within 5% of the values reported

in the literature. This is followed by anisotropic thermal conductivity measurements of two common semiconducting polymers – P3HT (*p*-type) and N2200 (*n*-type), and recently developed *n*-type thermoelectric polymers – NiETT and NiTTO. Thermal anisotropies are observed in both polymers with greater thermal conductivity in the in-plane direction. The anisotropy can be attributed to the preferential alignment of polymer chains during the film preparation process, despite the polymer being generally amorphous in nature.

CHAPTER 5. THERMAL CHARACTERIZATION OF MODULATED NANOWIRES

5.1 Introduction

Semiconductor nanowires offer exciting opportunities to control thermal transport as their structure can be precisely engineered.[102,103] Thermal transport in semiconductors is primarily due to phonon transport and their thermal conductivity is limited by phonon scattering events.[39,104] In bulk intrinsic semiconductors, thermal conductivity is dominated by phonon-phonon scattering events, whose temperature dependence is well-understood. In doped semiconductors, phonon scattering with dopant (impurity) atoms become significant, generally resulting in a reduction in thermal conductivity. However, phonon-boundary scattering is usually dominant in nanostructures whose dimensions are comparable to phonon mean free path, which often results in a significant reduction in thermal conductivity compared to their bulk counterparts. Nanowire thermal conductivity is a strong function of their size and like their bulk counterparts, is also a strong function of temperature. However, the effects of morphology, diameter, and surface roughness on the thermal conductivity of nanowires are not fully understood, as complex nanowire geometries can be challenging to engineer.

This chapter focuses on temperature-dependent thermal conductivity measurements of nanowires with axially-modulated diameters using steady-state and transient (frequency domain) approaches.

5.2 Measurement platform

A commonly used platform to measure thermal conductivity of nanowires and related structures involves suspending the sample across two suspended pads, as shown in Figure 36.[105-108] Metal lines are fabricated on both pads which serve as heater-thermometers. One of the pads (heating pad) is Joule heated and the subsequent temperature rise of the other pad (sensing pad) is measured using resistive thermometry. Thermal conductivity is determined by fitting the measured values to an analytical thermal transport model. The thermal contact resistances between the nanostructure and the suspended pad is often neglected in this approach which could significantly affect the measurement accuracy.

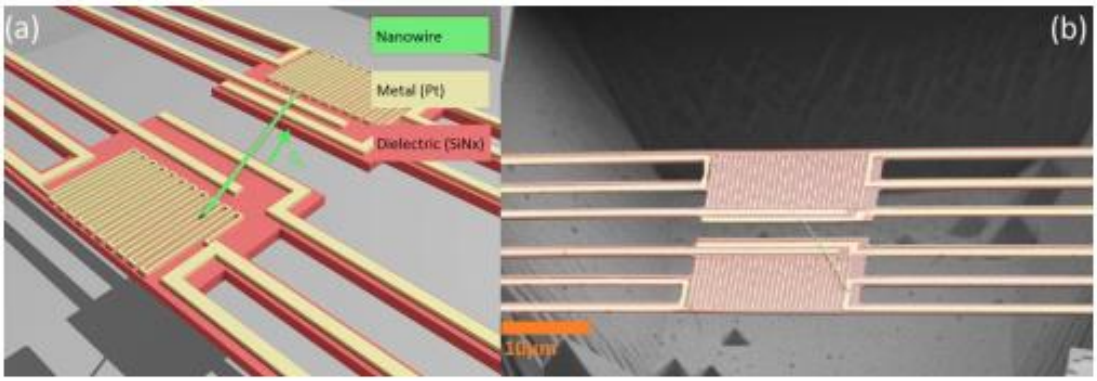

Figure 36 - (a) Schematic and (b) false colored SEM image of suspended beam microstructure commonly used to measure thermal conductivity of nanostructures. (Reproduced with permission from IOP publishing)

Recently, a four-probe suspended microbridge[109] measurement platform, as shown in Figure 37(a), has been proposed that can measure thermal properties of nanostructures independent of the thermal contact resistance. The nanowire is suspended across the four microbridges, with each microbridge serving as a metal heater-thermometer. The heat flow

along the nanowire and the temperature rise of the microbridges are measured by independently heating each microbridge. The microbridge structure with the nanowire suspended across can be represented using the thermal resistive network shown in Figure 37(b). Here, $T_{m,n}$ represents the temperature rise at the contact point of the m^{th} bridge and the nanowire when the n^{th} bridge is heated with heating amplitude P_n, $R_{th,m}$ is the thermal resistance of the m^{th} bridge, $R_{c,m}$ is the contact resistance between the m^{th} bridge and the nanowire, and R_1, R_2, and R_3 are the thermal resistances of the nanowire suspended between bridges 1-2, 2-3, and 3-4, respectively. The experimentally measured sixteen values of $T_{m,n}$ and four values of P_n are solved using the thermal resistive network shown in Figure 37(b) to determine the thermal resistance ($R_{nw,2}$) of the part of the nanowire suspended between the two central microbridges. The nanowire thermal conductivity (k_{nw}) is calculated using equation (43), where l_2 and d_{nw} are the length and diameter of the nanowire suspended between the 2nd and 3rd bridge. This four-bridge approach is adopted here to characterize the modulated nanowires.

$$k_{nw} = \frac{l_2}{R_{nw,2}\left(\pi d_{nw}^2 / 4\right)} \tag{43}$$

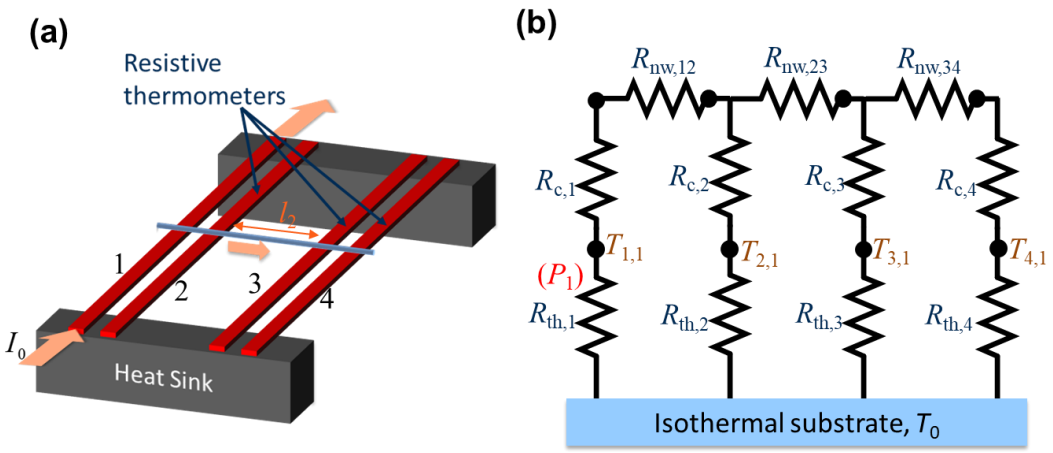

Figure 37 – (a) Schematic of the suspended microbridge structure with the nanowire across (b) Equivalent thermal resistive circuit of the microbridge structure with the nanowire suspended across it.

5.2.1 Suspended microbridge fabrication

An illustration of the fabrication of the suspended microbridge structure is shown in Figure 38. First, a 300 nm low stress silicon nitride (SiN_x) layer is grown atop a silicon substrate using LPCVD (step 1) using 100 sccm of dichlorosilane and 17 sccm of ammonia at 800 ˚C. A 60 nm thick Pt layer with 5 nm Cr adhesion layer is deposited at the rate 0.1 nm/s using e-beam evaporation (step 2). Photoresist (Futurrex NR71-3000p) is then spun-coat on the sample and is patterned using conventional photolithography (step 3). This is followed by an ICP etch to anisotropically etch the exposed Pt and SiN_x. Pt etching is carried out using a plasma of 8 sccm Cl_2 and 32 sccm Ar, and SiN_x etching is carried out using a plasma of 15 sccm C_4F_8, 28 sccm CO_2, and 5 sccm Ar. The patterned photoresist serves as a protective mask during the etching process. Post-etching, the photoresist is stripped using an acetone rinse to reveal four Pt/SiN_x microbridges, with each bridge connected to four pads in a four-probe configuration (step 4). This is followed by a second lithography step where the photoresist Microposit S1813 is spun-coat and patterned using

conventional photolithography to open an etch window exposing the bridges while covering the contact pads (step 5). In the final step, the Si exposed by the window is isotropically etched using xenon difluoride plasma. The depth of the trough is ~10 μm. Finally, the photoresist is stripped using an acetone rinse to obtain four suspended microbridges connected in four-probe configuration (step 6). Post fabrication, the wafer is diced, and individual devices are wirebonded to a dual in-line chip package for measurements. A SEM image of the measurement platform is shown in Figure 39. The width of the microbridge used in this study is ~ 1.5 μm and the bridges are separated by ~ 5 μm. Electron microscopy is also used to verify that the microbridges are completely suspended.

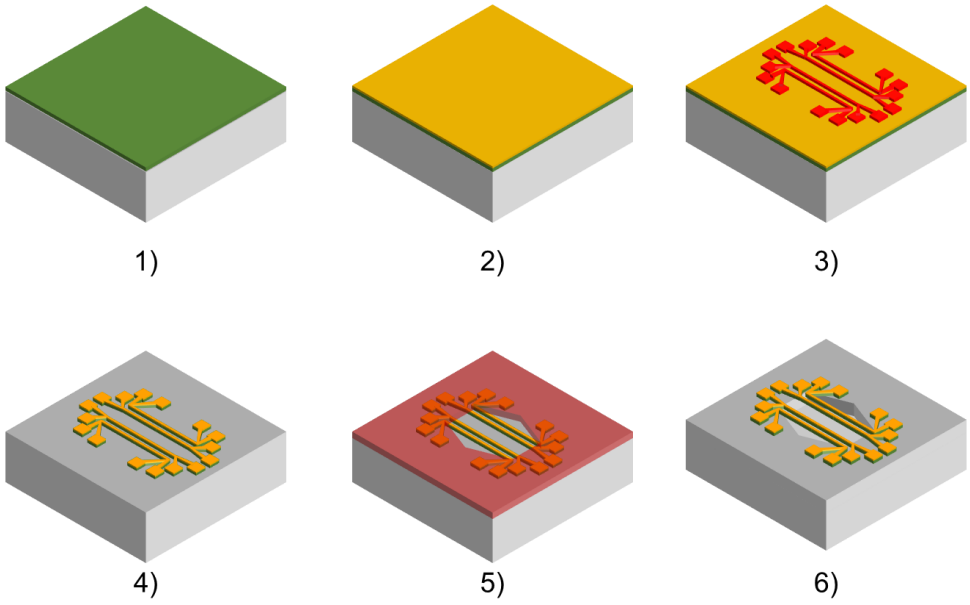

Figure 38 – Microfabrication flowchart for a suspended microbridge measurement platform.

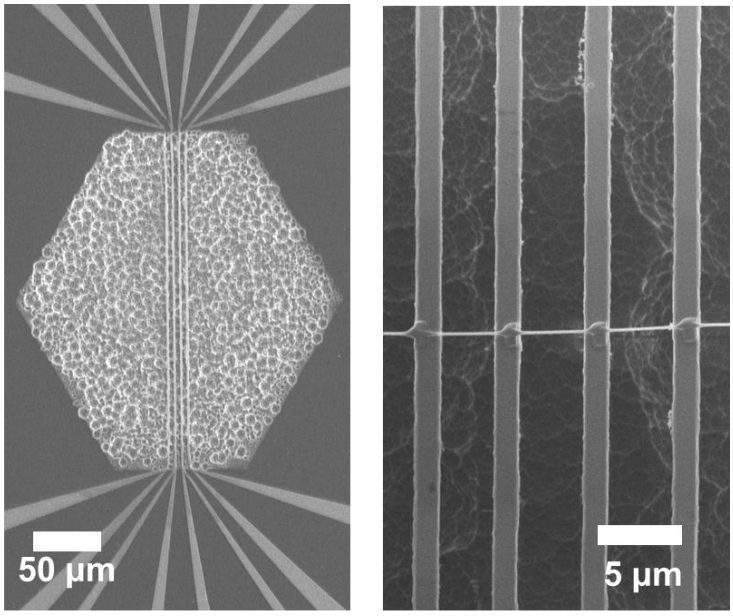

Figure 39 – SEM images of the suspended microbridge structure. The image on the right also shows the nanowire suspended across the microbridges.

5.3 Frequency-domain (AC) technique

While the steady state technique detailed in section 5.2 is useful for nanowire characterization, switching to a frequency domain variant has a couple of key advantages such as faster thermal response (time constant of the system is inversely proportional to modulation frequency) and improved accuracy (fitting experimental data at multiple frequencies to an analytical model reduces experimental uncertainty).

The frequency-domain (AC) variant is a modification of the 3ω technique. An AC current of magnitude I_n at a frequency ω is passed through the n^{th} microbridge (with electrical resistance R_n) to generate volumetric Joule heating with amplitude $P_n = I_n^2 R_n / 2$ at frequency 2ω. This creates a thermal wave that propagates across the microbridge-nanowire system, with all microbridges experiencing a temperature rise at 2ω, which in turn causes their electrical resistance to include a component at 2ω. The voltage drop across

heating microbridge has a 3ω component, which can be used to determine the average temperature rise ($\overline{T}_{n,n}$), similar to a conventional 3ω technique. To determine the average temperature rise of the sensing bridges ($\overline{T}_{m,n}$, $m \neq n$), a DC current is passed through the bridge which results in a voltage component at 2ω. This 2ω voltage component can be accurately measured using a lock-in amplifier and can be analyzed to obtain the average temperature rise, $\overline{T}_{m,n}$ ($m \neq n$) of the sensing bridges. With *m* and *n* ranging between 1 and 4, the sixteen values of $\overline{T}_{m,n}$ and four values of P_n can be analyzed using an analytical thermal model to obtain the thermal conductivity of the nanowire.

5.3.1 Thermal transport model

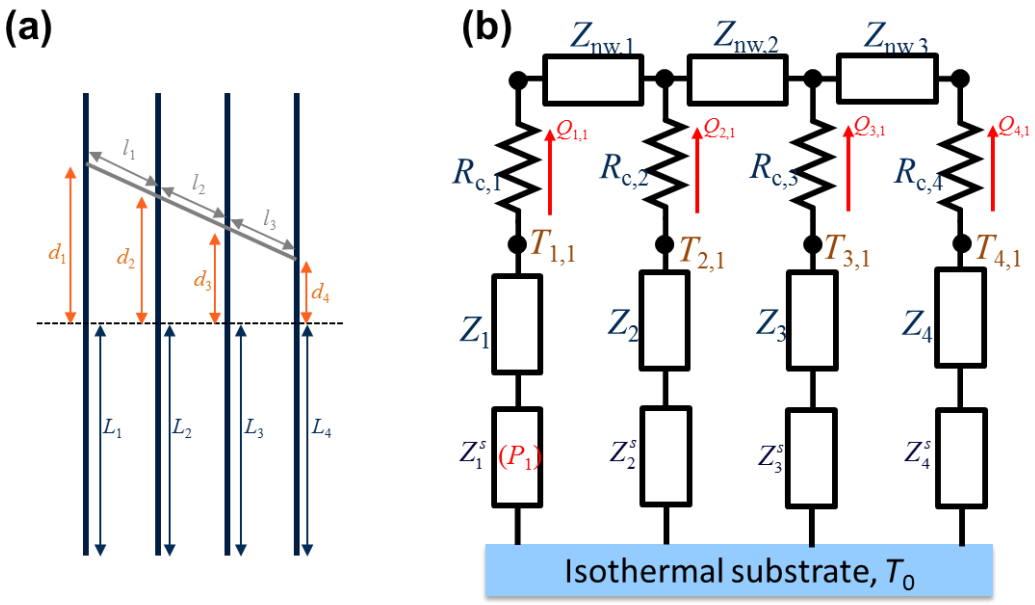

Figure 40 – (a) Schematic of the microbridge-nanowire system showing the key dimensions. (b) Equivalent thermal circuit of the suspended microbridge-nanowire system for an AC measurement with bridge 1 serving as the heating bridge.

Figure 40(a) also shows a top-down schematic of the microbridge platform with an off-centered nanowire. The half-length of the m^{th} microbridge is L_m and the deviation of its center from the point of contact to the nanowire is d_m. The frequency-domain measurement data can be analysed using an equivalent thermal circuit given in Figure 40(b). The rate of heat flow ($Q_{m,n}$) from the m^{th} microbridge to the nanowire when the n^{th} bridge is heated is also represented in the figure. Under the same heater configuration, the temperature $T_{m,n}$ shown in the figure is the temperature at the contact point of the nanowire and the m^{th} microbridge. Each microbridge is modelled as two impedances in series – impedance (Z_m^s) to volumetric heat generation P_n and impedance (Z_m) to the heat flow rate $Q_{m,n}$. The analytical expressions for the two impedances are given in equation (44). The derivations of these analytical expressions are presented in Appendix C.

$$\begin{aligned} Z_m &= \frac{3R_{\mathrm{th},m}}{12 + j\left(2R_{\mathrm{th},m}C_{\mathrm{th},m}\omega\right)} \\ Z_m^s &= \frac{R_{\mathrm{th},m}}{8 + j\left(2R_{\mathrm{th},m}C_{\mathrm{th},m}\omega\right)}\left(1 - \left(\frac{d_m}{L_m}\right)^2\right) \end{aligned} \tag{44}$$

$R_{\mathrm{th},m}$ and $C_{\mathrm{th},m}$ denote the thermal resistance and capacitance of the m^{th} microbridge given by equation (45), where L_m is the half-length, k_m is the effective thermal conductivity, S_m is the cross-sectional area, and C_m is the effective volumetric heat capacity of the microbridge. The derivation of impedances in equation (44) use Taylor series' expansions of hyperbolic trigonometric functions and are thus valid when $\omega R_{\mathrm{th}.m}C_{\mathrm{th},m} << 1$. This is generally valid for the microbridge properties and geometry, and experimental frequencies used. The impedance, $Z_{\mathrm{nw},m}$, of the segment of the nanowire suspended between bridges m and $m+1$ (m = 1,2,3) is given by equation (46), where l_m and d_m are the length and diameter

of the nanowire segment, respectively, and k_{nw} and C_{nw} are the thermal conductivity and volumetric heat capacity of the nanowire, respectively. This expression is obtained using a lumped first-order system approximation.

$$R_{\mathrm{th},m} = \frac{2L_m}{k_m S_m} \text{ and } C_{\mathrm{th},m} = 2L_m S_m C_m \tag{45}$$

$$Z_{\mathrm{nw},m} = \frac{R_{\mathrm{nw},m}}{1 + j\left(R_{\mathrm{nw},m} C_{\mathrm{nw},m} \omega\right)}, \text{ where } R_{\mathrm{nw},m} = \frac{l_m}{k_{\mathrm{nw}}\left(\frac{\pi d_m^2}{4}\right)}, \; C_{\mathrm{nw},m} = l_m\left(\frac{\pi d_m^2}{4}\right)C_{\mathrm{nw}} \tag{46}$$

The microbridge impedances can then be related to the temperatures $T_{m,n}$ using equation (47). Here, δ_{mn} is the Kronecker delta function which takes the value 1 or 0 depending on whether $m = n$ or $m \neq n$, respectively.

$$T_{m,n} = P_n Z_m^s \delta_{mn} - Q_{m,n} Z_m \tag{47}$$

Solving the thermal circuit requires the knowledge of temperatures $T_{m,n}$,, which can be related to experimentally measured $\bar{T}_{m,n}$ using equation (48).

$$\begin{aligned} T_{m,n} &= \bar{T}_{m,n} \cdot \frac{\left(4 + jR_{\mathrm{th},m} C_{\mathrm{th},m} \omega\right)}{\left(2 + jR_{\mathrm{th},m} C_{\mathrm{th},m} \omega\right)}, \text{ for } m \neq n \\ T_{n,n} &= P_n Z_n^s - Z_n \cdot \sum_{m \neq n}\left(\frac{\bar{T}_{m,n}}{Z_m^s}\right) \end{aligned} \tag{48}$$

In the limit of $\omega \rightarrow 0$, the solution described by the above equations simplifies to the steady-state solution. Frequency-dependent experimental values of $\bar{T}_{m,n}$ are fit to the thermal

circuit described by equations (44)-(48) to obtain thermal conductivity of the nanowire. The derivations of these expressions are discussed in Appendix C.

5.4 Validation of the measurement approach on modulated nanowires

The frequency-domain approach detailed in the previous section is used to measure thermal conductivity of Silicon nanowires and are compared against the results obtained using the steady-state approach, which will aid in validating the frequency-domain approach. The nanowires measured in this chapter are axially modulated with repeated doped and undoped segments, synthesized using the vapor-liquid-solid (VLS) mechanism.[110] Post growth, the doped segments are selectively etched to obtain modulated nanowires with periodic doped and undoped segments of varying diameters. This is illustrated in Figure 41, along with the corresponding SEM image. Two non-dimensional parameters, defined by equation (49), are used to characterize the nanowires.

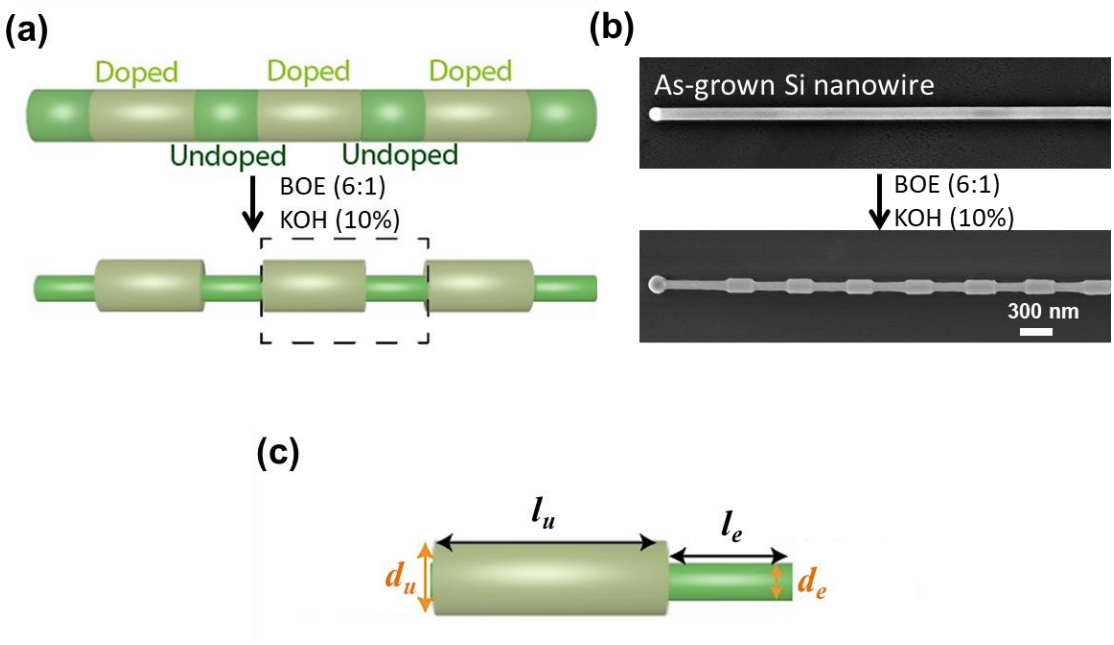

Figure 41 – (a) Illustration of the synthesis of axially modulated nanowires. The post-growth selective etching of doped segments is carried out using buffered oxide etch (BOE) and potassium hydroxide (KOH). (b) SEM images of the nanowire before and after the etching process. (c) Illustration of the etched and unetched segments highlighting the critical dimensions.

$$\bar{L} = \frac{l_e}{l_e + l_u} \quad \bar{D} = \frac{d_e}{d_u} \tag{49}$$

To understand the effect of diameter modulation on the thermal conductivity, two different etched and modulated nanowire geometries (two sets of $\bar{L}$ and $\bar{D}$) are studied and compared to the unetched nanowire. SEM images of different nanowire geometries measured are shown in Figure 42. In all samples, the diameter of the unetched segment is kept nearly constant at ≈165 nm during the fabrication process.

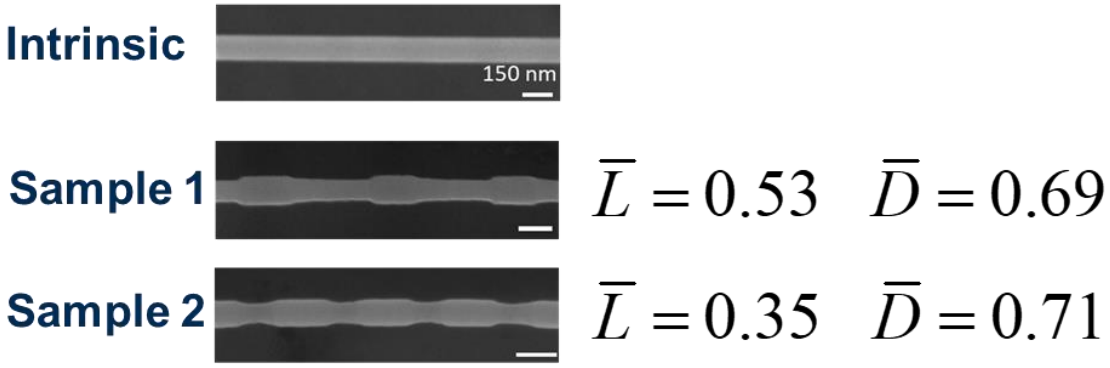

Figure 42 – SEM images of the nanowires measured in this chapter. Samples 1 and 2 are axially modulated with repeated doped and undoped segments. Sample 0 is the intrinsic nanowire. The doped segments of samples 1 and 2 are etched post-growth to precisely control the geometry.

The nanowires are suspended across the microbridges and the contact between the microbridge and the nanowire is established through Pt deposition using a focused ion beam (see Figure 39). This also helps in in minimizing contact resistance, thus improving measurement sensitivity. Thermal conductivity measurements are performed using both steady-state and frequency-domain approaches. Temperature-dependent measurements between 30 and 300 K are performed in a closed-loop Helium cryostat.

As a parallel effort, thermal conductivity of the nanowires is calculated using a theoretical approach[111] based on the Boltzmann transport equation (BTE). The thermal conductivity of the doped and undoped segments are calculated independently using equation (50), where C is the heat capacity, v is the phonon group velocity, Λ_{eff} is the effective phonon mean free path, and subscripts $\boldsymbol{q}$ and s indicate the wave vector and phonon branch, respectively. An effective medium approach is then used to calculate the thermal conductivity of the etched modulated nanowire. The effective mean free path in the BTE accurately accounts for the phonon-interface interactions using the Beckmann-

Kirchhoff surface scattering theory.[112] The model accounts for the surface roughness, η, of the nanowires and the proportion of specularly scattered phonons, ($0 \leq p \leq 1$, with $p = 0$ corresponding to maximum surface roughness). This allows for a more accurate prediction of thermal conductivity.

$$k_{\mathrm{BTE}} = \sum_{\boldsymbol{q},s} \left(C_{\boldsymbol{q},s} v_{\boldsymbol{q},s} \Lambda_{\mathrm{eff},\boldsymbol{q},s} \right) \tag{50}$$

Figure 43 shows the temperature-dependent measurements on the intrinsic nanowire (sample 0). The experimental uncertainties are calculated using a Monte Carlo approach. The predictions of the model are also shown in the figure. Since the thermal conductivity is limited by phonon-boundary scattering, it is a strong function of the surface roughness of the nanowire with the highest thermal conductivity corresponding to a smooth surface. The uncertainty in the model is based on the variation in the diameter of the nanowire. As can be noticed in Figure 43, model prediction with a surface roughness of 0.5 nm agrees with the experimental data within uncertainty limits.

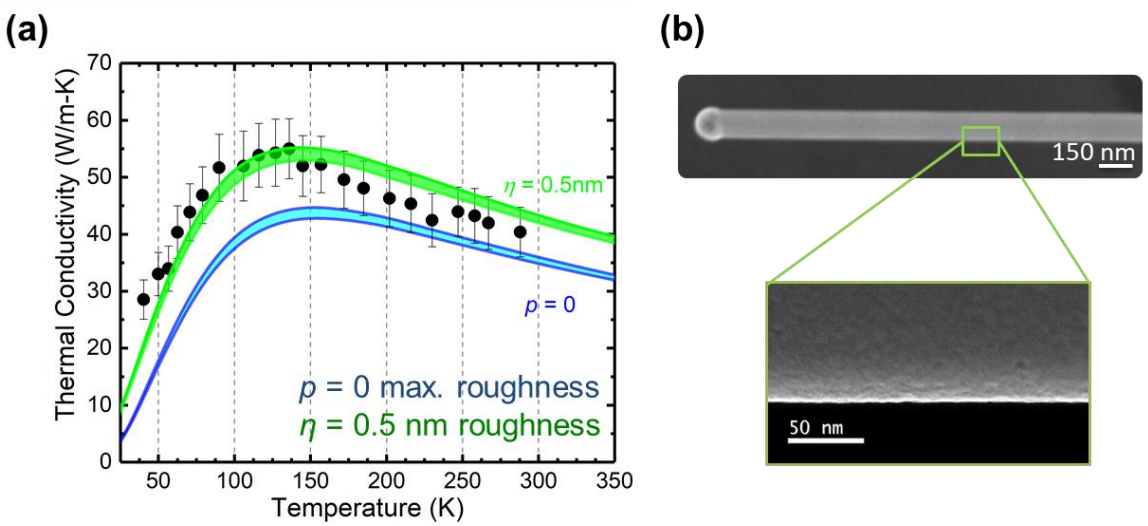

Figure 43 – (a) Measured and predicted thermal conductivity of the intrinsic nanowire (sample 0). It is observed that model prediction with a surface roughness of 0.5 nm agrees well with the measurements. (b) Zoomed-in view of the nanowire showing the surface roughness.

The measurement of the intrinsic nanowire is followed by similar temperature-dependent measurements of the etched nanowires. This is shown in Figure 44. Measurements were performed using both steady-state and frequency-domain approaches. The Monte-Carlo approach is used to determine measurement uncertainty for the AC approach. To determine the thermal conductivity of etched nanowires using equations (43) and (46), the larger diameter (of the unetched segment) is used as d_{nw}. This diameter allows for a direct comparison of thermal conductivities with the intrinsic nanowire. It is observed that the experimental data and model predictions agree within the uncertainty limits at lower temperatures (T < 130 K) but the model overpredicts the thermal conductivities at higher temperatures. This suggests the presence of increased phonon scattering at higher temperatures, resulting in a lower experimental thermal conductivity.

It can also be readily observed that the measurements from the steady-state and frequency-domain approach agree well with each other within the limits of uncertainty for both samples over the entire temperature range. This serves as a validation for the modified 3ω approach. This approach has a lower measurement uncertainty compared to the steady-state approach because it involves fitting data across multiple frequencies and the voltages are accurately measured using a lock-in amplifier

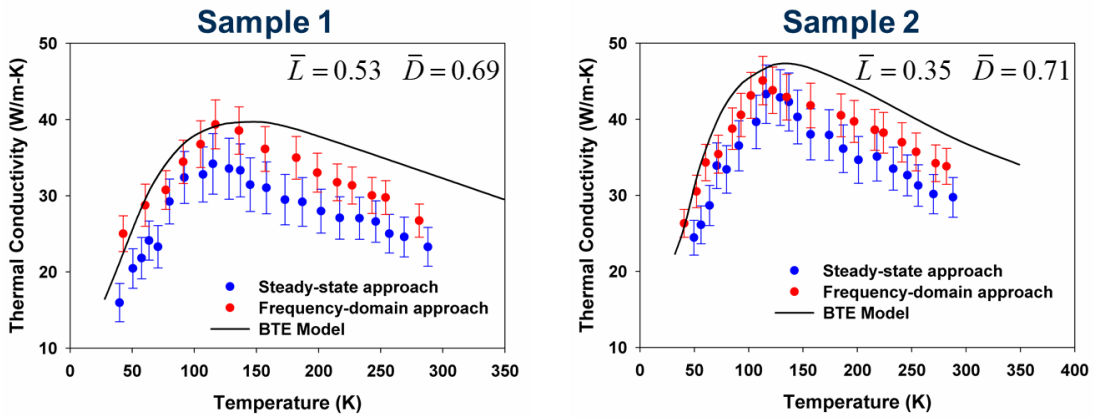

Figure 44 – Measured and predicted thermal conductivity of etched-modulated nanowire samples 1 and 2. The measurements from the AC approach agree well with the steady-state measurements, thus validating the modified AC approach.

Another key observation from Figure 44 is the effect of $\bar{L}$ and $\bar{D}$ on thermal conductivity. By decreasing the diameter of the etched segment and/or increasing the length of the etched segment, a reduction in thermal conductivity is observed. In other words, thermal conductivity decreases as $\bar{L}$ increases and/or $\bar{D}$ decreases. This trend can be explained by the increased phonon-boundary scattering in nanowires with longer and/or narrower etched segments.

5.5 Summary

This chapter explores the utility of frequency-domain electrothermal measurement of nanowire thermal conductivity. The nanowires of interest are axially modulated with repeated doped and intrinsic segments, whose doped segments are etched post-growth to varying degrees. Two dimensionless parameters are defined to study the effect of nanowire geometry on its thermal conductivity. The experimental values are also compared with the predictions of a theoretical model based on the Boltzmann transport equation and effective medium theory. The experimental results on the etched nanowires agree well with the model at $T < 130$ K, but is lower than the model predictions at higher temperatures

Thermal conductivity measurements of nanowires are performed using a steady-state (DC) approach documented in previous literature and a frequency-domain (AC) variation detailed in this chapter. The data analysis in the AC method is performed using a simplified thermal circuit with the microbridge and nanowire modelled as thermal impedances. The two methods yield similar values of thermal conductivity in the temperature range 30-300 K, which suggests the applicability of the AC technique.

CHAPTER 6. CONCLUSIONS AND FUTURE DIRECTIONS

The 3-omega technique is an electro-thermal characterization technique that is commonly used to measure thermal conductivity of thin films on substrates. The measurement approach involves relatively straight forward microfabrication (often metal deposition through a shadow mask) and has high levels of accuracy and precision, particularly in measuring low thermal conductivity materials such as polymers. The data analysis involves fitting experimental measurements to robust analytical models, which results in the 3ω technique generally having a higher accuracy than steady-state and transient time-domain techniques such as transient plane source and transient hot wire. Furthermore, the versatility of the technique allows for characterization of powders, liquids, and gases using a metal-coated fiber heater.

Herein, four applications of thermophysical characterization using the 3ω technique are explored, which showcase the versatility of the technique. This dissertation is intended to provide a useful foundation to researchers working on 3-omega or other related aspects of thermal characterization. The key findings of this thesis could be further explored to gain additional scientific insights. As an example, the empirical model could be improved by using more recent results of atomistic simulations and broader experimental set of data. The variants of 3ω discussed in chapters 4 and 5 serve as a good basis for further modifications characterization of additional micro/nano-structures. The key findings of this dissertation could provide useful starting points for answering additional scientific questions, some of which are briefly discussed in Section 6.2.

6.1 Thesis questions

The conclusions and intellectual contributions of this work can be presented by answering the four questions mentioned in Section 1.3.

What are the limits of sensitivity achievable using a gas sensor based on 3ω technique? And to what extent can a balance between sensitivity and power consumption be realized?

The 3ω technique is used for gas sensing using two different sensor geometries – a suspended polysilicon microbridge and a gold-coated glass fiber, and experiments are performed on binary gas mixtures of He, Ar, CH_4, and CO_2 in N_2. Based on a differential approach to data analysis, composition curves for both sensor geometries are developed which relate gas concentration to experimental signals. The sensitivity of this approach is demonstrated to be ~100 ppm with the sensor power consumption <10 mW. The sensitivities are comparable with some of the best TCDs in literature, with a much lower power consumption (~10 % of conventional wheat-stone bridge TCDs). The sensitivity of the sensor is inversely proportional to the power consumption, as demonstrated by the metal-coated fiber sensor. The sensitivity can be further improved by sourcing higher currents through the 3ω heater.

The composition curve based on the phase signal is found to be independent of the sourcing current amplitude and has the advantage of not requiring a current-dependent calibration for individual sensors. This approach could be useful in remote sensing applications.

How accurately can an empirical model based on experimental 3ω data predict temperature-dependent thermal conductivity of amorphous polymers?

An empirical model that can aid in predicting temperature-dependent thermal conductivity of amorphous polymers is developed based on kinetic theory of vibrations. The model explicitly accounts for contributions of different vibrational modes in polymers – propagons, diffusons, and locons. The contribution from localized modes (locons) is found to negligible, which agrees with MD simulations on polymers. The empirical model is fully characterized and validated using experimental measurements of thermal conductivity.

The model depends only on fundamental material properties such as density, monomer molecular weight, and speed of sound. The model improves upon the existing Cahill-Pohl k-min model, particularly at low temperatures (< 50 K). Besides predicting the temperature-dependent thermal conductivity, the model can be used to explicitly calculate the contributions of propagating and diffusive modes, along with the range of their vibrational frequencies. The predictions of the model in the temperature range of 1-300 K are in good agreement with experimental data, with a R^2 value greater than 0.75. The model has an upper limit, which can be used to predict the room temperature thermal conductivity of polymers. This limit is in good agreement (generally within 30%) with experimental values of a variety of polymers reported in literature. It is observed that the room temperature prediction is generally lower than the experimental value, which can be partly explained by the absence of locon contribution in the empirical model.

To what degree of accuracy can the 3ω technique measure anisotropic thermal conductivities in polymers? What degree of anisotropy in thermal conductivity is observed in semiconducting polymers?

While conventional 3ω methods have been modified to measure in-plane thermal conductivity, they often face challenges such as complex microfabrication and/or low measurement accuracy. A suspended film 3ω method is explored which overcomes these two key challenges. Data analysis in this method is performed using an approximated 1-D heat transfer model, which is valid for narrow heater lines and thin films. The necessary conditions to use the 1-D model are presented, which provides design and experimental criteria for the suspended film method. Thermal conductivity determined using this method does not require the exact knowledge of heater width and through-plane thermal conductivity, which results in experimental uncertainty lower than 5%. This is an improvement over conventional 3ω methods to characterize anisotropy.

The suspended film method is then used to measure in-plane thermal conductivities of a few semiconducting polymers, including NiETT and NiTTO, two recently developed n-type thermoelectric polymers. A thermal conductivity ratio (in-plane to through-plane) of ~1.5-2 is noticed in all polymer films measured, which is important to determine thermoelectric figure of merit, zT.

How accurately can a variant of 3ω technique measure thermal conductivities of nanowires and other nanostructures?

A measurement platform with four suspended Pt/SiN_x microbridges, each of which serve as a heater/thermometer is discussed in Chapter 5. A variant of 3ω technique, which

involves sourcing a sinusoidal current (frequency ω) through one microbridge and sensing the temperature rise (frequency 2ω) of the others. By sweeping across a range of frequencies, the experimental data are fit to an approximated thermal circuit which models the microbridge and nanowire as thermal impedances. The circuit model is validated using COMSOL Multiphysics simulations and the experimental results obtained using this AC approach are in agreement with a steady-state (DC) approach documented in previous literature, thus validating of the data analysis procedure.

The measurement uncertainty using the AC approach (~7 %) is generally lower than the DC approach (~12 %), highlighting its utility. Using this approach, temperature-dependent thermal conductivity of nanowires with axially modulated doped and undoped segments are measured. The doped segments are etched post-growth to study the effect of the modulation on the effective nanowire thermal conductivity.

6.2 Future directions

While this dissertation explores a few applications of thermophysical characterization using 3ω technique, the technique can be extended a few additional applications that build on this work. The differential method is used here to measure thermal conductivity of polymers as a function of temperature, with a focus on cryogenic temperatures. Similar measurements can be performed at higher temperatures to capture the effects of glass transition on thermal transport. The 3ω technique is advantageous for these measurements as glass transition affects surface morphology, which has very little impact on the measurement technique. The measured values can be compared with the predictions of the empirical model in chapter 3. These results could be used to further

improve the empirical model to broaden its scope. Block copolymers[113,114] and cross linkable polymers[115,116] are interesting samples as they facilitate further understanding of the effect of polymer chain mobility and interlinking on the thermal conductivity. The suspended film technique can be used in conjunction to quantify the anisotropy in these samples.

Another area of interest involves thermal characterization of high temperature heat transfer media (HTM) in applications such as concentrated solar power (CSP) generation and storage.[117] There is a lack of suitable characterization techniques and the 3ω technique with a modified metal-coated-fiber heater can be used here. This can be used to simultaneously determine k and C of the HTM by sweeping across a wide range of frequencies. Appropriate fibers and metal layers must be chosen to withstand the high temperatures, and a protective cladding layer around the metal is required to prevent the corrosion by the HTM.

Lastly, the suspended microbridge measurement platform with the AC modification can be used to characterize polymer fibers and understand thermal transport in these (semi-crystalline) polymers. Recently, organics systems that undergo reversible (photochemical) polymerization – (thermal) depolymerization have been synthesized.[118] Temperature-dependent measurements on such samples can be used to further explore the nature of thermal transport in polymer fibers. The switchable nature of (de)polymerization could provide a path to interesting applications.

APPENDIX A. 3-OMEGA CIRCUIT

The 3-Omega circuit used for our measurements is illustrated in Figure 45. The variable ballast resistor discussed in the paper is indicated by block A in the circuit. The terminals labeled 2400-I and 2400-V (front and rear) connect to the respective terminals of Keithley 2400 Sourcemeter and will be used to measure the resistance of the sample and the ballast, respectively. The outputs corresponding to the voltage across the sample and the ballast are connected to the AD524CD precision instrument amplifier, which is used to match the impedances of the respective circuits. These amplifiers can also be used to apply a variable gain (between 1 and 1000) to the voltage drop across the sample and the ballast. This could be used to measure smaller voltages under 10 μV. The block B in the circuit corresponds to the voltage reducer circuit, which is connected to the NI-USB 6009 Data Acquisition unit through the D-Sub connection. The reduction constant (sample resistance / ballast resistance) is input to the AD7541A KN digital-to-analog converter, which modifies the voltage drop across the ballast to nearly match the 1ω voltage drop across the sample.

This 3-Omega circuit offers versatility in measurement as the reducer circuit can be connected either to the sample or ballast, depending on the application. The voltage signals from the two precision instrument amplifiers (one of which is also connected to the reducer circuit) are fed to a SR-850 lock-in amplifier, which measures the 3ω component of voltage. The relay circuit, shown in block C is used to switch the sample connections between the Keithley 2400 and the lock-in. The relays in the circuit are controlled by the user, using the NI DAq card.

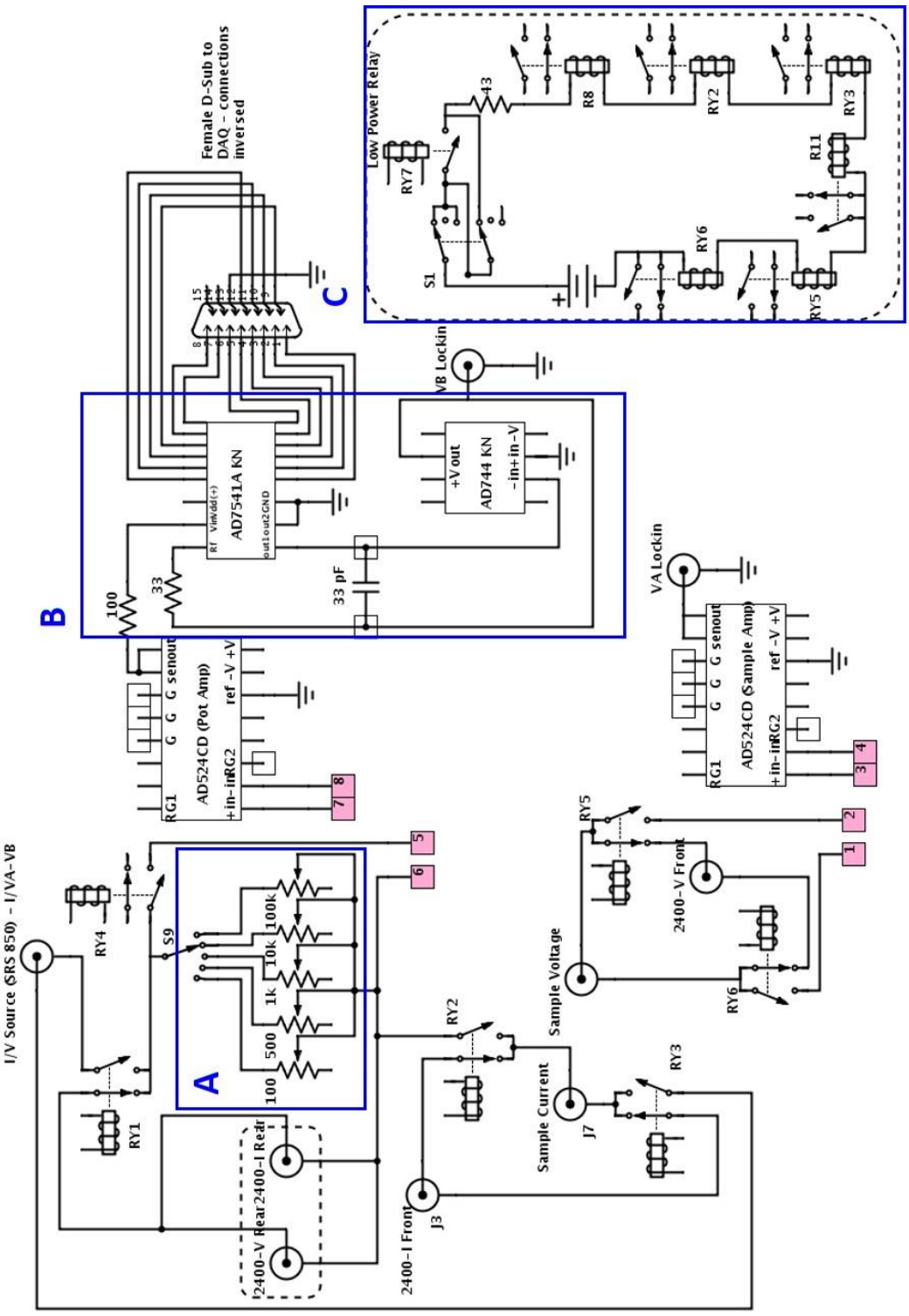

Figure 45 – Schematic of the 3-omega circuit used

APPENDIX B. ERROR PROPAGATION ANALYSIS

The measurement uncertainty in the slope method, differential method, and the suspended film method can be estimated using standard error propagation analysis. The thermal conductivity of a substrate using slope method is given by equation (51), which is obtained by combining equations (9) and (13). Here, $\partial\left(V_{\text{in,RMS}}\right)/\partial\left(\ln\omega\right)$ is the slope of the linear fit between the RMS value of in-phase component of 3ω voltage and the logarithmic frequency.

$$k_{\text{sub}} = \frac{-P_0}{4\pi L}\left(\frac{dR}{dT}\right) I_{\text{RMS}} \frac{1}{\left[\partial\left(V_{\text{in,RMS}}\right)/\partial\left(\ln\omega\right)\right]} \tag{51}$$

Similarly, the thermal conductivity of a thin film on substrate using differential method is given by equation (52), which is obtained by combining equations (9) and (14). In deriving this equation, it is assumed that *dR/dT* of the heater lines on the substrate and the film-on-substrate are different, which is common during 3ω experiments.

$$k_{\text{film}} = \frac{P_0 d_{\text{f}}}{4bLI_{\text{RMS}}}\left[\frac{1}{\left(\frac{\left(dR/dT\right)}{V_{\text{in,RMS}}}\right)_{\text{film+sub}} - \left(\frac{\left(dR/dT\right)}{V_{\text{in,RMS}}}\right)_{\text{sub}}}\right] \tag{52}$$

Lastly, the thermal conductivity using the 1D model for the suspended film technique is given by equation (53), which is obtained by combining equations (9) and (38).

$$k_{\parallel} = \frac{P_0^2\left(dR/dT\right)^2}{32d^2C}\left(\frac{I_{\text{RMS}}}{V_{3\omega,\text{RMS}}}\right)^2 \tag{53}$$

In these cases, the measurement uncertainty (u_k) can be calculated using simple error propagation, according to equation (54), where j indicates all variables presented in the respective equations, and u_j is the uncertainty of parameter j.

$$u_k = \sqrt{\sum_j \left(\frac{\partial k}{\partial j} \cdot u_j \right)^2} \tag{54}$$

Since the lock-in amplifier, current source, and sourcemeter are very accurate, uncertainties in V_{in}, $V_{3\omega}$, I_{RMS}, P_0 are typically negligible. The heater length, L, is also very precise and can be neglected. The contribution to the uncertainty in thermal conductivity from these parameters cumulatively is typically < 1 %. The largest contributors to the uncertainty are dR/dT, b and d.

APPENDIX C. THERMAL CIRCUIT ANALYSIS FOR FREQUENCY-DOMAIN MICROBRIDGE TECHNIQUE

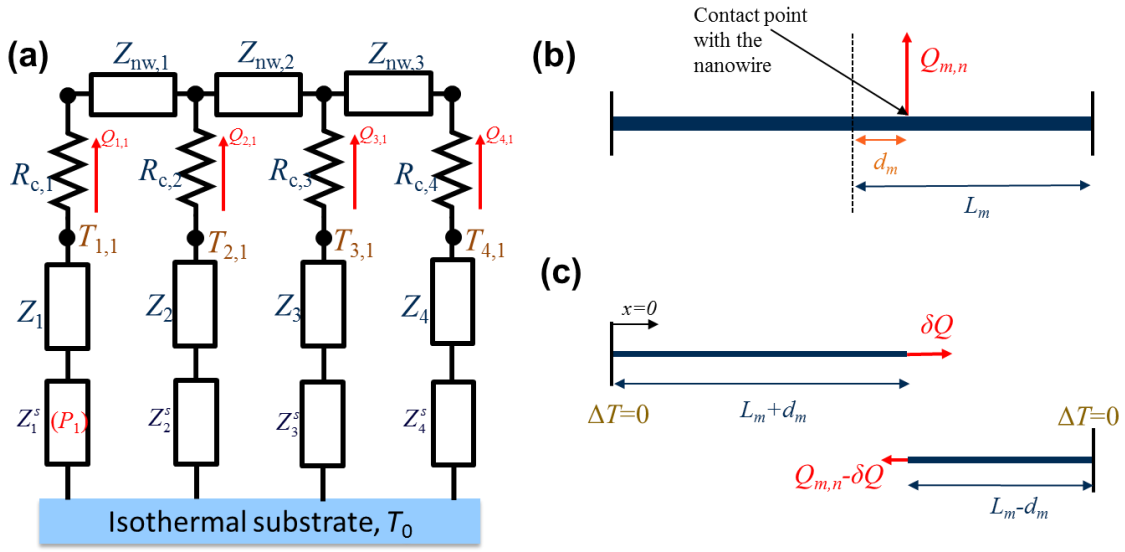

Figure 46 – (a) Thermal circuit showing the directions of heat flow. (b) Schematic of m^{th} microbridge when n^{th} microbridge is heated. (c) The left and right parts of the microbridge are analyzed separately using a 1D heat diffusion equation.

Figure 46(a) shows the thermal impedance circuit with bridge 1 serving as the heater. When n^{th} microbridge serves as the heater, $Q_{m,n}$ denotes the amplitude of the heat flow from m^{th} microbridge to the nanowire. Figure 46(b) shows the schematic of m^{th} microbridge. The 1-D heat diffusion equation is solved for each microbridge to obtain $Z_{m,n}$. The parts of the microbridge to the left and right of the contact point with the nanowire are solved independently using the equation (55). Here, $T(x,t)$ is the temperature rise at location x and time t, P_n is the amplitude of heating power in the n^{th} microbridge, and δ_{mn} is the Kronecker delta function. Since the thermal wave is at a frequency 2ω, equation (55) can be simplified to equation (56) using $T(x,t) = \Delta T(x)e^{j(2\omega t)}$.

$$C_m \frac{\partial}{\partial t}\left[T\left(x,t\right)\right] - k_m \frac{\partial^2}{\partial x^2}\left[T\left(x,t\right)\right] = \frac{P_n}{2L_m S_m} e^{j(2\omega t)} \delta_{mn} \tag{55}$$

$$2\omega C_m \left[\Delta T\left(x\right)\right] - k_m \frac{d^2}{dx^2}\left[\Delta T\left(x\right)\right] = \frac{P_n}{2L_m S_m} \delta_{mn} \tag{56}$$

This second-order ODE can be solved for the left and right parts of the microbridge with the boundary conditions in equation (57) to obtain the temperature distribution along the microbridge. The temperatures $T_{m,n}$ and $\bar{T}_{m,n}$ can be calculated using equation (58).

$$\begin{aligned} &\Delta T\left(0\right) = \Delta T\left(2L_m\right) = 0 \\ &\text{At } x = L_m + d_m,\ \Delta T\left(x^-\right) = \Delta T\left(x^+\right) \\ &\text{At } x = L_m + d_m,\ \frac{d}{dx}\left[\Delta T\left(x^+\right)\right] - \frac{d}{dx}\left[\Delta T\left(x^-\right)\right] = \frac{Q_{m,n}}{k_m S_m} \end{aligned} \tag{57}$$

$$T_{m,n} = \Delta T\left(x = d_m\right) \text{ and } \bar{T}_{m,n} = \frac{1}{2L_m} \int_0^{2L_m} \Delta T\left(x\right) dx \tag{58}$$

The general solution to equation (56) involves hyperbolic trigonometric functions. The hyperbolic functions are simplified using their Taylor series' expansions and neglecting terms of 3rd order and higher. The simplified solution is given by equation, valid for $\omega R_{\text{th},m} C_{\text{th},m} << 1$. The inequality criterion is comfortably satisfied for the microbridge-nanowire system used here. The simplified solution and equation (58) can be solved to obtain equations (59) and (60). Equation (59) is identical to equation (47), with the first-term on the right side representing the contribution from volumetric heat generation and the second-term representing the contribution from the heat flow rate. The analytical expressions of the two impedances, Z_m^s and Z_m are evident from equation (59)

$$T_{m,n} = \frac{R_{\text{th},m}}{8 + j2\omega R_{\text{th},m} C_{\text{th},m}} \left(1 - \left(\frac{d_m}{L_m}\right)^2\right) P_n \delta_{mn} - \frac{3R_{\text{th},m}}{12 + j2\omega R_{\text{th},m} C_{\text{th},m}} Q_{m,n} \tag{59}$$

$$\bar{T}_{m,n} = \frac{R_{\text{th},m}}{12 + j2\omega R_{\text{th},m} C_{\text{th},m}} P_n \delta_{mn} - \frac{R_{\text{th},m}}{8 + j2\omega R_{\text{th},m} C_{\text{th},m}} Q_{m,n} \tag{60}$$

The segments of nanowire suspended between consecutive microbridges are modeled as a thermal resistance in parallel with a lumped capacitance, with the effective impedance given by equation (61).

$$Z_{\text{nw},m} = \frac{1}{\frac{1}{R_{\text{nw},m}} + j2\omega C_{\text{nw},m}} = \frac{R_{\text{nw},m}}{1 + j2\omega R_{\text{nw},m} C_{\text{nw},m}} \tag{61}$$

The heat flow rates $Q_{m,n}$ can be related using equation (62). This is an approximation that is valid for low frequencies ($\omega R_{\text{nw}} C_{\text{nw}} << 1$) and low nanowire capacitance ($C_{\text{nw}}/C_{\text{th},m} << 1$). These assumptions are reasonable for nanowire geometries and properties, and experimental frequencies (< 500 Hz) used here. This approximation has also been verified by comparing the above thermal circuit against a detailed COMSOL Multiphysics simulation. The desired nanowire impedance can be related to the heat flow rates and contact temperatures by equation (63). Equation (48) can be obtained by combining equations (60) and (62)

$$\sum_m Q_{m,n} = 0 \tag{62}$$

$$T_{2,n} - T_{3,n} = Q_{2,n} R_{\text{c}2} - Q_{3,n} R_{\text{c}3} + \left(Q_{1,n} + Q_{2,n}\right) Z_{\text{nw},2} \tag{63}$$

C.1 Data Analysis Routine

In a typical experiment, the sixteen average temperature rises of microbridges $\bar{T}_{m,n}$ are measured as function of sourcing current frequency. The heating power amplitude P_n can be calculated based on the sourcing current and electrical resistance of the microbridge. The data fitting routine to determine nanowire thermal conductivity is as follows:

1) Experimental data are fit to equation (60) to obtain $R_{\mathrm{th},m}$, $C_{\mathrm{th},m}$, $Q_{m,n}$.
2) $T_{m,n}$ is calculated using equation (59).
3) The values of $Q_{m,n}$ and $T_{m,n}$ are plugged into equation (63) and the nanowire thermal conductivity is determined from equation (61) based on the least squares fit.

Since the thermal circuit model involves a few approximations, it is thoroughly validated using COMSOL Multiphysics simulations for a range of nanowire geometries and thermal conductivities.

REFERENCES

1 Thompson, D. R., Rao, S. R. & Cola, B. A. A stepped-bar apparatus for thermal resistance measurements. *Journal of Electronic Packaging* **135**, 041002 (2013).

2 Smirnov, M., Khokhlov, V. & Filatov, E. Thermal conductivity of molten alkali halides and their mixtures. *Electrochimica acta* **32**, 1019-1026 (1987).

3 Flynn, D. R. in *Compendium of Thermophysical Property Measurement Methods: Volume 2 Recommended Measurement Techniques and Practices* (eds K. D. Maglić, A. Cezairliyan, & V. E. Peletsky) 33-75 (Springer US, 1992).

4 ASTM-D1518-14. Standard Test Method for Thermal Resistance of Batting Systems Using a Hot Plate. *ASTM International*, doi:10.1520/D1518-14 (2014).

5 Moon, J. *et al.* Note: Thermal conductivity measurement of individual poly(ether ketone)/carbon nanotube fibers using a steady-state dc thermal bridge method. *Review of Scientific Instruments* **83**, 016103, doi:10.1063/1.3676650 (2012).

6 ASTM-D7896-14. Standard Test Method for Thermal Conductivity, Thermal Diffusivity and Volumetric Heat Capacity of Engine Coolants and Related Fluids by Transient Hot Wire Liquid Thermal Conductivity Method. *ASTM International*, doi:10.1520/D7896-14 (2014).

7 Cahill, D. G. Analysis of heat flow in layered structures for time-domain thermoreflectance. *Review of Scientific Instruments* **75**, 5119-5122 (2004).

8 Min, S., Blumm, J. & Lindemann, A. A new laser flash system for measurement of the thermophysical properties. *Thermochimica Acta* **455**, 46-49 (2007).

9 ASTM-D7984-16. Test Method for Measurement of Thermal Effusivity of Fabrics Using a Modified Transient Plane Source (MTPS) Instrument. *ASTM International*, doi:10.1520/D7984-16 (2016).

10 Cahill, D. G. Thermal-Conductivity Measurement from 30-K to 750-K - the 3-Omega Method. *Review of Scientific Instruments* **61**, 802-808, doi:Doi 10.1063/1.1141498 (1990).

11 Schmidt, A. J., Cheaito, R. & Chiesa, M. A frequency-domain thermoreflectance method for the characterization of thermal properties. *Review of Scientific Instruments* **80**, 094901 (2009).

12 Maldonado, O. Pulse method for simultaneous measurement of electric thermopower and heat conductivity at low temperatures. *Cryogenics* **32**, 908-912 (1992).

13 Dames, C. Measuring the thermal conductivity of thin films: 3 omega and related electrothermal methods. *Annual Review of Heat Transfer* **16** (2013).

14 Dames, C. & Chen, G. 1ω, 2ω, and 3ω methods for measurements of thermal properties. *Review of Scientific Instruments* **76**, 124902, doi:10.1063/1.2130718 (2005).

15 Borca-Tasciuc, T., Kumar, A. R. & Chen, G. Data reduction in 3ω method for thin-film thermal conductivity determination. *Review of Scientific Instruments* **72**, 2139-2147, doi:doi:http://dx.doi.org/10.1063/1.1353189 (2001).

16 Feser, J. P. *Scalable routes to efficient thermoelectric materials*, UC Berkeley, (2010).

17 Bergman, T. L., Lavine, A. S., Incropera, F. P. & DeWitt, D. P. Fundamentals of Heat and Mass Transfer, 7th ed., 983-986 (2011).

18 Schiffres, S. N. & Malen, J. A. Improved 3-omega measurement of thermal conductivity in liquid, gases, and powders using a metal-coated optical fiber. *Review of Scientific Instruments* **82**, 064903, doi:10.1063/1.3593372 (2011).

19 Kommandur, S., Mahdavifar, A., Jin, S., Hesketh, P. J. & Yee, S. Metal-coated glass microfiber for concentration detection in gas mixtures using the 3-Omega excitation method. *Sensors and Actuators A: Physical* **250**, 243-249 (2016).

20 Bougher, T. L. *et al.* Thermal boundary resistance in GaN films measured by time domain thermoreflectance with robust Monte Carlo uncertainty estimation. *Nanoscale and Microscale Thermophysical Engineering* **20**, 22-32 (2016).

21 Papadopoulos, C. E. & Yeung, H. Uncertainty estimation and Monte Carlo simulation method. *Flow Measurement and Instrumentation* **12**, 291-298 (2001).

22 Yang, J., Ziade, E. & Schmidt, A. J. Uncertainty analysis of thermoreflectance measurements. *Review of Scientific Instruments* **87**, 014901 (2016).

23 Azad, A., Akbar, S., Mhaisalkar, S., Birkefeld, L. & Goto, K. Solid-state gas sensors: A review. *Journal of the Electrochemical Society* **139**, 3690-3704 (1992).

24 Fraiwan, L., Lweesy, K., Bani-Salma, A. & Mani, N. in *Biomedical Engineering (MECBME), 2011 1st Middle East Conference on.* 11-14 (IEEE).

25 Jones, M. & Nevell, T. The detection of hydrogen using catalytic flammable gas sensors. *Sensors and Actuators* **16**, 215-224 (1989).

26 Khanna, V. *et al.* Design and electro-thermal simulation of a polysilicon microheater on a suspended membrane for use in gas sensing. *Indian Journal of pure and applied physics* **45**, 332 (2007).

27 Zanini, M. *et al.* Fabrication and properties of a Si-based high-sensitivity microcalorimetric gas sensor. *Sensors and Actuators A: Physical* **48**, 187-192 (1995).

28 Cruz, D. *et al.* Microfabricated thermal conductivity detector for the micro-ChemLab™. *Sensors and Actuators B: Chemical* **121**, 414-422 (2007).

29 Narayanan, S., Alfeeli, B. & Agah, M. Two-port static coated micro gas chromatography column with an embedded thermal conductivity detector. *Sensors Journal, IEEE* **12**, 1893-1900 (2012).

30 Puente, D., Gracia, F. J. & Ayerdi, I. Thermal conductivity microsensor for determining the Methane Number of natural gas. *Sensors and Actuators B: Chemical* **110**, 181-189 (2005).

31 Mahdavifar, A. *et al.* Simulation and fabrication of an ultra-low power miniature microbridge thermal conductivity gas sensor. *Journal of Electrochemical Society* **161**, 855-861 (2014).

32 Kawano, T. *et al.* An electrothermal carbon nanotube gas sensor. *Nano letters* **7**, 3686-3690 (2007).

33 Ahn, M. W. *et al.* On-chip fabrication of ZnO-nanowire gas sensor with high gas sensitivity. *Sensors and Actuators B: Chemical* **138**, 168-173 (2009).

34 Yu, C. *et al.* Integration of metal oxide nanobelts with microsystems for nerve agent detection. *Applied Physics Letters* **86**, 063101-063101-063103 (2005).

35 Kommandur, S., Mahdavifar, A., Hesketh, P. J. & Yee, S. A microbridge heater for low power gas sensing based on the 3-Omega technique. *Sensors and Actuators A: Physical* **233**, 231-238, doi:10.1016/j.sna.2015.07.011 (2015).

36 Linstrom, P. J., Mallard, W. G. & Eds. NIST Chemistry WebBook, NIST Standard Reference Database Number 69. *National Institute of Standards and Technology, Gaithersburg MD, 20899*.

37 Cahill, D. G. & Pohl, R. O. Heat flow and lattice vibrations in glasses. *Solid State Communications* **70**, 927-930 (1989).

38 Cahill, D. G., Watson, S. K. & Pohl, R. O. Lower limit to the thermal conductivity of disordered crystals. *Physical Review B* **46**, 6131-6140 (1992).

39 Toberer, E. S., Baranowski, L. L. & Dames, C. Advances in Thermal Conductivity. *Annual Review of Materials Research* **42**, 179-209, doi:doi:10.1146/annurev-matsci-070511-155040 (2012).

40 Choy, C. L. Thermal conductivity of polymers. *Polymer* **18**, 984-1004 (1977).

41 Choy, C. L. & Greig, D. The low temperature thermal conductivity of isotropic and oriented polymers. *Journal of Physics, C: Solid State Physics* **10**, 169-179 (1977).

42 Greig, D. Low temperature thermal conductivity of polymers. *Cryogenics* **28**, 243-247 (1988).

43 Shenogin, S., Bodapati, A., Keblinski, P. & McGaughey, A. J. H. Predicting the thermal conductivity of inorganic and polymeric glasses: The role of anharmonicity. *Journal of Applied Physics* **105**, 034906, doi:doi:http://dx.doi.org/10.1063/1.3073954 (2009).

44 Freeman, J. J. & Anderson, A. C. Thermal conductivity of amorphous solids. *Physical Review B* **34**, 5684-5690, doi:10.1103/PhysRevB.34.5684 (1986).

45 Marquardt, E. D., Le, J. P. & Radebaugh, R. in *11th International Cryocooler Conference* (National Institute of Standards and Technology, Keystone, CO, 2000).

46 Ashcroft, N. W. & Mermin, N. D. *Solid state physics*. (Holt, Rinehart and Winston, 1976).

47 Graebner, J. E., Golding, B. & Allen, L. C. Phonon localization in glasses. *Physical Review B* **34**, 5696-5701 (1986).

48 Alexander, S., Entin-Wohlman, O. & Orbach, R. Phonon-fracton anharmonic interactions: The thermal conductivity of amorphous materials. *Physical Review B* **34**, 2726-2734 (1986).

49 Grannan, E. R., Randeria, M. & Sethna, J. P. Low-temperature properties of a model glass. *Physical Review Letters* **60**, 1402-1405 (1988).

50 Allen, P. B., Feldman, J. L., Fabian, J. & Wooten, F. Diffusons, locons and propagons: Character of atomie yibrations in amorphous Si. *Philosophical Magazine Part B* **79**, 1715-1731 (1999).

51 Lake Shore Cryotronics Inc., Cryogenic Reference Tables, http://www.lakeshore.com/Documents/LSTC_appendixI_l.pdf (accessed December 1, 2016). <http://www.lakeshore.com/Documents/LSTC_appendixI_l.pdf> (

52 Barucci, M., Olivieri, E., Pasca, E., Risegari, L. & Ventura, G. Thermal conductivity of Torlon between 4.2 and 300K. *Cryogenics* **45**, 295-299, doi:10.1016/j.cryogenics.2004.11.006 (2005).

53 Woodcraft, A. L., Martelli, V. & Ventura, G. Thermal conductivity of Tecamax® SRP from millikelvin temperatures to room temperature. *Cryogenics* **50**, 66-70, doi:http://dx.doi.org/10.1016/j.cryogenics.2009.11.002 (2010).

54 Allen, P. B. & Feldman, J. L. Thermal conductivity of disordered harmonic solids. *Physical Review B* **48**, 12581-12588, doi:10.1103/PhysRevB.48.12581 (1993).

55 Feldman, J. L., Kluge, M. D., Allen, P. B. & Wooten, F. Thermal conductivity and localization in glasses: Numerical study of a model of amorphous silicon. *Physical Review B* **48**, 12589-12602, doi:10.1103/PhysRevB.48.12589 (1993).

56 Kamitakahara, W. A., Soukoulis, C. M., Shanks, H. R., Buchenau, U. & Grest, G. S. Vibrational spectrum of amorphous silicon: Experiment and computer simulation. *Physical Review B* **36**, 6539-6542 (1987).

57 Wooten, F., Winer, K. & Weaire, D. Computer generation of structural models of amorphous Si and Ge. *Phys Rev Lett* **54**, 1392-1395, doi:10.1103/PhysRevLett.54.1392 (1985).

58 Larkin, J. M. & McGaughey, A. J. H. Thermal conductivity accumulation in amorphous silica and amorphous silicon. *Physical Review B* **89**, doi:10.1103/PhysRevB.89.144303 (2014).

59 Luo, T., Esfarjani, K., Shiomi, J., Henry, A. & Chen, G. Molecular dynamics simulation of thermal energy transport in polydimethylsiloxane. *Journal of Applied Physics* **109**, 074321, doi:doi:http://dx.doi.org/10.1063/1.3569862 (2011).

60 Ma, H. & Tian, Z. Effects of polymer chain confinement on thermal conductivity of ultrathin amorphous polystyrene films. *Applied Physics Letters* **107**, 073111, doi:doi:http://dx.doi.org/10.1063/1.4929426 (2015).

61 Kittel, C. *Introduction to solid state physics*. (Wiley, 2005).

62 Zhang, Z. M. *Nano/microscale heat transfer*. (McGraw-Hill New York, 2007).

63 Biswas, R., Bouchard, A. M., Kamitakahara, W. A., Grest, G. S. & Soukoulis, C. M. Vibrational Localization in Amorphous Silicon. *Physical Review Letters* **60**, 2280-2283 (1988).

64 Seyf, H. R. & Henry, A. A method for distinguishing between propagons, diffusions, and locons. *Journal of Applied Physics* **120**, 025101, doi:10.1063/1.4955420 (2016).

65 McGaughey, A. J. H. & Kaviany, M. Quantitative validation of the Boltzmann transport equation phonon thermal conductivity model under the single-mode relaxation time approximation. *Physical Review B* **69**, doi:10.1103/PhysRevB.69.094303 (2004).

66 Beltukov, Y. M., Kozub, V. I. & Parshin, D. A. Ioffe-Regel criterion and diffusion of vibrations in random lattices. *Physical Review B* **87**, 134203 (2013).

67 Sheng, P. & Zhou, M. Heat Conductivity of amorphous Solids: simulation results on model structures. *Science* **253**, 539 (1991).

68 Masciovecchio, C. *et al.* Evidence for a crossover in the frequency dependence of the acoustic attenuation in vitreous silica. *Phys Rev Lett* **97**, 035501, doi:10.1103/PhysRevLett.97.035501 (2006).

69 Christie, J. K., Taraskin, S. N. & Elliott, S. R. Vibrational behavior of a realistic amorphous-silicon model. *Journal of Non-Crystalline Solids* **353**, 2272-2279, doi:10.1016/j.jnoncrysol.2007.02.039 (2007).

70 Lv, W. & Henry, A. Phonon transport in amorphous carbon using Green–Kubo modal analysis. *Applied Physics Letters* **108**, 181905, doi:doi:http://dx.doi.org/10.1063/1.4948605 (2016).

71 Wei, L. & Asegun, H. Direct calculation of modal contributions to thermal conductivity via Green–Kubo modal analysis. *New Journal of Physics* **18**, 013028 (2016).

72 Feldman, J. L., Allen, P. B. & Bickham, S. R. Numerical study of low-frequency vibrations in amorphous silicon. *Physical Review B* **59**, 3551-3559 (1999).

73 Solvay Ultra Polymers, Torlon PAI Design Guide, http://www.solvayultrapolymers.com/en/binaries/Torlon-PAI-Design-Guide_EN-227547.pdf (accessed December 1, 2016). *Torlon PAI Design Guide*, <http://www.solvayultrapolymers.com/en/binaries/Torlon-PAI-Design-Guide_EN-227547.pdf> (

74 Solvay Ultra Polymers, Torlon PAI Overview, http://www.solvay.com/en/binaries/Torlon-PAI-Overview_EN-220724.pdf (accessed December 1, 2016). *Torlon PAI Overview*, <http://www.solvay.com/en/binaries/Torlon-PAI-Overview_EN-220724.pdf> (

75 SD Plastics, Tecamax SRP Properties, http://www.sdplastics.com/ensinger/Tecamax_SRP.pdf (accessed December 1, 2016). *Tecamax SRP Properties*, <http://www.sdplastics.com/ensinger/Tecamax_SRP.pdf> (

76 Kommandur, S. & Yee, S. K. An empirical model to predict temperature-dependent thermal conductivity of amorphous polymers. *Journal of Polymer Science Part B: Polymer Physics* **55**, 1160-1170 (2017).

77 Henry, A. & Chen, G. High Thermal Conductivity of Single Polyethylene Chains Using Molecular Dynamics Simulations. *Physical Review Letters* **101**, 235502 (2008).

78 Lv, W. & Henry, A. Theoretical Prediction of Room Temperature Thermal Superconductivity in Single Polythiophene Chains. *Bulletin of the American Physical Society* **60** (2015).

79 Shen, S., Henry, A., Tong, J., Zheng, R. & Chen, G. Polyethylene nanofibres with very high thermal conductivities. *Nat Nano* **5**, 251-255, doi:http://www.nature.com/nnano/journal/v5/n4/suppinfo/nnano.2010.27_S1.html (2010).

80 Singh, V. *et al.* High thermal conductivity of chain-oriented amorphous polythiophene. *Nat Nano* **9**, 384-390, doi:10.1038/nnano.2014.44 (2014).

81 Wang, X., Ho, V., Segalman, R. A. & Cahill, D. G. Thermal Conductivity of High-Modulus Polymer Fibers. *Macromolecules* **46**, 4937-4943, doi:10.1021/ma400612y (2013).

82 Bubnova, O. & Crispin, X. Towards polymer-based organic thermoelectric generators. *Energy & Environmental Science* **5**, 9345-9362, doi:10.1039/C2EE22777K (2012).

83 He, M., Qiu, F. & Lin, Z. Towards high-performance polymer-based thermoelectric materials. *Energy & Environmental Science* **6**, 1352-1361, doi:10.1039/C3EE24193A (2013).

84 Huang, D. *et al.* Conjugated-Backbone Effect of Organic Small Molecules for n-Type Thermoelectric Materials with ZT over 0.2. *Journal of the American Chemical Society* **139**, 13013-13023, doi:10.1021/jacs.7b05344 (2017).

85 Liu, J. *et al.* Thermal Conductivity and Elastic Constants of PEDOT:PSS with High Electrical Conductivity. *Macromolecules* **48**, 585-591, doi:10.1021/ma502099t (2015).

86 Sun, Y. *et al.* Flexible n-Type High-Performance Thermoelectric Thin Films of Poly(nickel-ethylenetetrathiolate) Prepared by an Electrochemical Method. *Advanced Materials* **28**, 3351-3358, doi:10.1002/adma.201505922 (2016).

87 Feser, J. P. & Cahill, D. G. Probing anisotropic heat transport using time-domain thermoreflectance with offset laser spots. *Review of Scientific Instruments* **83**, 104901, doi:10.1063/1.4757863 (2012).

88 Feser, J. P., Liu, J. & Cahill, D. G. Pump-probe measurements of the thermal conductivity tensor for materials lacking in-plane symmetry. *Review of Scientific Instruments* **85**, 104903, doi:10.1063/1.4897622 (2014).

89 Rodin, D. & Yee, S. K. Simultaneous measurement of in-plane and through-plane thermal conductivity using beam-offset frequency domain thermoreflectance. *Review of Scientific Instruments* **88**, 014902 (2017).

90 Ju, Y., Kurabayashi, K. & Goodson, K. Thermal characterization of anisotropic thin dielectric films using harmonic Joule heating. *Thin Solid Films* **339**, 160-164 (1999).

91 Jang, W., Chen, Z., Bao, W., Lau, C. N. & Dames, C. Thickness-Dependent Thermal Conductivity of Encased Graphene and Ultrathin Graphite. *Nano Letters* **10**, 3909-3913, doi:10.1021/nl101613u (2010).

92 Asheghi, M., Touzelbaev, M. N., Goodson, K. E., Leung, Y. K. & Wong, S. S. Temperature-Dependent Thermal Conductivity of Single-Crystal Silicon Layers in SOI Substrates. *Journal of Heat Transfer* **120**, 30-36, doi:10.1115/1.2830059 (1998).

93 Zhang, X. & Grigoropoulos, C. P. Thermal conductivity and diffusivity of free-standing silicon nitride thin films. *Review of Scientific Instruments* **66**, 1115-1120, doi:10.1063/1.1145989 (1995).

94 Zhang, X. *et al.* Thermal and electrical conductivity of a suspended platinum nanofilm. *Applied Physics Letters* **86**, 171912, doi:10.1063/1.1921350 (2005).

95 Tai, Y. C., Mastrangelo, C. H. & Muller, R. S. Thermal conductivity of heavily doped low-pressure chemical vapor deposited polycrystalline silicon films. *Journal of Applied Physics* **63**, 1442-1447, doi:10.1063/1.339924 (1988).

96 Kommandur, S. & Yee, S. A suspended 3-omega technique to measure the anisotropic thermal conductivity of semiconducting polymers. *Review of Scientific Instruments* **89**, 114905 (2018).

97 Gray, A. S. & Uher, C. Thermal conductivity of mica at low temperatures. *Journal of Materials Science* **12**, 959-965, doi:10.1007/BF00540978 (1977).

98 Abderrahim, B., Laurent, I., Evelyne, G. & Yves, C. A simultaneous characterization of thermal conductivity and diffusivity of polymer materials by a periodic method. *Journal of Physics D: Applied Physics* **37**, 132 (2004).

99 Krishnakumar Menon, A. *Development of Organic Thermoelectric Materials and Devices for Energy Harvesting*, Georgia Institute of Technology, (2018).

100 Wolfe, R. M. *et al.* Simultaneous Enhancement in Electrical Conductivity and Thermopower of n-Type NiETT/PVDF Composite Films by Annealing. *Advanced Functional Materials* **28**, 1803275 (2018).

101 Menon, A. K., Wolfe, R. M. W., Kommandur, S. & Yee, S. K. Progress in Nickel-Coordinated Polymers as Intrinsically Conducting n-Type Thermoelectric Materials. *Advanced Electronic Materials* **0**, 1800884, doi:10.1002/aelm.201800884 (2019).

102 Cahill, D. G. *et al.* Nanoscale thermal transport. *Journal of Applied Physics* **93**, 793-818 (2003).

103 Cahill, D. G. *et al.* Nanoscale thermal transport. II. 2003–2012. *Applied Physics Reviews* **1**, 011305 (2014).

104 Chen, G. *Nanoscale energy transport and conversion: a parallel treatment of electrons, molecules, phonons, and photons*. (Oxford University Press, 2005).

105 Li, D. *et al.* Thermal conductivity of individual silicon nanowires. *Applied Physics Letters* **83**, 2934-2936, doi:10.1063/1.1616981 (2003).

106 Kim, P., Shi, L., Majumdar, A. & McEuen, P. L. Thermal Transport Measurements of Individual Multiwalled Nanotubes. *Physical Review Letters* **87**, 215502, doi:10.1103/PhysRevLett.87.215502 (2001).

107 Lee, S. *et al.* Anomalously low electronic thermal conductivity in metallic vanadium dioxide. *Science* **355**, 371-374, doi:10.1126/science.aag0410 (2017).

108 Swinkels, M. Y. *et al.* Diameter dependence of the thermal conductivity of InAs nanowires. *Nanotechnology* **26**, 385401 (2015).

109 Kim, J., Ou, E., Sellan, D. P. & Shi, L. A four-probe thermal transport measurement method for nanostructures. *Review of Scientific Instruments* **86**, 044901 (2015).

110 Ek, M. & Filler, M. A. Atomic-Scale Choreography of Vapor–Liquid–Solid Nanowire Growth. *Accounts of Chemical Research* **51**, 118-126, doi:10.1021/acs.accounts.7b00392 (2018).

111 Malhotra, A. & Maldovan, M. Impact of Phonon Surface Scattering on Thermal Energy Distribution of Si and SiGe Nanowires. *Scientific Reports* **6**, 25818, doi:10.1038/srep25818 (2016).

112 Beckmann, P. & Spizzichino, A. The scattering of electromagnetic waves from rough surfaces. *Norwood, MA, Artech House, Inc., 1987, 511 p.* (1987).

113 George, M. C., Rodriguez, M. A., Kent, M. S., Brennecka, G. L. & Hopkins, P. E. Thermal Conductivity of Self-Assembling Symmetric Block Copolymer Thin Films of Polystyrene-Block-Poly(methyl methacrylate). *Journal of Heat Transfer* **138**, 024505-024505-024505, doi:10.1115/1.4031701 (2015).

114 Wei, X. & Luo, T. The effect of the block ratio on the thermal conductivity of amorphous polyethylene–polypropylene (PE–PP) diblock copolymers. *Physical Chemistry Chemical Physics* **20**, 20534-20539, doi:10.1039/C8CP03433H (2018).

115 Rashidi, V., Coyle, E. J., Sebeck, K., Kieffer, J. & Pipe, K. P. Thermal Conductance in Cross-linked Polymers: Effects of Non-Bonding Interactions. *The*

Journal of Physical Chemistry B **121**, 4600-4609, doi:10.1021/acs.jpcb.7b01377 (2017).

116 Huang, C., Qian, X. & Yang, R. Thermal conductivity of polymers and polymer nanocomposites. *Materials Science and Engineering: R: Reports* **132**, 1-22, doi:https://doi.org/10.1016/j.mser.2018.06.002 (2018).

117 Mehos, M. *et al.* Concentrating Solar Power Gen3 Demonstration Roadmap. (NREL (National Renewable Energy Laboratory (NREL), Golden, CO (United States), 2017).

118 Dou, L. *et al.* Single-crystal linear polymers through visible light–triggered topochemical quantitative polymerization. *Science* **343**, 272-277 (2014).